



**OFFSHORE TECHNOLOGY  
RESEARCH CENTER**

**Surfical Geological Characteristics of the Alaminos  
Canyon, Gulf of Mexico**

**By**

**Jia-Yuh Lui**

266 AA

214-A

# **Surfical Geological Characteristics of the Alaminos Canyon, Gulf of Mexico**

**By**

**Jia-Yuh Lui**

NSF# CDR-8721512



**OFFSHORE  
TECHNOLOGY  
RESEARCH  
CENTER**

*A National Science Foundation Engineering Research Center*

12/98A9875

*For more information contact:*

**Offshore Technology Research Center**

Texas A&M University  
1200 Mariner Drive  
College Station, TX 77845-3400  
(409) 845-6000

*or,*

**Center for Offshore Technology**  
The University of Texas at Austin  
Department of Civil Engineering  
ECJ 4.200

Austin, Texas 78712  
(512) 471-3753

## ABSTRACT

Surficial Geological Characteristics of the Alaminos Canyon,

Gulf of Mexico. (December 1997)

Jia-Yuh Liu, B.S., National Taiwan College of Marine Science and Technology;

M.S., Texas A&M University

Chair of Advisory Committee: Dr. William R. Bryant

Understanding the surface morphology and sediment in the deep water environment is important for construction of platforms and pipelines, estimating for potential geological hazards, and development of physical oceanography and sediment transport models. As bathymetry is mainly a surficial reflection of subsurface allochthonous salt in the Gulf of Mexico, a detailed bathymetry can help us understand the deep structure. This study uses multibeam system bathymetry data, rejects erroneous data points, and examines different interpolation methods. The error points are removed from the georeferenced data based on an algorithm usually used during the survey (Herlihy et al., 1992). To generate optimum resolution of the bathymetry data, different spatial interpolation methods are examined. Universal kriging with a linear model (Ukl) seems to be the best choice for the Sea Beam data in this study.

The GLORIA II sidescan sonar image released by National Geophysical Data Center (NGDC) is prone to the uncertainty of pixel locations and ambiguity of artifacts versus true backscattering. This study corrects these errors and examines location inaccuracy. The reprocessed GLORIA II image has a location accuracy of about 400 m. In a 50 m gridded bathymetry and sonar image, the spatial uncertainty is about 8 pixels. The possibility of reducing the noisy near nadir pixels is discussed. In a single sonograph strip, the processed image shows significant improvement. When these sonographs are



georeferenced on a plane earth, spatial interpolation is used to readjust the aspect-ratio. The resultant image seems fuzzier than the original image but contains fewer artifacts.

Ground truth samples are used to examine sediment accumulation rates. A change of the accumulation ratio through time for two cores suggests episodic sediment inputs. The ground truth data are also used to model the acoustic energy attenuation rate. The result show that the energy is more than 3 dB down or has lost more than 50% of its incident energy at a depth of 500 cm below the seafloor.

Four different Geographic Information System (GIS) packages are used to take advantage of their build-in functionality and compliment their deficiencies. Bathymetry data, properties derived from bathymetry data, sidescan sonar imagery, ground truth data, and other support geophysical data are integrated to give a geological interpretation of the canyon. The ability of automated and interactive mapping through the Internet is briefly discussed at the end of Chapter IV.

## ACKNOWLEDGMENTS

I am most grateful to my committee chair, Dr., William R. Bryant, for both academic guidance and financial support. I am also indebted to my committee members; Dr. William W. Sager, Aubrey L. Anderson, Wayne Dunlap and Daniel Sui. Dr. William Sager supplied the multi-beamed data and unlimited access to his 35" HP DesignJet Printer. Professor Aubrey Anderson gave me valuable advice and encouragement. Associate Director of OTRC, Wayne Dunlap, offered financial support. Dr. Daniel Sui taught the excellent advanced GIS class. I thank my GCR, Dr. Lloyd T. Wilson, for his comments and suggestions.

I would also like to thank the students and crews who helped collect the Deep Tow Data. Matt Howard led me into the Information Highway before the name was used, and his allowing me on the PV- WAVE is greatly appreciated.

This research is funded by OTRC Seafloor Foundation Engineering Project, a NSF Engineering Research Center (CDR- 8721512).



## TABLE OF CONTENTS

	Page
ABSTRACT.....	iii
ACKNOWLEDGMENTS.....	v
TABLE OF CONTENTS.....	vii
LIST OF TABLES .....	ix
LIST OF FIGURES .....	x
 CHAPTER	
I      INTRODUCTION.....	1
Study area.....	1
Data base.....	3
Objectives and importance of this research .....	6
II      BACKGROUND .....	9
Sea Beam.....	9
GLORIA II.....	11
Geologic settings and previous studies .....	16
III     DATA PROCESSING AND EVALUATION .....	19
Post-processing Sea Beam data.....	19
Post-processing GLORIA II data .....	25
Ground truth measurements .....	30
IV     RESULTS AND DISCUSSIONS .....	33
Sea Beam filtered results.....	33
Gridding algorithms .....	37
GLORIA II sidescan sonar image .....	61
Ground truth samples.....	69
Sediment accumulation rate .....	74
Intrinsic morphologic properties.....	77
Implication of reprocessed GLORIA II image.....	94
Other support data .....	104
Geological interpretation.....	111
Visualization and data sharing .....	116
V      SUMMARY AND CONCLUSIONS.....	124

	Page
REFERENCES CITED .....	128
APPENDIX A.....	133
APPENDIX B.....	134
APPENDIX C.....	138
VITA .....	142

## LIST OF TABLES

TABLE	Page
1 Comparison chart between Sea Beam and GLORIA II .....	15
2 Statistics of interpolated difference with respect to Ukl method .....	53
3 Signal-to-noise ratio (SNR) of processed GLORIA II image .....	68
4 Averaged dry-bulk density of AC01 and AC02 for Zone A, B, and C .....	76
5 Grazing angle and footprint size (F.S.) in the ground truth locations .....	97
6 Rayleigh roughness and DN values in the ground truth locations .....	98

## LIST OF FIGURES

FIGURE	Page
1 Bathymetric relief map of northern Gulf of Mexico .....	2
2 Location map of the study area-Alaminos Canyon .....	3
3 Multibeam and sidescan sonar systems survey routes and location of ground truth samples .....	5
4 A multibeam echo sounding system-Sea Beam .....	10
5 Determining the time for the center of mass for each beam .....	12
6 GLORIA II sidescan sonar .....	13
7 GLORIA II image in the Alaminos Canyon .....	26
8 DN values of a GLORIA II image strip .....	27
9 Unedited Alaminos Canyon bathymetric contour map .....	34
10 Histograms of Sea Beam depth soundings .....	35
11 Edited Alaminos Canyon bathymetric contour map .....	36
12 Alaminos Canyon bathymetric contour map.....	38
13 Locations of randomly selected 233 validating points.....	40
14 Depth sounding residual contour map-IDW (inverse distance weighted) method.....	41
15 Depth sounding residual contour map-MinCurv (minimum surface curvature) method .....	42
16 Depth sounding residual contour map-TIN (triangulated irregular network) method.....	43
17 Depth sounding residual contour map-OK (ordinary kriging) method.....	44
18 Depth sounding residual contour map-UKl (universal kriging method with a linear model) .....	45
19 Depth sounding residual contour map-UKq (universal kriging method with a quadratic model).....	46
20 Depth sounding residual contour map-SubUK (subdivisioned UK method with a linear model) .....	47

FIGURE	Page
21 Summary statistics of depth sounding residuals based on IDW (inverse distance weighting), MinCurv (minimum surface curvature), and TIN (triangulated irregular network) methods.....	48
22 Summary statistics of depth sounding residuals based on kriging methods .....	49
23 Depth difference between IDW and UKI methods.....	54
24 Depth difference between MinCurv and UKI methods.....	55
25 Depth difference between TIN and UKI methods.....	56
26 Depth difference between OK and UKI methods .....	57
27 Depth difference between UKq and UKI methods.....	58
28 Depth difference between SubUK and UKI methods.....	59
29 Example of a GLORIA II image strip .....	62
30 Averaged along ship track DN profiles of a GLORIA II image.....	63
31 The same GLORIA II image strip as Figure 29 .....	65
32 Reprocessed GLORIA II image of the Alaminos Canyon .....	67
33 P-wave velocity and bulk-density plots of AC01 .....	70
34 P-wave velocity and bulk-density plots of AC02 .....	71
35 P-wave velocity and bulk-density plots of AC03 .....	72
36 P-wave velocity and bulk-density plots of AC05 .....	73
37 Correlation of bulk density between AC01 and AC02 .....	75
38 Bathymetric relief map of the Alaminos Canyon .....	78
39 Slope gradient map of the Alaminos Canyon.....	80
40 Seafloor roughness map of the Alaminos Canyon .....	81
41 The assigning of pixel values for a slope direction map.....	82
42 Slope direction map of the Alaminos Canyon .....	83
43 Drainage pattern of the Alaminos Canyon .....	84
44 Location map of bathymetric profiles of the channels.....	86



FIGURE	Page
45 Location map of bathymetric profiles of the main drainage path .....	87
46 Profiles of the channels along the canyon wall .....	88
47 Profiles of the main drainage path of the canyon .....	90
48 Transmitted GLORIA II acoustic energy versus depth in the ground truth locations .....	102
49 Composite contour map of the Alaminos Canyon area with locations of support data .....	105
50 TAMU Deep Tow Line 11 .....	107
51 TAMU Deep Tow Line 4.....	109
52 Seismic profile in the southeast of the Alaminos Canyon.....	112
53 Line drawing of geological interpretation of the Alaminos Canyon.....	113
54 Composite relief map of the Alaminos Canyon area .....	117
55 Color-coded slope gradient, drainage network, ground truth locations draped over bathymetry.....	118
56 Same as Figure 55 but with three times of vertical exaggeration and a different viewing direction .....	119
57 Color-coded GLORIA II image draped over Sea Beam bathymetry .....	120
58 Interactive bathymetric contour mapping through the Internet.....	122
59 VRML enabled “fly-by” in the Alaminos Canyon.....	123

## CHAPTER I

### INTRODUCTION

The continental slope of Texas and Louisiana has a regional slope gradient of less than  $1^\circ$ , but locally the seafloor is very rugged and the slope gradient can exceed  $30^\circ$ . The rugged seafloor is composed of more than one hundred basins and domes which are products of underlying vertical and horizontal displacements of allochthonous salt—salt that had been separated from its “mother” layer, the Jurassic Louann salt (Figure 1).

With increased interest in deep water hydrocarbon discoveries in subsalt structures on the continental slope of Texas and Louisiana, understanding the deep water environment becomes essential. The Offshore Technology Research Center (OTRC) seafloor foundation engineering project was formed to characterize the seafloor engineering properties, evaluate gas hydrate hazards and slope stability, and develop innovative foundation systems for deep water environment. This research is part of the OTRC seafloor project with primary focus on processing, integrating, visualizing, and interpreting seafloor surficial geophysical and geological data.

#### **Study area**

This study covers a major portion of the Alaminos Canyon (Figure 2). Longitude of the study area extends from approximately  $94.69^\circ\text{W}$  to  $94.33^\circ\text{W}$  and latitude extends from approximately  $26.3^\circ\text{N}$  to  $26.58^\circ\text{N}$ . Depths vary from about 1,600 m to 2,700 m.

---

This dissertation follows the style and format of the Bulletin of the American Association of Petroleum Geologists.

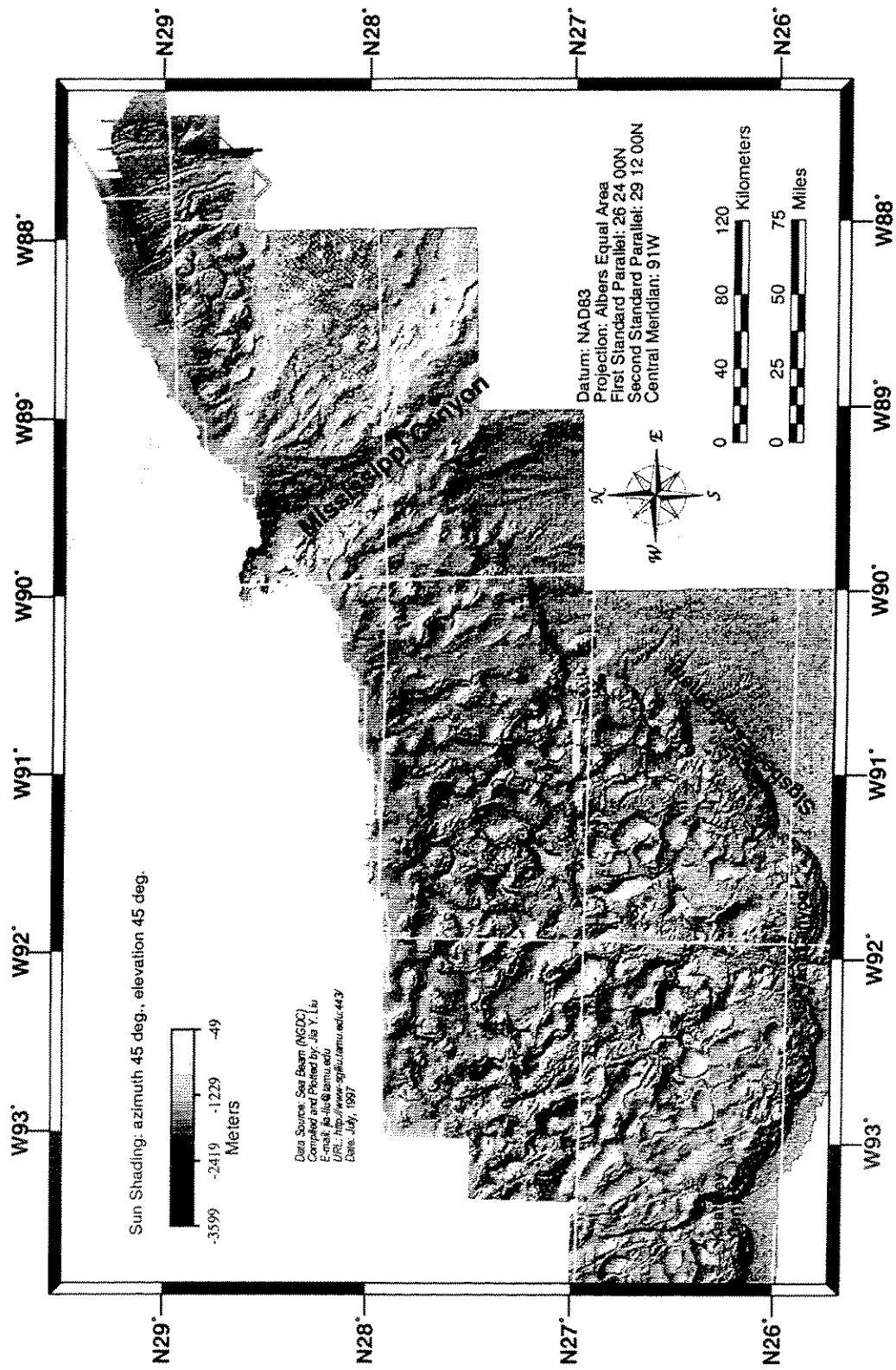


Figure 1-Bathymetric relief map of northern Gulf of Mexico.

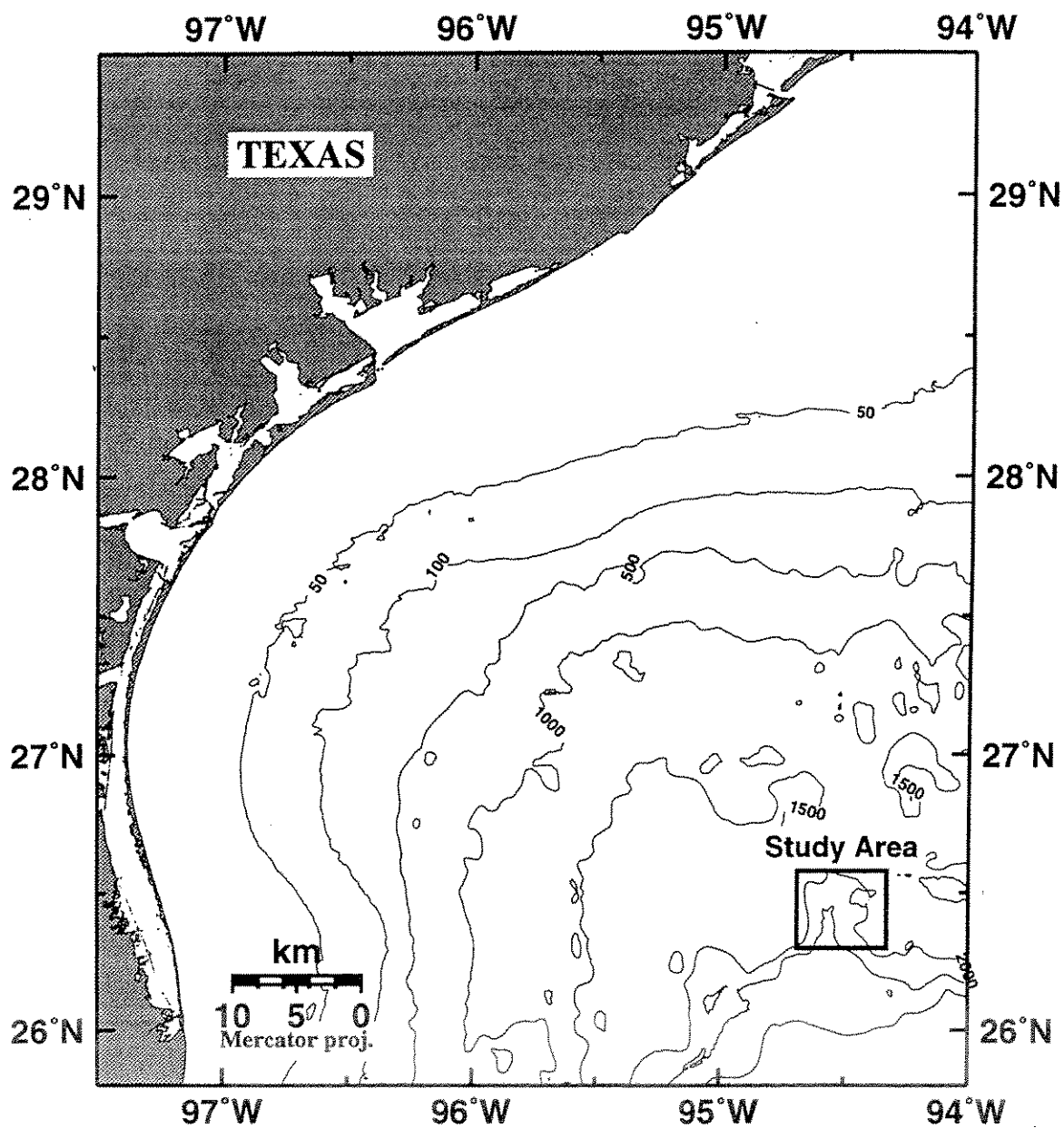


Figure 2-Location map of the study area-Alaminos Canyon. Contour interval in meters (After Bryant et al., 1990).

Alaminos Canyon has been described as the largest canyon in the lower continental slope of the northwestern Gulf of Mexico with a broad, square-shaped feature and dimensions of about 30 by 30 km. The canyon separates a dome-and-basin shaped Texas-Louisiana continental slope on the east from a relatively flat area on the west (Bryant et al., 1990). Based on scattered seismic lines, the canyon has been described as being formed by complex faulting, folding, salt deformation, submarine erosion (Bouma et al., 1972), and by coalescing of salt canopies (Hardin, 1989). Alaminos Canyon is also the location of the deepest riser drilling depth and the deepest known chemosynthetic organism community to the present in the Gulf of Mexico (Brown, 1996; Sager, 1997).

#### **Data base**

Data used for this study includes bathymetry, sidescan sonar backscattered images, ground truth samples, and other geophysical data (Appendix A). The bathymetry data used is from a 1990 Sea Beam multibeam echo sounder survey collected by R/V Atlantis II from WHOI (Woods Hole Oceanographic Institution; Sager, 1997). Sidescan sonar data is GLORIA II (Geological Long Range Inclined Asdic) imagery collected by U.S. Geological Survey (USGS) in 1985. Ground truth piston cores and TAMU Deep Tow echo sounder profiles were collected during 1996 Gyre cruises. Other support data, such as the salt distribution map and seismic lines, are also used in this study to tie the processed and interpreted geological features with previous observations. Figure 3 shows the survey routes for the multibeam and sidescan sonar systems. One ground truth sample, AC05, is located in the north, outside the study area.

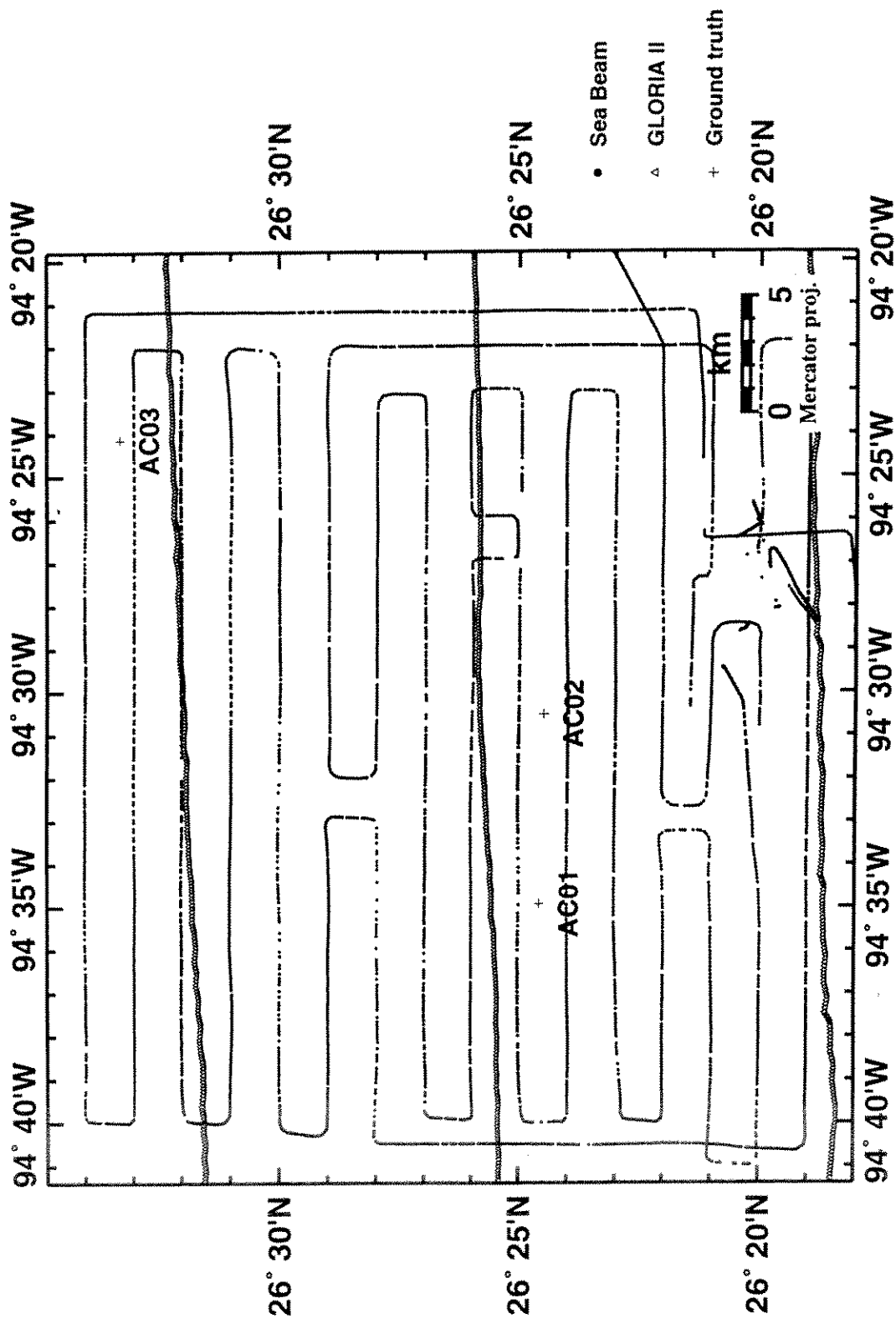


Figure 3-Multibeam and sidescan sonar systems survey routes and location of ground truth samples.

## **Objectives and importance of this research**

The objectives of this study are: (1) to process both previously released and recently collected bathymetric, sidescan sonar, and ground truth data in the Alaminos Canyon area, Gulf of Mexico; (2) to qualitatively and quantitatively compare the effects of different spatial interpolations on discrete depth soundings; (3) to evaluate the geological factors that contribute to the sidescan sonar image; (4) to characterize and interpret the surface and near surface geomorphological features.

Seafloor morphology or bathymetry is the basic and most important property of deep water environments. For examples, detailed bathymetry is a necessity in laying out a telephone cable route, estimating potential geological hazards, and building sediment transport models. Bathymetry is especially important for the continental slope of the Gulf of Mexico where the seafloor is mainly a surficial representation of subsurface allochthonous salt. As hydrocarbon traps are often closely related to allochthonous salt structures, an accurate and detailed bathymetry will help refine the extent of the underlying salt sheets in the hydrocarbon evaluation stage and the construction of platforms and pipelines in the prospecting stage.

The most extensive seafloor survey in the Gulf of Mexico was conducted by the National Oceanic and Atmospheric Administration (NOAA) from 1988 to 1991. This survey was made using a multibeam echosounder, Sea Beam, in the U.S. Exclusive Economic Zone (EEZ), which extends 200 nautical miles offshore from the United States and U.S. trust territories. Both gridded and raw data were released in 1992. However, the NOAA bathymetry mapping project was terminated after only part of the EEZ was surveyed. One of the unfinished areas is the Alaminos Canyon, in which the most detailed previous bathymetric map was based on seismic surveys with grid spacing of 8 to 14 km (Bryant et al., 1990). In 1990, William Sager and others surveyed a major

portion of the canyon using the same multibeam survey system (Sager, 1997). The Sea Beam soundings, with a spatial resolution of about 74 m to 120 m in the Alaminos Canyon, have never been published. The study uses the 1990 WHOI Sea Beam survey data and reveals the fine features of the bathymetry.

Spatial interpolation derives values at unsampled locations from sampled locations. This process is especially important when data points are randomly sampled and a high spatial resolution raster is necessary for many data analyses and visual presentations. Different interpolation algorithms can generate different results and affect the accuracy of results. However, a complex and computation-extensive algorithm does not necessarily outperform a simple algorithm. The choice of algorithm is data dependent, and should be made empirically. In this study, to fully use the depth soundings collected by multibeam systems, different interpolation algorithms are tested and compared. These comparisons not only offer criteria for choosing the best estimator but also present the accuracy of the interpolated result.

The long range GLORIA II sidescan sonar imagery of the Gulf of Mexico was released by National Geophysical Data Center (NGDC) in 1987. In the approximately 12° longitude by 6° latitude gray-scaled mosaic backscattered image, detrital sediments transported from the Mississippi Canyon and basins surrounded by high slope gradients are evident. But for a scale of tens of minutes by tens of minutes, several factors make geological interpretation difficult. These factors include the noisy nadir below the ship track, ambiguity of true or artifact pixel values, and the uncertainty of georeferencing. This study reprocesses the NGDC released GLORIA II data to differentiate artifacts from true backscattering, to register geographic coordinates for each footprint, and to examine parameters affecting backscattering.

The ground truth samples are used to describe physical properties of the deep water sediment and compare their spatial variations. When the bathymetry data, sidescan



sonar imagery, and physical properties of the sediment are combined, we can better understand the geomorphological driving processes and sediment movements in the Alaminos Canyon.

## CHAPTER II

### BACKGROUND

#### Sea Beam

Sea Beam is a hull-mounted multibeam echo sounder system (Figure 4). It was introduced by General Instrument Corporation in 1976. There are 20 transmitting transducers (3.05 m long by 1.83 m wide) which lie along the ship's keel and send out a 7-ms pulse of 12.158 kHz. There are 40 receiving transducers (3.05 m long by 0.46 m wide) which lie athwartships, and long axes are oriented fore-aft. By appropriate phase shift and summing, the transmitter forms a single  $2\frac{2}{3}^\circ$  by  $54^\circ$  beam, while the receiving beams are sixteen  $20^\circ$  by  $2\frac{2}{3}^\circ$  in a fan shaped pattern (Tyce, 1986). The predominant return acoustic energy is received from the intersection of the transmit and receive beams, forming the equivalent 16 discrete beams with  $2\frac{2}{3}^\circ \times 2\frac{2}{3}^\circ$  angular resolution for each beam. The swath angle is  $40^\circ$  from center-to-center of the two outermost beams or  $42.7^\circ$  between the outside edges of beams. The swath width is 73% of water depth, if calculated from the center of the outermost beams.

There are two main components in the Sea Beam instrument. One is a narrow beam echo sounder (NBES), and another is an echo processor (EP). The NBES includes signal generator, pitch and roll compensator, timing unit, power amplifiers, preamplifiers, and an analog beam-forming network. The pitch and roll compensator includes a gyroscope and a vertical reference sensor, which can detect an error of  $1/10^\circ$  (Tyce et al., 1987). The EP is used to digitize echo signals, correct roll and refraction, compute depths and horizontal distance, and generate output to a swath plotter with a near-real-time display.

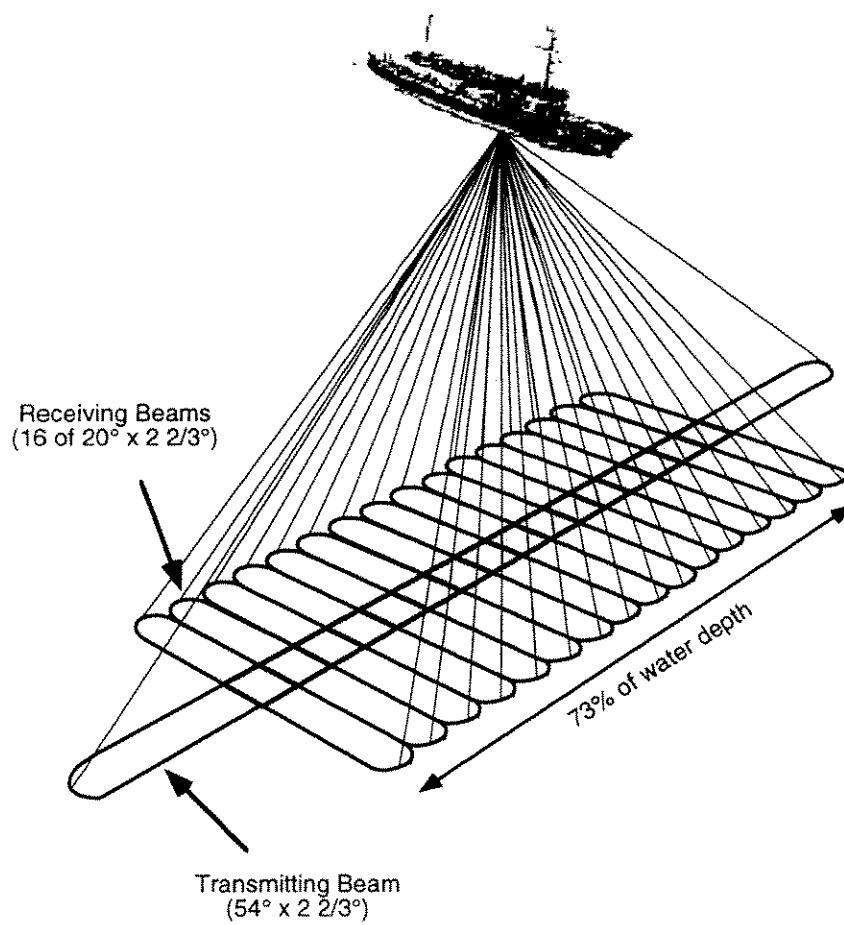


Figure 4-A multibeam echo sounding system-Sea Beam.

Figure 5 shows how the best estimate of arrival time or center of mass is measured for each return beam (Farr, 1980). Three stages are involved in the estimate of arrival time. They are gating, thresholding, and averaging. Gating is used to separate each beam from its previous ping. Thresholding is used to suppress noise and sidelobes. When the signals fall within the time gate and above the threshold, an averaging algorithm is applied to determine the arrival time. The next step is to correct for the rolling of the ship. From the velocity profile, depths and horizontal distances are calculated. The depth of the sounding  $Z$  and horizontal distance  $Y$  are calculated from (de Moustier and Kleinrock, 1986):

$$Z = R \cos \psi \quad (1)$$

$$Y = \frac{C_a}{C_n} R \sin \psi \quad (2)$$

where  $R$  is the slant range calculated by multiplying 750 m/s with the two-way travel time to the center of mass of the acoustic return,  $\psi$  is the stabilized beam angle,  $C_a$  is the mean sound velocity calculated from the measured sound velocity profile,  $C_n$  is the reference sound velocity for sea water (1,500 m/s).

The final soundings collected on the ship are called raw soundings or full resolution soundings. These raw soundings are also the point data that are processed and presented in this study.

## GLORIA II

GLORIA (Geological Long Range Inclined Asdic) is a long-range side-looking sonar (Figure 6) built by Institute of Oceanographic Sciences (IOS) in England in 1969. It

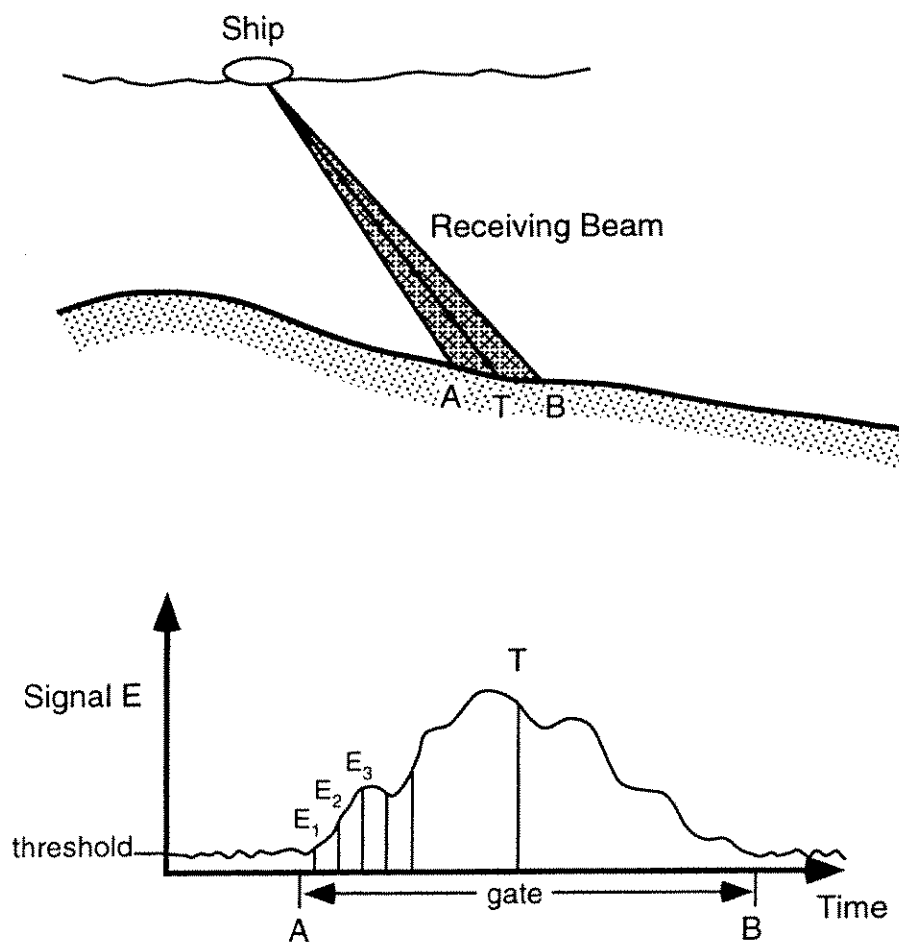


Figure 5-Determining the time for the center of mass for each beam (modified from Farr, 1980). The arrival time, T, is derived after signal strength is integrated between time A and B.

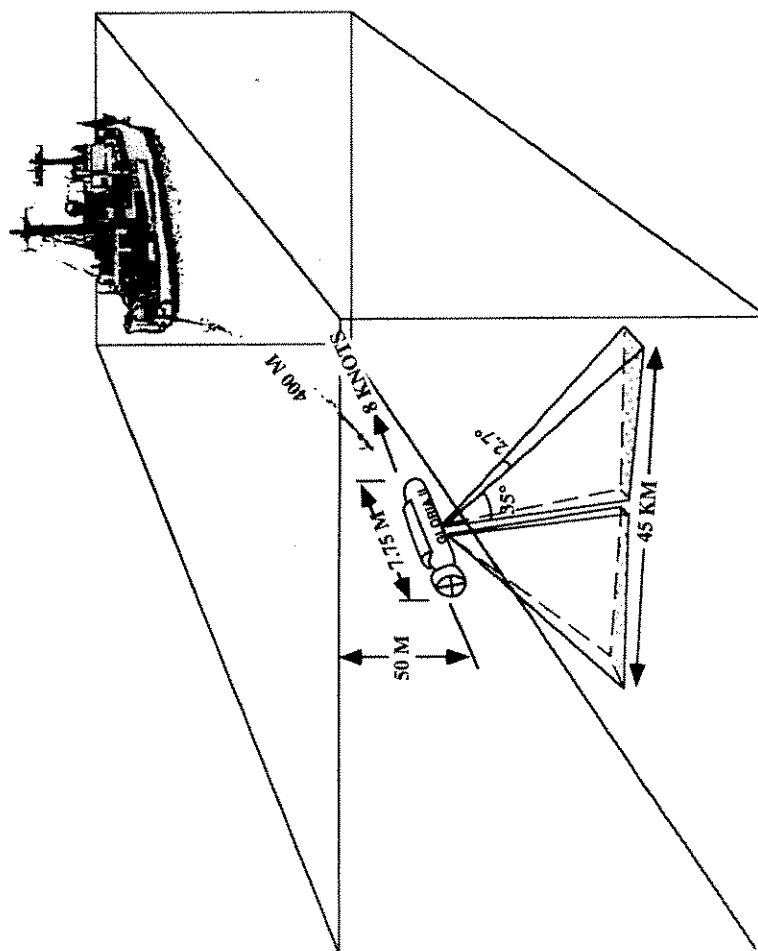


Figure 6-GLORIA II sidescan sonar (modified from EEZ-Scan 85 Scientific Staff, 1987).

is an active system using acoustical waves to produce images or so called sonographs (Sutton, 1979). The data used in this study were collected by GLORIA II, which is an updated GLORIA introduced in 1977. The near surface towed device is called a "fish." There are 120 transducers (30 to a row, 60 to each side) in the sonar array of the "fish." Each array is 5.3 m by 40 m. To avoid cross-talking between the acoustic pulses, the operating frequency on the port array and the starboard array are 6.0 kHz and 6.8 kHz, respectively. A 2 or 4 seconds long pulse is repeated every 20 to 40 seconds. The resulting acoustic beam is  $2.7^\circ$  wide in the horizontal and  $35^\circ$  in the vertical. The "fish" is towed about 400 m behind the ship. Towing depth depends on the towing speed. With a survey speed of 8 knots (15 km/hr), the "fish" depth is about 50 m. GLORIA is usually used in a water depth less than 4,000 m and the resulting swaths are up to 45 km wide (Chavez, 1986).

When the acoustic pulses generated from GLORIA II travel through the water column and reach the seafloor, these pulses were reflected and scattered back to the sidescan sonar. The received voltages are then converted to pixel values which are digital numbers (DNs) ranging from 0 to 255. In a continuous sidescan sonar survey, the 0-255 DN values are displayed in gray scale and the result is called a sonograph. Such sonographs are functions of the relief of the sea floor (height and gradient), the microtopography and roughness of the sea floor (e.g. sediment waves, and pressure features on submarine landslide deposits), and the physical properties of the sea floor (e.g. sediment type, degree of compaction, and induration) (Johnson and Helferty, 1990). The variation in DNs imply properties and the results of geologic processes of the seafloor. In GLORIA data, the high backscattered amplitudes are represented by high DNs or light tones, and the low backscattered amplitudes are represented by low DNs or dark tones.

Table 1 compares the physical specifications and capabilities of the Sea Beam and GLORIA II instruments. Since Sea Beam can be operated at 1.5 times the speed of

Table 1. Comparison chart between Sea Beam and GLORIA II (After Tyce, 1986; EEZ-Scan 85 Scientific Staff, 1987; Kleinrock, 1991)

System	Sea Beam	GLORIA II
Frequency (kHz)	12.158	6.2/6.8
Introduction	1975	1977
Pulse length	7 ms	2, 4 sec
Pulse rep. (sec)	1-22	20-40
Bandwidth (kHz)	0.14	0.1
Beamwidth (degree)	2.7 x 2.7	2.7 x 35
Array length	2.8 x 2.8 m	5.33 m
Vehicle length	hull mount	7.75 m
Weight (metric)		2.25 tonnes
Stabilization	all axes	heading
Data type	digital	digital
Tow depth	hull mount	30-60 m
Water depths	200-10,000 m	200-11,000 m
Cross track resolution	14-233 m	30 m
Along track resolution	233 m	218 m
Bathymetry accuracy	10-50 m	
Swath width	0.73 water depth	14-60 km
Survey speed	15 kts	10 kts
Number in use	12	2
Coverage (km <sup>2</sup> /day)	1,250	13,000



GLORIA II, and the swath width of GLORIA II is about 6 times that of the Sea Beam system in the study area, for the same period of time the coverage of GLORIA II can be more than 4 times that of the Sea Beam's.

The GLORIA II data released by NGDC (EEZ-Scan 85 Scientific Staff, 1987) has had both geometric and radiometric corrections applied (Chavez, 1986). The geometric corrections adjust spatial locations of the sonograph pixels and they include correcting water-depth offset, slant-range geometry, and aspect-ratio distortion. The water-depth offset correction subtracts the time the sonar signal travels through the water column. The slant-range geometry correction converts slant-range distance to true horizontal distance. The aspect-ratio distortion accounts for the different resolution in the along-track and across-track directions as well as distortion caused by ship speed variations.

The radiometric corrections adjust the DN values of pixels by applying shading correction and speckle-noise correction, as well as removing striping noise. The shading correction adjusts for the sonar energy attenuation in the across-track direction by applying a two-pass algorithm. The first pass removes low-frequency patterns. The second pass normalizes all data and allows comparing sonographs in the across-track direction. The speckle-noise and striping noise corrections remove artifacts in the sonographs. The speckle-noise correction uses a 2 by 2 smoothing filter. The removal of striping noise uses a combination of high- and low-pass filters (Chavez and Soderblom, 1974).

### **Geological settings and previous studies**

Although the Gulf of Mexico is a passive continental margin, the construction and evolution of the northwestern portion of the Gulf is very complex. The rugged morphology of the upper and lower continental slope off Texas and Louisiana are primarily influenced by underlying halokinesis of allochthonous salt along with rapid shelf edge sediment

progradation, sea level fluctuations, and mass movement. The bathymetric highs usually correspond with shallow salt (less than 1 second/sec two-way-travel-time/TWTT below seafloor), whereas the bathymetric lows correspond to sediment-filled intraslope basins (Bryant et al., 1990). Based on their relationship with the salt, these intraslope basins can be categorized as interdomal, interlobal, and supralobal, basins. Interdomal basins occur between isolated salt domes and are common across the shelf and upper slope. Interlobal basins are surrounded by coalescing salt canopies and are common on the upper and middle slope. Supralobal basins which are above the allochthonous salt and are formed by sediment downbuilding and salt withdrawal are common on the lower slope (Simmons et al., 1996).

There are four large canyons, two foldbelts, and a large escarpment on the lower continental slope of northwestern Gulf of Mexico. The Sigsbee Escarpment represents the southward depositional limit of autochthonous Louann Salt. Although most continental margin submarine canyons were formed by erosion during major sea level lowstands, Bryant, Keathley, Alaminos, and Rio Perdido Canyons were mainly influenced by the coalescing and migration of salt canopies. The NW-SE trending Perdido Foldbelt is a salt-cored compressional foldbelt that lies on an extensional detachment surface (Simmons et al., 1996). Another foldbelt, the Mexican Ridges are shale-cored large submarine slides (Winker, 1982; Bryant, 1991).

The geomorphologic and geological studies in the Alaminos Canyon can be summarized as follows. Treadwell (1949) first charted the seafloor bathymetry in the northwest Gulf continental slope, and attributed the irregular topography to slumping, folding, and faulting. Gealy (1955) outlined the bathymetry of Alaminos Canyon and attributed the hummocky topography to gravity-caused sediment failures. Uchupi (1968) mapped the re-entrant of the canyon. The same year, Bouma, Bryant, and Antoine (Bouma et al., 1968) used fathometer and single-channel high resolution record to map the canyon

area; they noted the terrace-like morphology of the canyon and gave it the name of Alaminos Canyon. Garrison and Berryhill (1970) speculated that the Alaminos Canyon might be formed by separate basins with coalescing salt fronts. Bouma et al. (1972) constructed a better bathymetric map of the Alaminos Canyon area; they observed thick and thin sand layers in the canyon, and speculated that these coarse sediments were transported to the canyon during Pleistocene sea level lowstands; they interpreted the canyon as the product of a complex history of faulting, folding, diapiric uplift, salt-front movement, and submarine erosion. Based on single channel seismic data, Bryant et al. (1990) described the canyon as a broad re-entrant that separates the rugged Texas-Louisiana continental slope to the east and relatively smooth seafloor to the west. Hardin (1989) and Mechler (1994) used multichannel seismic data and suggested that the canyon is in part the result of the coalescing salt canopies with the center portion of the canyon salt free. A more recent study by Trudgill et al. (1997) shows that the center of the canyon has salt at a depth of greater than 7 secs TWTT. The same year, Brown (1996) also reports on the deepest hydrocarbon drilling in the Alaminos Canyon area.

## CHAPTER III

### DATA PROCESSING AND EVALUATION

In this chapter, the procedures used in processing the bathymetry data, sidescan sonar data, and ground truth samples are illustrated. As all the data dealt with in this study have a spatial component, Geographic Information System (GIS) is used as a primary tool to take advantage of its built-in functionality and to facilitate the data processing. The GIS packages used in this study include Arc/Info (1997), ER Mapper (1995), GMT (Wessel and Smith, 1995), and GRASS (1993). The data analysis package, PV-WAVE (1994), is used to process the pre-georeferenced sidescan sonar data. C-programs are also coded to locate geographic coordinates for multibeam's sidebeams, process ground truth data, and make links between different computer packages.

#### Post-processing Sea Beam data

The full resolution soundings of the Sea Beam data were stored in a sequential fixed-length binary format. As the Sea Beam raw soundings only contain time, ship's heading, and location of the ship track, after restoring the binary data, the next step is to derive the location of the adjacent side beams. As the distance between each beam is in hundreds of meters, a planar earth is assumed:

$$\phi_R = \phi_0 - \frac{H \times \sin \theta}{\lambda_1} \quad (3)$$

$$\lambda_R = \lambda_0 + \frac{H \times \cos \theta}{\phi_1} \quad (4)$$

$$\phi_L = \phi_0 + \frac{H \times \sin \theta}{\lambda_1} \quad (5)$$

$$\lambda_L = \lambda_0 - \frac{H \times \cos \theta}{\phi_1} \quad (6)$$

where  $\lambda_L$  is the latitude of the left side beam,  $\lambda_R$  is the latitude of the right side beam,  $\phi_L$  is the longitude of the left side beam,  $\phi_R$  is the longitude of the right side beam,  $H$  is the horizontal distance of the side beam to the ship nadir in meters,  $\theta$  is the ship's heading,  $\lambda_1$  is the length of  $1^\circ$  latitude in meters, and  $\phi_1$  is the length of  $1^\circ$  longitude in meters.

The length of longitude and latitude are calculated based on the Clarke spheroid of 1866 (Bowditch, 1975):

$$P = 111,415.13 \cos L - 94.55 \cos 3L + 0.12 \cos 5L - \dots \quad (7)$$

$$M = 111,132.09 - 566.05 \cos 2L + 1.20 \cos 4L - 0.002 \cos 6L + \dots \quad (8)$$

where  $P$  is the length of  $1^\circ$  of the longitude in meters,  $M$  is the length of  $1^\circ$  of the latitude in meters, and  $L$  is the latitude in degrees.

As the sound velocity in sea water varies with temperature, salinity, and pressure, while Sea Beam uses sound velocity profiles to correct the horizontal distance away from the nadir but not the vertical distance which assumes a constant sound velocity 1500 m/sec, it is necessary to correct the depth of Sea Beam raw soundings. These depth corrections were first proposed by D. J. Matthew in 1927. Since then the Matthews' Tables have been

updated by Matthews (1939) and other authors (Charnock and Crease, 1966; Crease and Edwards, 1972; Greenberg and Sweers, 1972). The latest update was by Carter (1980) who divided the ocean into 85 areas. Although there may still have errors, but according to Matthews (1939), these errors should be much less than the error caused by the echo sounder, the slope of the sea floor, or the uncertainty of the ship's position.

There are 63,598 Sea Beam raw soundings in the Alaminos Canyon area. To reject the error depth acquired during data collection, a depth contour plot based on the raw soundings is generated. Based on visual examination, a short survey line (cb90apr12.d03) that overlaps with other survey lines shows messy clustering and is excluded. Some soundings appear much shallower than their surrounding soundings and are believed to be bad data points. To delete these bad data points, an algorithm used by Herlihy et al. (1992) is modified. Three criteria are used to recognize bad data points: a minimum of surrounding points, a deviation from the averaged sounding, and a tolerable variance. When a sounding is secluded and lies outside the range of an averaged value with a tolerance, this sounding is judged as bad data point and is excluded. In Herlihy's algorithm, the rejection process is performed during the data collection on a ping by ping basis. In this study, all raw soundings are georeferenced and converted to a 50 m spaced grid. These soundings then are judged by a moving window with a searching radius on a cell by cell basis.

(1) Minimum surrounding points:

Every valid sounding must have another five soundings (i.e. the minimum surrounding points used in this study is 6) in a searching radius. A searching radius of one and half times of the average Sea Beam one ping coverage is used:

$$2053.3 \text{ m (average depth)} \times 73\% \text{ (swath coverage)} \times 1.5 = 2248.4 \text{ m}$$

(2) Standard deviation:

In the searching radius, all valid soundings must be within the depth range of the averaged sounding in the searching radius  $\pm 2$  times the standard deviation.

(3) Besides the above two criteria, all valid soundings must also be in the range of the averaged depth of the searching radius  $\pm 10$  m.

The distance between depth soundings varies from 75 m to 120 m. After rejecting the erroneous depth data, the soundings are further gridded to a 50 m interval. In a gridding process, when the desired number of cells are smaller than the known values, averaging must be down. For the Sea Beam data in the Alaminos Canyon, as a fine resolution or the desired number of cells are larger than the known values, spatial interpolations need to be applied. There are many interpolation methods. Each has its advantages and disadvantages, and a bad interpolation can bias a feature's shape and misrepresent the topography. In this study, four popular interpolation algorithms are tested and evaluated: inverse distance weighting (IDW), minimum curvature with spline tension (MinCurv), triangulated irregular network (TIN), and kriging (Arc/Info, 1997; Smith and Wessel, 1990). Appendix B summarizes how these algorithms are calculated.

The IDW method assumes that observations are more similar to each other when they are more closely spaced. The estimated value is derived according to the distance from the known points, and more weight is given to closer points. The choice of weight can be inversely proportional to the power of the distance from the known points to the estimated point. In this study, a search distance of 250 m, and a power of 2 are used.

A spline or flexible ruler is often used to fit curves between data points in a 2-D environment. In a 3-D case, bicubic splines are most commonly used. The MinCurv method fits bicubic splines between control points and minimizes total squared curvature. This algorithm is analogous to using an elastic plate that passes through the known points.

One problem associated with this method is the occurrence of extreme inflection points. This study uses Smith and Wessel's (1990) algorithm which applies a tension parameter that eliminates the oscillations that are generally inherited from the minimum curvature method. The tension parameter controls the roughness of the surface from that of a thin plate or a bicubic spline (tension = 0) to membrane or a harmonic surface (tension = 1). In this study, a tension of 0.25 is used.

The TIN method uses adjacent nonoverlapping triangles connecting irregularly spaced points. The most popular triangulation method is the Delaunay triangulation which tries to make equilateral triangles. The TIN method is relatively fast, can exclude the areas that are not to be interpolated, and allows various resolution according to the density of known points. As TIN is a vector structure, to compare its result with other algorithms, the interpolated values are further rasterized in this study.

The geostatistical method, kriging, was developed by a French geomathematician Georges Matheron (1971) and a South African mining engineer D. G. Krige. Kriging gives a Best Linear Unbiased Estimate (BLUE) because it minimizes variance of errors—best, the estimate values are weighted linear combinations of the known data—linear, and it tries to zero the mean residual—unbiased. The method is based on the regionalized variable theory and assumes spatial variation is homogeneous throughout the whole area. There are two concepts of regionalized variable theory (Burrough, 1992). First, the spatial variation of variables can be divided into (a) a structural component, (b) a random but spatially correlated component, and (c) a random noise (residual error). Second, the existence of “stationarity of difference” and “variance of differences”, which means the expected or averaged difference between any two places,  $x$  and  $x+h$  that are separated by a distance  $h$ , will be 0 (i.e.  $E[Z(x) - Z(x+h)] = 0$ ), and the variance of variables for spatially correlated components only depends on the distance between them (i.e.  $E\{[Z(x) - Z(x+h)]^2\} = 2\gamma(h)$ ;  $\gamma(h)$  is called semivariance).



In this study, ordinary kriging (OK), universal kriging with a linear model (UKl), universal kriging with a quadratic model (UKq), and subdivided universal kriging with a linear model (SubUK) are tested. In the OK, no structural drift is considered, and a gaussian model is used to model the variogram in this study. In the universal kriging, a structure trend that represents the slope is considered. In the SubUK, the whole Sea Beam coverage is subdivided into 3 km x 3 km areas to compensate for the non-homogeneity of the study area.

To evaluate which interpolation method performs the best, one-two hundreds of the processed Sea Beam data or 233 random points in the Alaminos Canyon were temporarily removed before interpolation. The interpolated results or the estimated values at the removed locations are then compared with the true values. The differences between estimated and true values or residuals then are expressed by summary statistics. The mean absolute error (MAE) and mean squared error (MSE) are used to describe the measures of spread and mean of the residual distribution (bias) (Isaaks and Srivastava, 1989):

$$MAE = \frac{1}{n-1} \sum_{i=1}^n |\gamma_i| \quad (9)$$

$$MSE = \frac{1}{n-1} \sum_{i=1}^n \gamma_i^2 \quad (10)$$

where  $n$  is the number of samples, and  $\gamma_i$  is the difference between estimated value and true value.

## Post-processing GLORIA II data

The GLORIA II data released by NGDC has been corrected for both geometric and radiometric distortions. Figure 7 is the GLORIA II image of the study area extracted from a NGDC released  $2^\circ$  by  $2^\circ$  mosaic image. During the image cropping of the study area, the control points for georeferencing are the boundary of the  $2^\circ$  by  $2^\circ$  coverage. As a result, the locations of pixels in this cropped image are far from accurate. Some apparent artifacts exist in the image that are either acquired during data gathering, data processing, or mosaic generation. These artifacts include high DN values in the nadir, messy and low DN values in the near range, and unmatched tone in the upper right corner of the mosaic. There are also some systematic patterns that may be artifacts. These patterns include in the north of  $N26^\circ30'$  where consistent medium DN values occurred in the medium range, and some semi-irregular patches located between  $N26^\circ25'$  and  $N26^\circ20'$ .

The objectives in reprocessing the GLORIA II data are to differentiate dubious pixels from the true backscattered image, to have better geographic controls on the footprint, and to improve the quality of the image. Overall, the purpose is to enable reliable investigations when the GLORIA II image is combined with other geological and geophysical data. The procedures used in this study are mainly empirical and can be categorized into: correct messy DN values in the nadir and near range, histogram match adjacent image strips, georeference backscattered pixels, mosaic image strips, filter erratic DN values, and fill filtering generated voids.

For each GLORIA II sidescan sonar image strip used in this study, there are 892 pixels in the across ship track direction and more than 1,700 pixels in the along ship track direction. Figure 8(a) shows the perspective view of a portion of the NGDC released GLORIA II image strip in the Alaminos Canyon. Except for a few non-zero DNs in the very far range, the none-zero DNs are mainly between the 200th and 600th pixels across

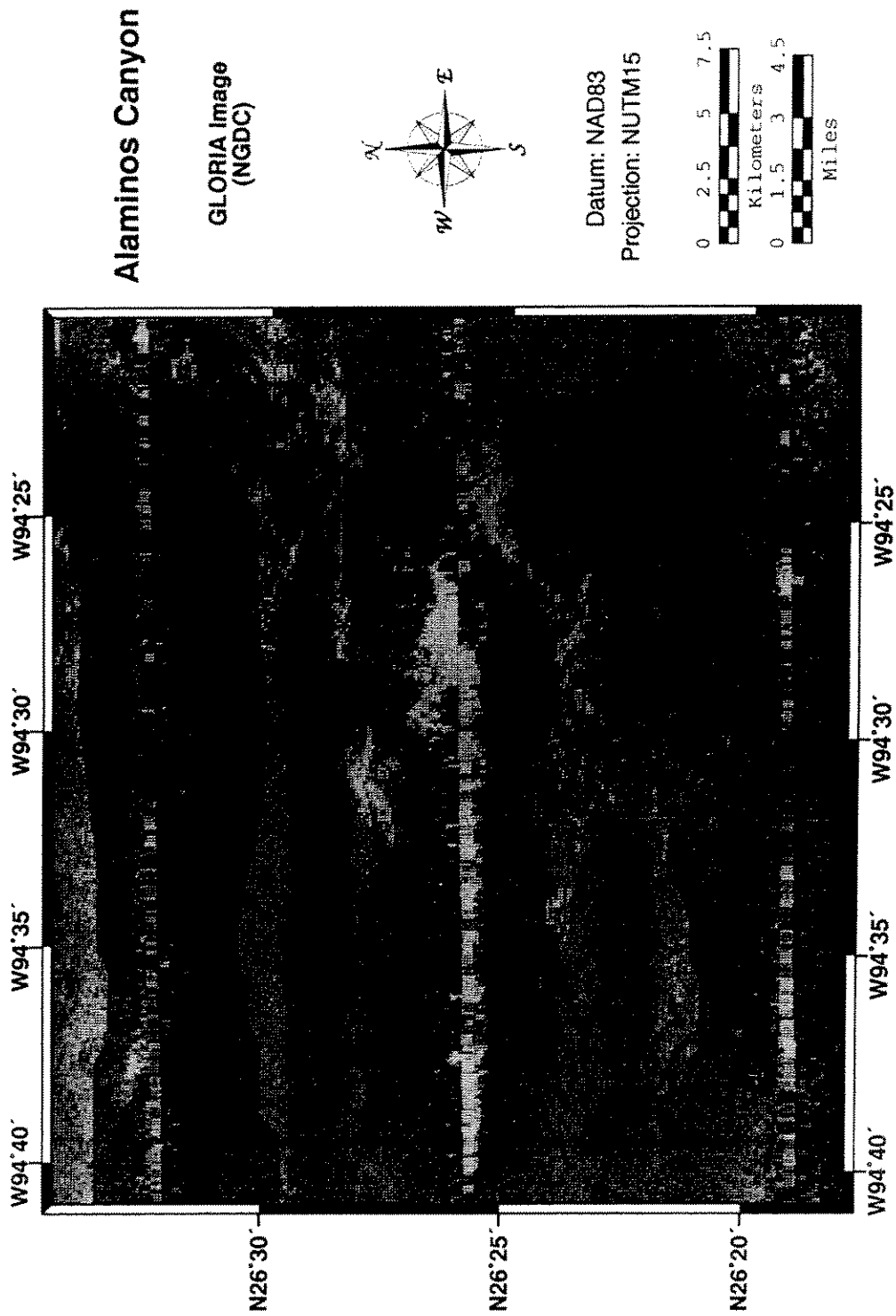
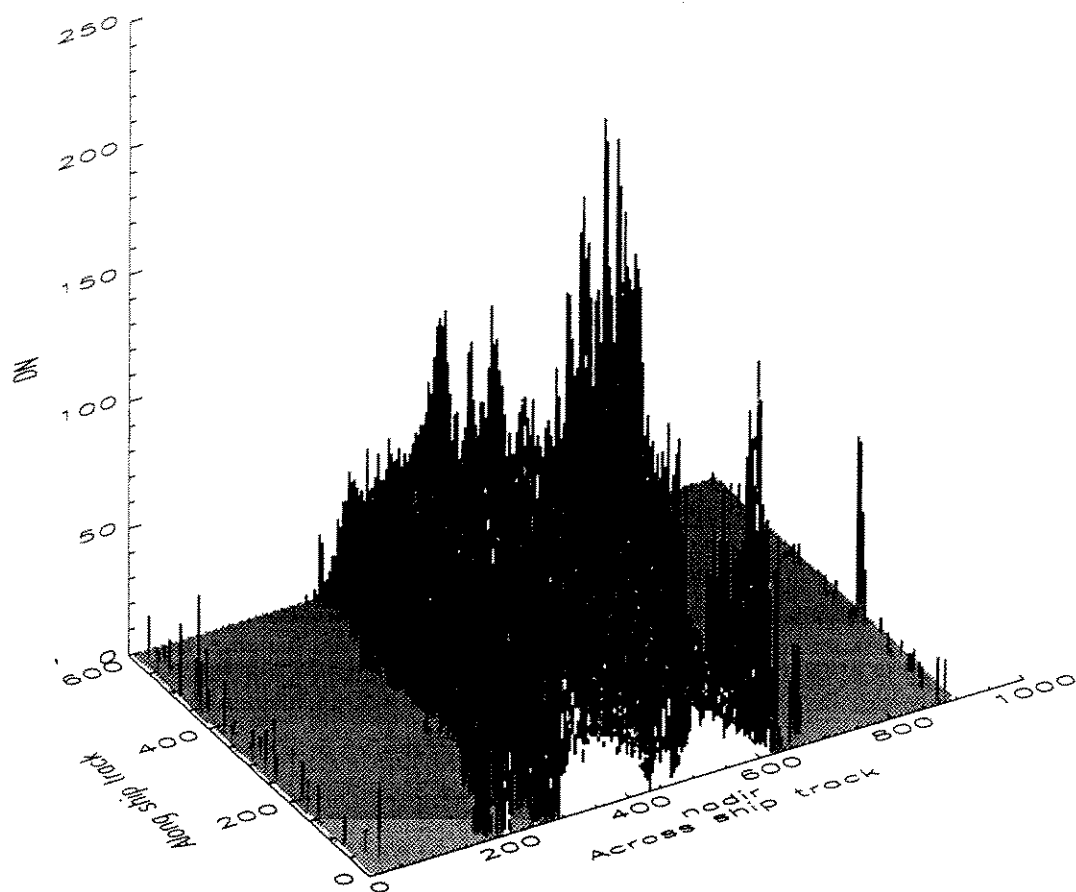
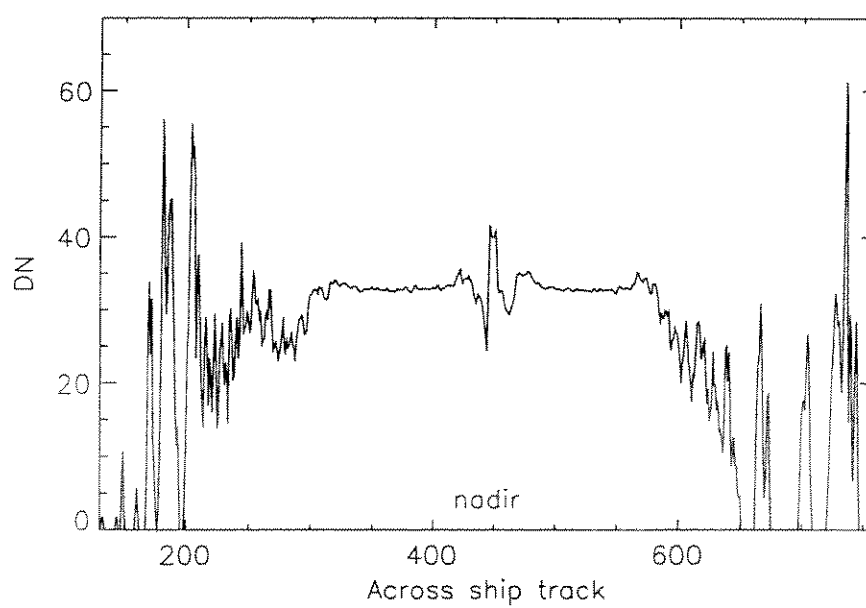


Figure 7-GLORIA II image in the Alaminos Canyon. Extracted from NGDC 2x2 degree image.



(a) Perspective view of DN values.



(b) Averaged DN values along columns .

Figure 8-DN values of a GLORIA II image strip.

the ship track. Along the outer range of the strip, the DN values are also relatively high. Figure 8(b) is the averaged DN values along each column. This typical sonar strip illustrates that the NGDC processed image is satisfying in the medium range. However, the DNs are erratically high in the far range. In the near nadir, the averaged DNs are relatively high (DN  $\approx$  40) and are surrounded by an abrupt drop (DN  $\approx$  25-30). Adjacent to the sudden DN drops are DN bumps (increase 4-5 DNs). The high DNs in the far range are usually not a concern, since these areas usually are covered by an adjacent image strip and can be easily deleted during the mosaic construction from the sonar strips. The main concern is how to compensate the distorted DNs in the nadir and near range.

After extracting the NGDC released GLORIA binary data, two methods have been examined for correcting the erratic DNs in the nadir and near range. The first method is similar to Chavez's "shading correction" (1986) to normalize average profile on a ping-by-ping basis. In this study, however, the normalized window is limited to the erratic nadir  $\pm$  70 pixels in the across ship track direction. The correction coefficients are first determined from the comparison of averaged DN values of the column and the averaged DN values of the nadir  $\pm$  70 pixels area:

$$C_i = \frac{\frac{\sum_{j=1}^{j=row} DN_{ij}}{N_c}}{\frac{\sum_{i=n-70}^{i=n+70} \sum_{j=1}^{j=row} DN_{ij}}{N_t}} \quad (11)$$

where  $C_i$  is the correction coefficient for column  $i$ ,  $DN_{ij}$  is the DN value for column  $i$  and row  $j$ ,  $n$  is the column index of the nadir,  $N_c$  is the number of DNs that is non zero in a column, and  $N_t$  is the number of DNs that is non zero in the whole nadir  $\pm$  70 pixels area. The correction coefficient is then multiplied by individual DN to generate the new DN.

As the DNs in the nadir and near range are either higher or lower than the averaged DNs, the second method is to extract the problematic DNs and tune them to a similar DN distribution as in the "trusted" area. In this approach, the problematic DNs are defined as DNs larger than 200 or less than 50, and are located in the nadir  $\pm 70$  pixels across the ship track direction. The "trusted" DNs are defined in the range of nadir - 130 pixels to nadir - 70 pixels and nadir +70 pixels to nadir +130 pixels. The histogram of the problematic DNs is adjusted and matched to the histogram of the "trusted" DNs. The newly adjusted DNs for the problematic area are then used to replace the original DNs, and a histogram matched sonar strip is generated.

Each sonar strip has a different distribution range of DNs which may cause differences in tone as shown in the upper right corner of Figure 7. Histogram matching is applied again to adjust the tone changes in adjacent sonar strips. Each image strip is then projected to geographic coordinates with the same method used in projecting side beam locations for the Sea Beam data. As GLORIA does not record the heading of the fish, the fish's position is assumed to be the same as the ship's heading, and the GLORIA sonar is assumed to scan at perpendicular to the ship's course. To stabilize the abrupt change in fish's heading, the current ping location and its following four pings' locations are averaged as the heading.

During the mosaic of image strips, a buffer of 2,500 m on the port side and 1,500 m on the starboard side are assigned. Outside the buffered area, the georeferenced DNs are deleted to eliminate the redundant and dubious far range DNs. For the aspect ratio, traditionally GLORIA data duplicate DNs in the along ship direction to account for the distortion of footprint size caused by the speed changes of the ship and fish. In this study, instead of using duplicate pings, the georeferenced DNs are interpolated to account for the distortion of aspect ratio. To avoid systematic interpolated patterns, like in the nadir, introduced by most interpolation methods, the minimum curvature surface method with

spline tension is used. The composite image is further filtered for the nadir no data or noisy zone. A method modified from Chavez (1980) is used where the nadir DNs are compared with their surrounding averaged DNs. When the difference exceeds or is lower than a threshold, these values are excluded. The thresholds used here are 230 and 10. To fill the voids after the filtering, two methods were tested. First, the voids are filled with a cubic spline function across the ship track. Second, the voids are filled with randomly sampled DNs with a radius 60. The reason for using these randomly sampled DNs instead of using some interpolation method is that these voids usually are not predicable or do not follow a specific pattern.

### **Ground truth measurements**

P-wave velocity and gamma-ray density of cores were measured using the "Multi-Sensor Core Logger" at 1 cm interval downcore. The P-wave velocity is calculated from the distance between transducers and the time for a 500 kHz pulse to reach the receiver from the transmitter:

$$V = \frac{D + d - 2w}{T - X} + 3(20 - t) \quad (12)$$

where V is the velocity of sound through the sediment at 20°C, D is the core diameter, d is the core diameter deviation, w is the liner thickness, T is the measured P-wave travel time, X is the P-wave time delay caused by the liner, and t is the logging temperature in °C. The term "3 x (20 - t)" is used to correct the measured sediment velocity to 20°C.

The empty liner used for velocity and density calibrations has a diameter of 74.57 mm and thickness of 2.47 mm. The P-wave time delay is calculated from a distilled water-filled liner:

$$X = T_w - \frac{D + d - 2w}{V_w} \quad (13)$$

where  $X$  is the P-wave time offset caused by the liner,  $T_w$  is the measured P-wave travel time of the distilled water, and  $V_w$  is the distilled water velocity at 20°C. During the experiment, the water temperature used for calibration is 21.3°C, which gives a velocity of 1495.34 m/sec. The resultant P-wave time delay is 9.6 micro sec.

The gamma ray density is measured using a 10 milli-curie  $^{137}\text{Cs}$  source and counting the number of electrons received by the receiver. Aluminum plates are used to calibrate the gamma ray count and convert the count to density:

$$\rho_{bc} = \frac{\frac{\ln G_m - \text{Intercept}}{\text{Slope}}}{D + d - 2w} \quad (14)$$

where  $\rho_{bc}$  is the “corrected” wet-bulk density measured from the gamma-ray device, and  $G_m$  is the measured gamma-ray count. The aluminum plates calibration gives a slope value of -0.0067 and an intercept of 9.0442.

The calibrated density is then corrected for the attenuation differences from standard quartz (Boyce, 1976):



$$\rho_b = \frac{(\rho_{bc} - \rho_{fc})(\rho_g - \rho_f)}{(\rho_{gc} - \rho_{fc})} + \rho_f \quad (15)$$

where  $\rho_b$  is the true wet-bulk density,  $\rho_{fc}$  is the “corrected” fluid density,  $\rho_g$  is the true grain density,  $\rho_f$  is the true fluid density,  $\rho_{gc}$  is the grain density. In the calculation, parameters assumed are  $\rho_{fc} = 1.128 \text{ g/cm}^3$ ,  $\rho_g = 2.65 \text{ g/cm}^3$ ,  $\rho_f = 1.025 \text{ g/cm}^3$ , and  $\rho_{gc} = 2.65 \text{ g/cm}^3$ .

Before final graphing, some unreasonable low readings are excluded. The unreasonable velocity readings usually occurred at both ends of each core section where disturbance and poor acoustic coupling occurred. A velocity of 1,400 m/sec is used as a minimum sediment velocity. The density measurements are quite consistent between each core section. The sea water density of  $1.025 \text{ g/cm}^3$  is used as a minimum density. Appendix C is a C program for calculating the physical properties from the multi-sensor logger exported file.

## CHAPTER IV

### RESULTS AND DISCUSSIONS

#### Sea Beam filtered results

After projecting side beams to geographic coordinates, a preliminary bathymetric contour is plotted based on these raw soundings (Figure 9). The contour map shows that the shape of the canyon is well defined by the raw data, but there are some dubious contour lines. In the northwest and southwest portions of the canyon, the dense contour lines are caused by shallow depth soundings, and in the southeast portion of the canyon, the ambiguous depths are caused by a short survey line (cb90apr12.d03). Figure 10(a) is the depth histogram of the raw soundings. There are 63,598 soundings with depths varying from 37m to 2,672 m. The majority of the soundings are between 2,700 m and 1,400 m. A few soundings with depths shallower than 1,000 m are apparently noise.

After rejecting the short survey line (cb90apr12.d03) and applying the filtering algorithm described in Chapter III, the number of soundings is reduced to 60,797 points. The questionable contour lines no longer exist while the rest of the bathymetry remains intact (Figure 11). Figure 10(b) is the histogram of filtered soundings. During the filtering, not only the depths shallower than 1,400 m are rejected, but some extreme depths are also removed. After the filtering, the highest frequency of occurrence at 2,700 m is about 120 instead of 130. There are three modes in the depth distributions. A location query based on these modes show that the 2,700 m to 2,100 m depths fall inside of the canyon, the 2,100 m to 1,650 m depths cover the outside of the canyon, and the 1,650 m to 1,400 m depths cover a very small portion in the upper right corner of the canyon.

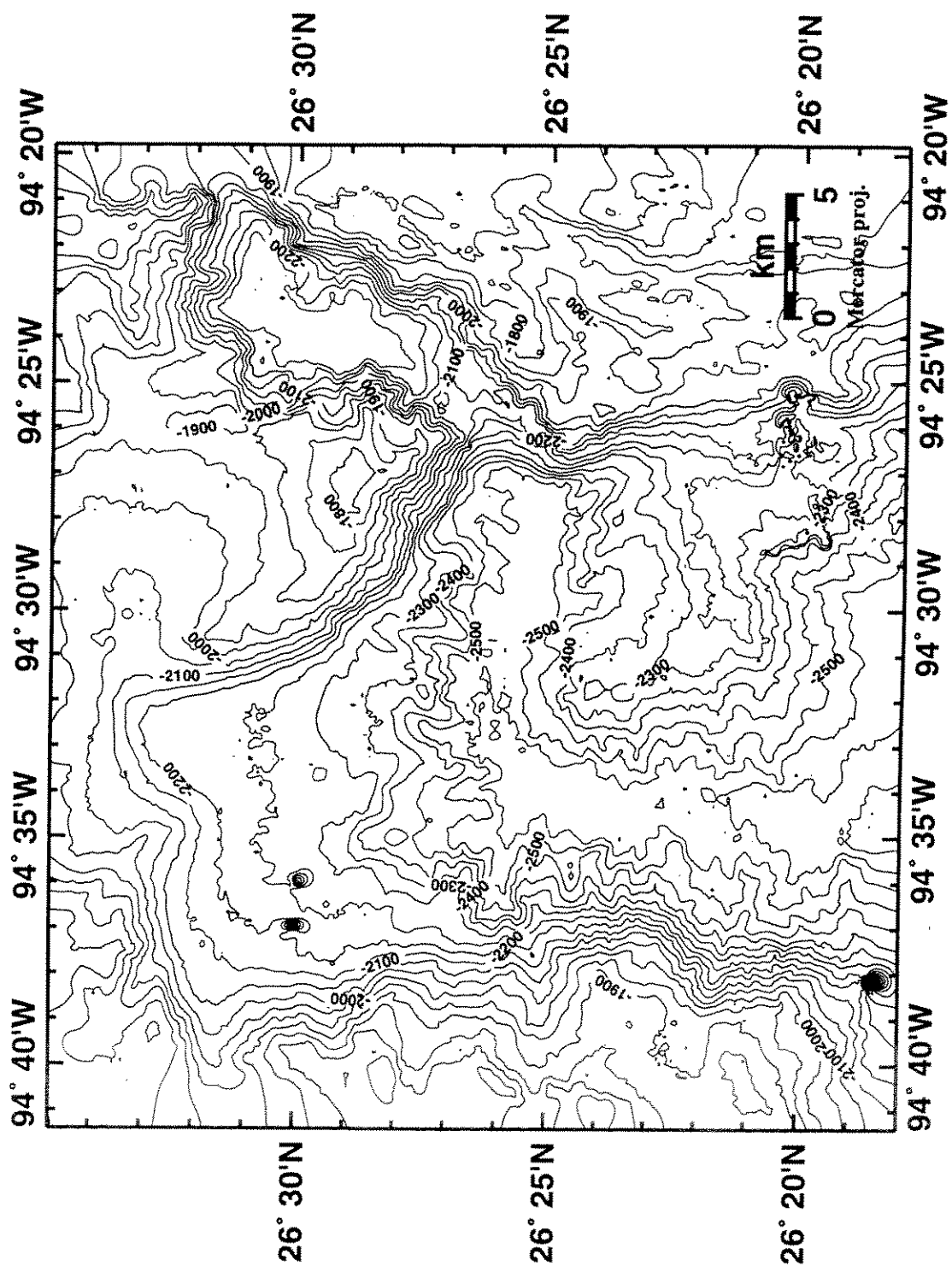


Figure 9-Unedited Alaminos Canyon bathymetric contour map. Contour interval 50 m.

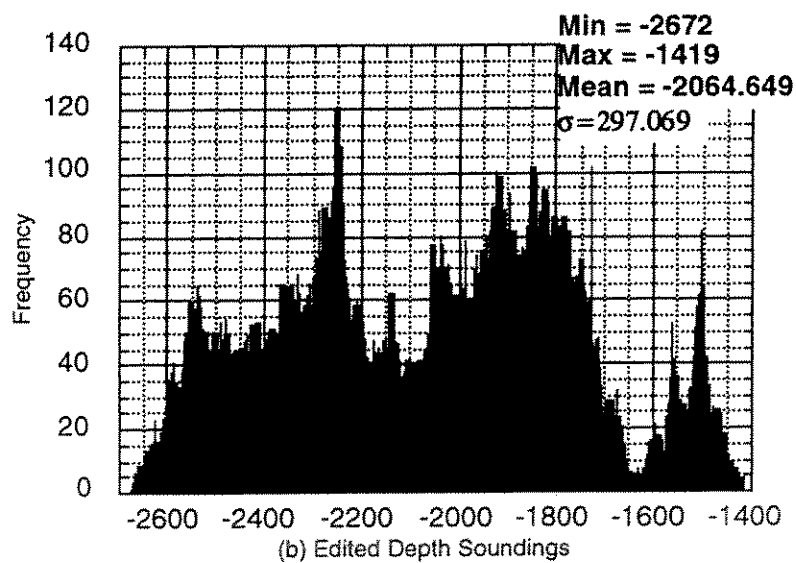
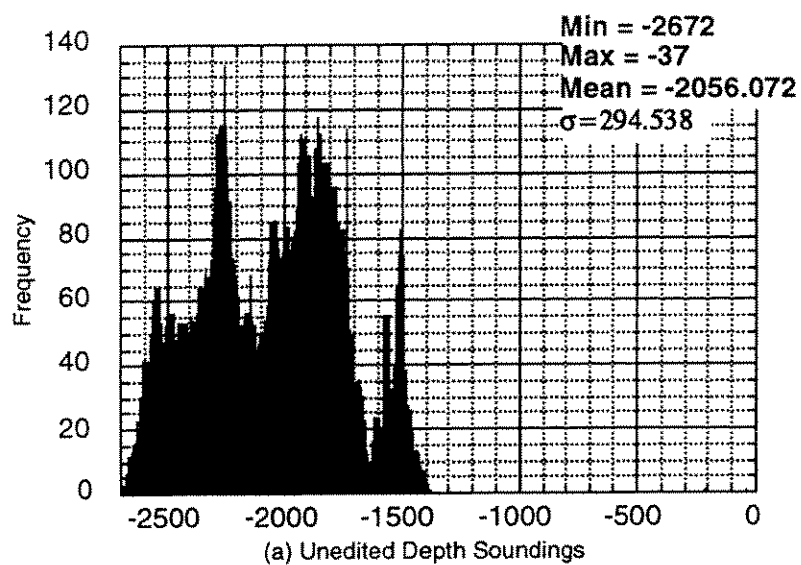


Figure 10-Histograms of Sea Beam depth soundings.

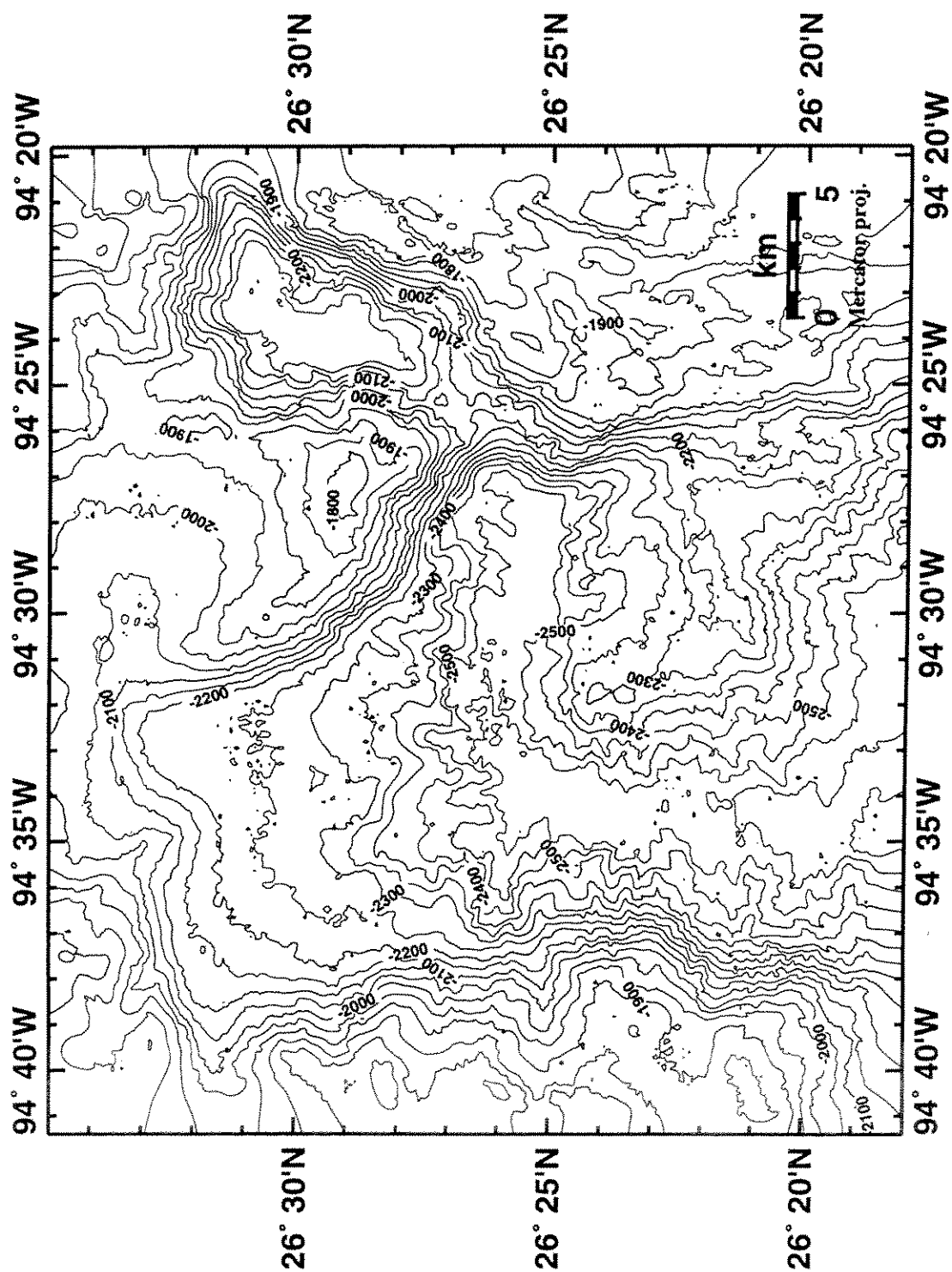


Figure 11-Edited Alaminos Canyon bathymetric contour map. Contour interval 50 m.

To evaluate the effectiveness of the algorithm used to reject the erroneous soundings, the contours generated from the edited soundings are overlaid with the contours generated from the unedited soundings. Figure 12 shows the edited soundings contoured at -1650, -1750, ..., -2750 m, while the original soundings contoured at -400, -500, ..., -2700 m. Except the areas where soundings are rejected, these contours appear to conform well with each other. Areas with some nonconformity include the southwest and southeast portions of the canyon where inaccurate shallow depths and clustered soundings are located. Other areas that have unnatural looking contours are on the canyon rim. In the re-entrant in the northeast area of the canyon, a major portion of the soundings are rejected which causes the edited and unedited contours to cross over each other.

The technique used in this study is not the only way to reject “erroneous soundings.” Other methods, for example, based on the regional slope gradient, can also be used. However, to maintain consistency in filtering out the doubtful soundings as used during regular Sea Beam surveys (Herlihy et al., 1992), this study successfully uses similar criteria after the raw soundings have been collected.

### **Gridding algorithms**

Unlike traditional 3.5 kHz or 2-D seismic surveys which generate one bathymetry sounding in each ping, the Sea Beam echo sounder system generates sixteen soundings. Because of the high density of the data, the bathymetry data released by NGDC has been averaged to 15 seconds and 250 m UTM grids. To fully utilize the recorded bathymetry data, spatial interpolation instead of averaging are required. For a dense data set, contours generated from different gridding algorithms may not show major differences. This is because the output differences between different algorithms are well below the contouring intervals; however, locally these differences can be significant.

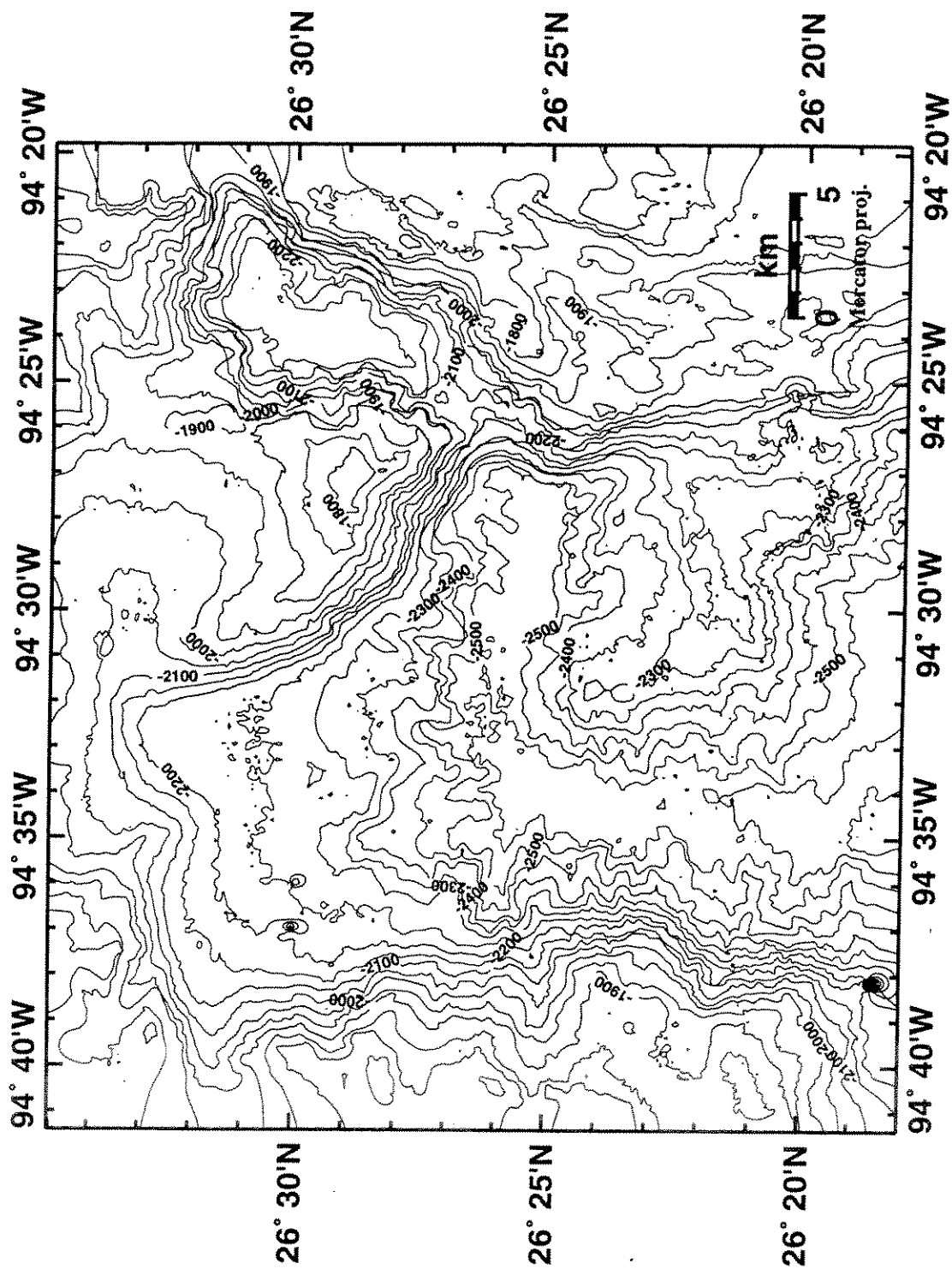


Figure 12-Alaminos Canyon bathymetric contour map. Unedited contours are in 100 m interval and annotated, while the edited contours lie in between of the unedited contours.

As we are inferring unknown depths based on known depths, the validation method used in this study excludes a portion of the known depths, then uses different interpolation algorithms and compares the estimated depths with the excluded true depths. Figure 13 shows the one-two hundreds of randomly chosen depth soundings used to test and validate different gridding algorithms. Figures 14-20 are the contour maps of the residuals overlying the 50 m bathymetry contour map. Figures 21-22 are the distributions and summary statistics of the residuals.

The IDW method is the simplest and least time-consuming algorithm in interpolation. This algorithm also shows the greatest variability in the estimates—31.5 m to -35 m (Figures 14 and 21). The extreme values are located in the west and northeast of the canyon. In the west of the canyon wall, the negative residuals extend about 1 minute in diameter. In the re-entrant in the northeast of the canyon, the residuals are much wider (about 3 minutes) and include both positive and negative values. The MAE and MSE, having values of 6.2 and 73.4 respectively, are the greatest among all examined. The greater and wider residual distribution can be explained by the IDW method deriving unknown points as a function of distances from adjacent known points, such that the distance between the known and unknown points and the values of the known points greatly influence the interpolated value. Although there are some variations of the IDW method, like applying different weights and powers to make the influence of surrounding points less or more prominent (Lancaster and Salkauskas, 1975), several problems still exist. First, the IDW method assumes that the interpolated surface is isotropic and the weight is only related to distance. When the sampling distance is greater than the interpolated distance, the result may not be satisfying. Second, the IDW method is a smoothing algorithm. The interpolated values can only fall between the known values, and the maximum and minimum values can only occur at known points. Third, the choice



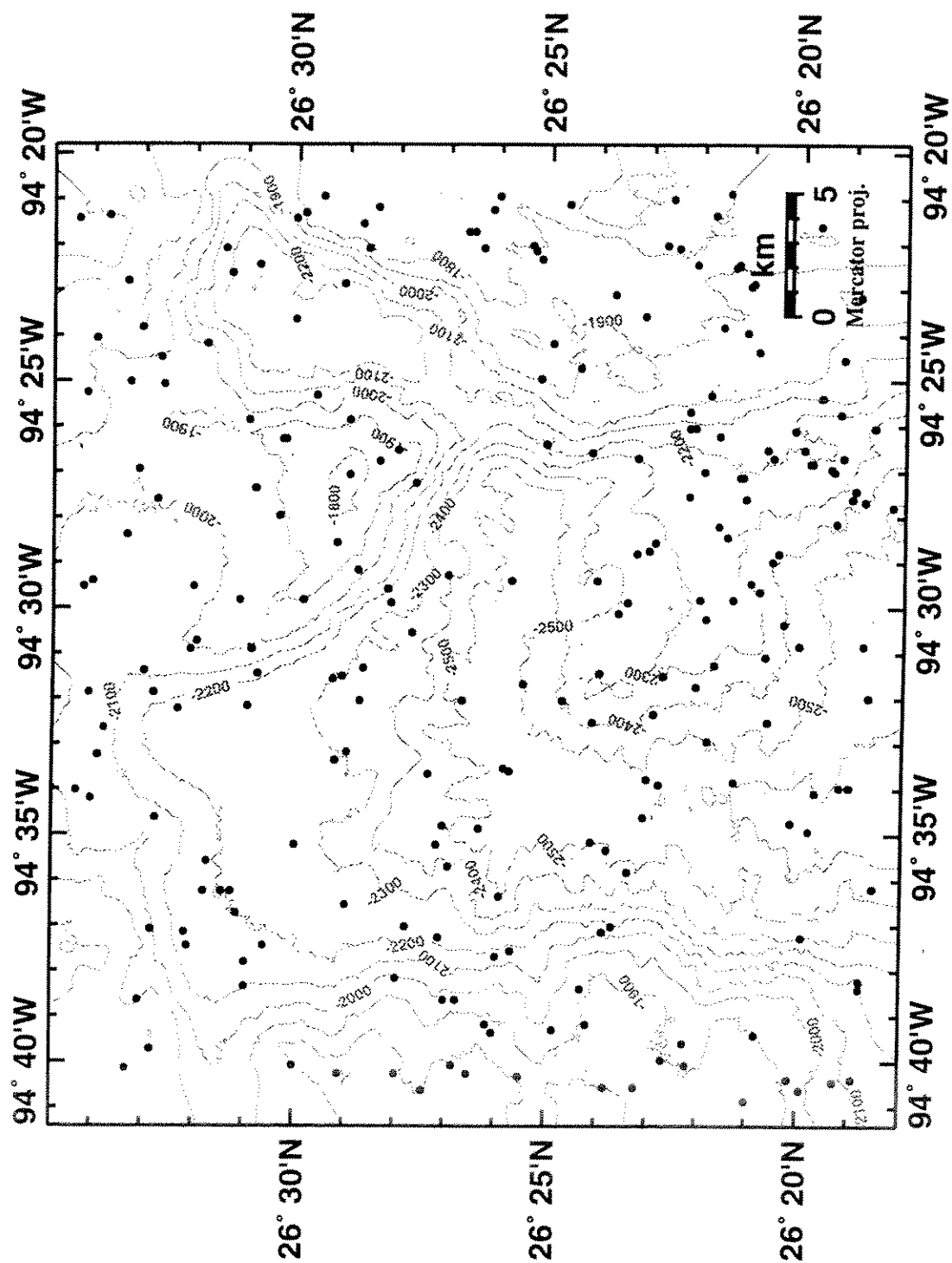


Figure 13-Locations of randomly selected 233 validating points.

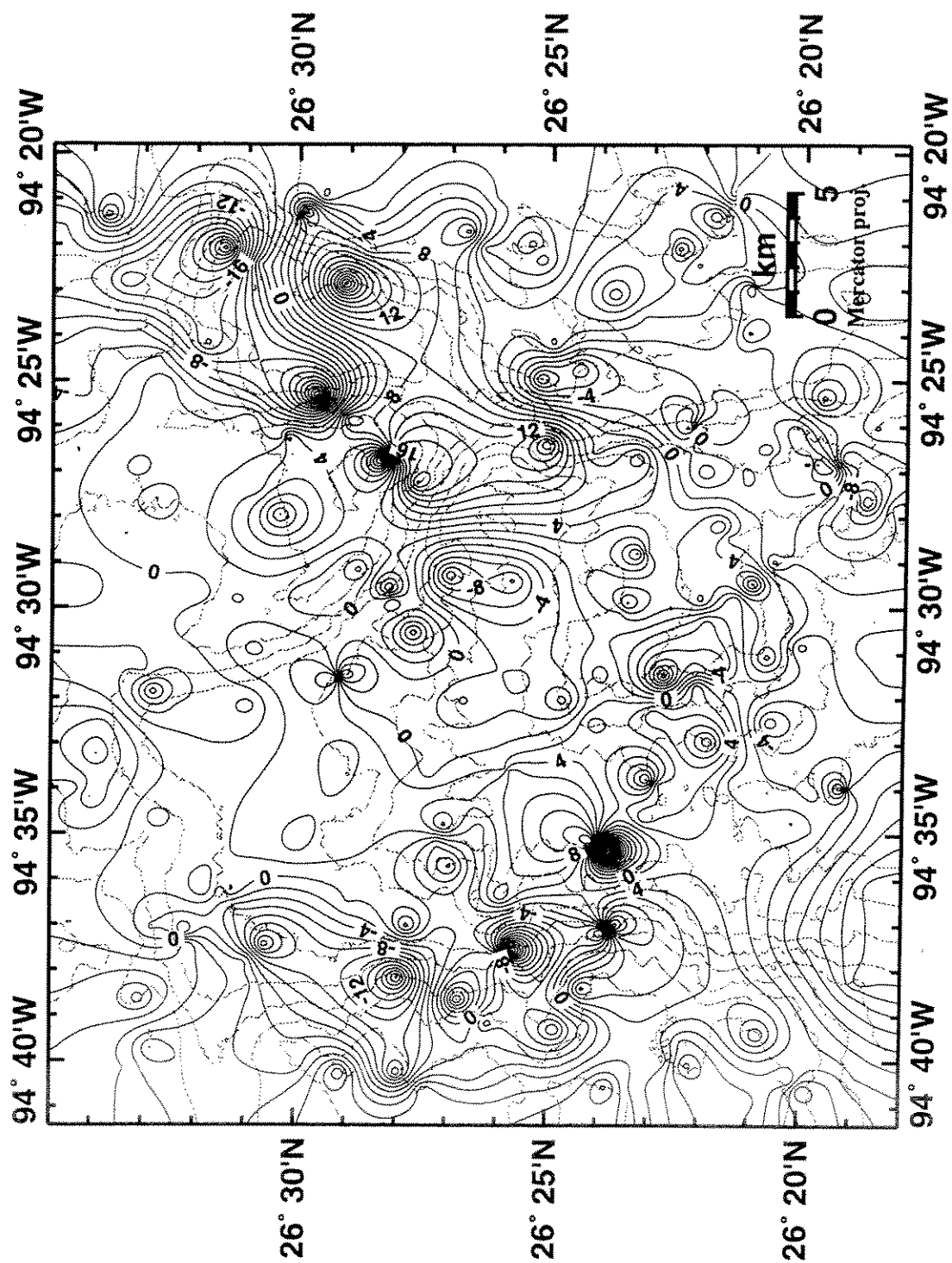


Figure 14-Depth sounding residual contour map-IDW (inverse distance weighting) method. Contour interval 2 m.

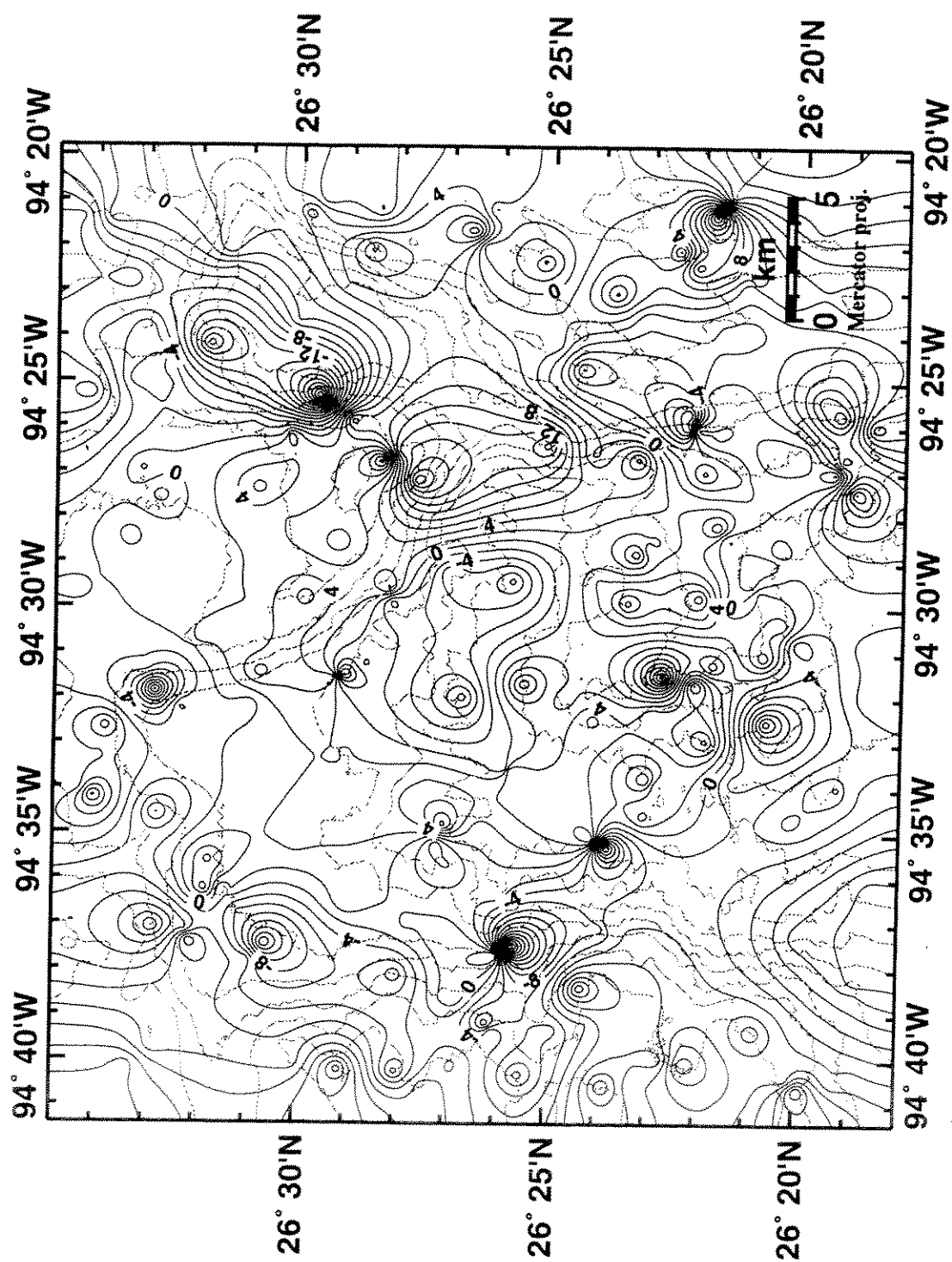


Figure 15-Depth sounding residual contour map-MinCurv (minimum surface curvature) method. Contour interval 2 m.

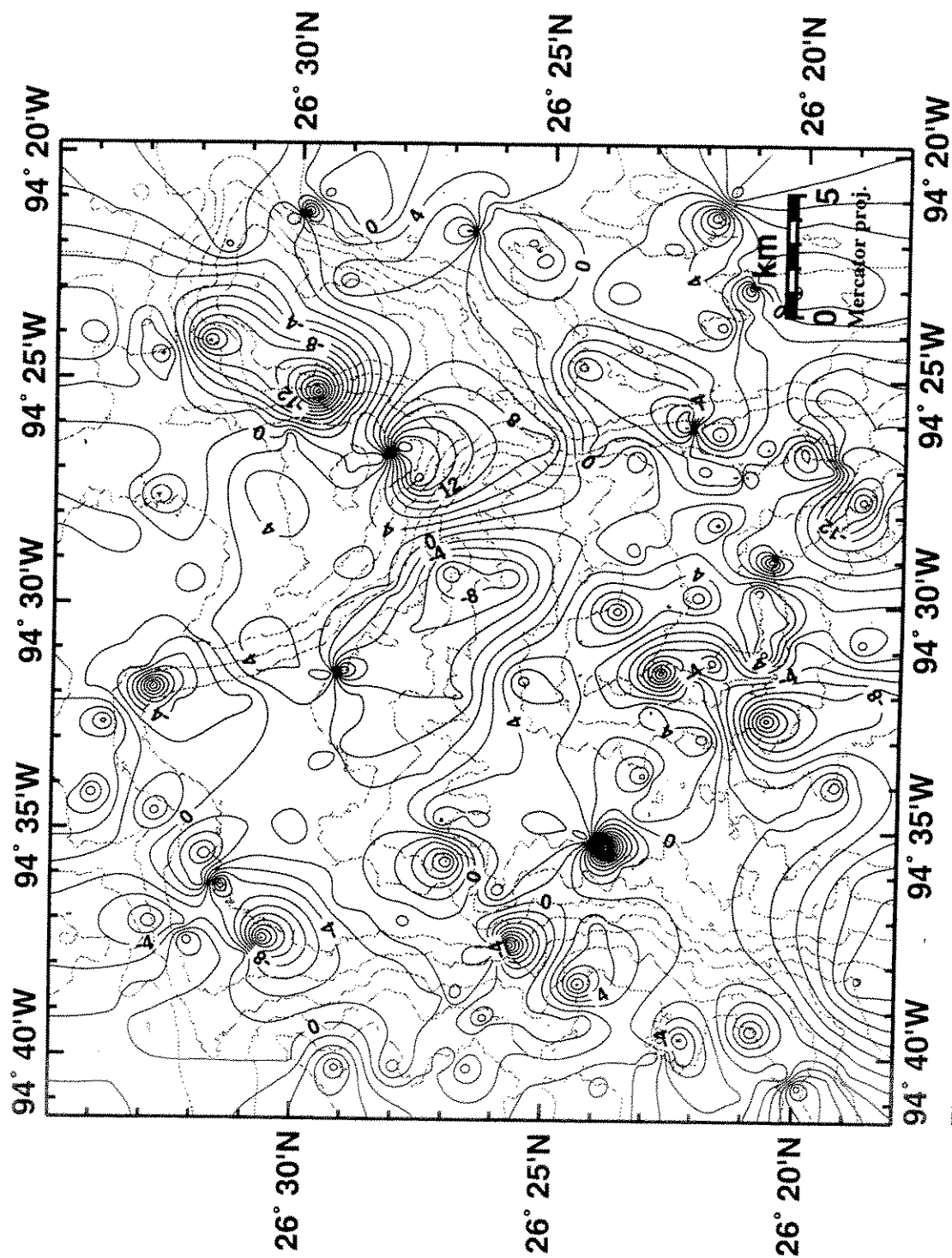


Figure 16-Depth sounding residual contour map-TIN (triangulated irregular network) method. Contour interval 2 m.

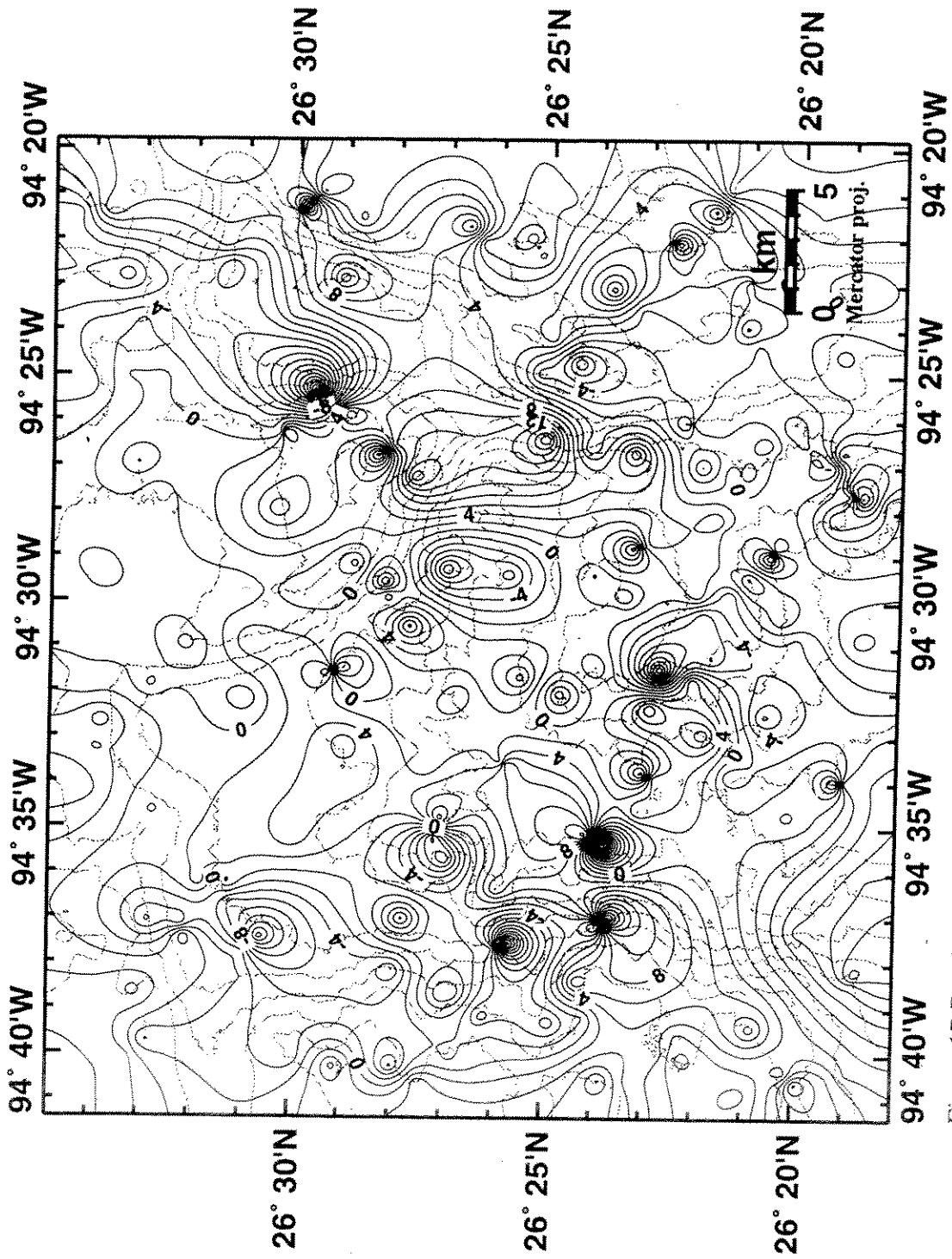


Figure 17-Depth sounding residual contour map-OK (ordinary kriging) method. Contour interval 2 m.

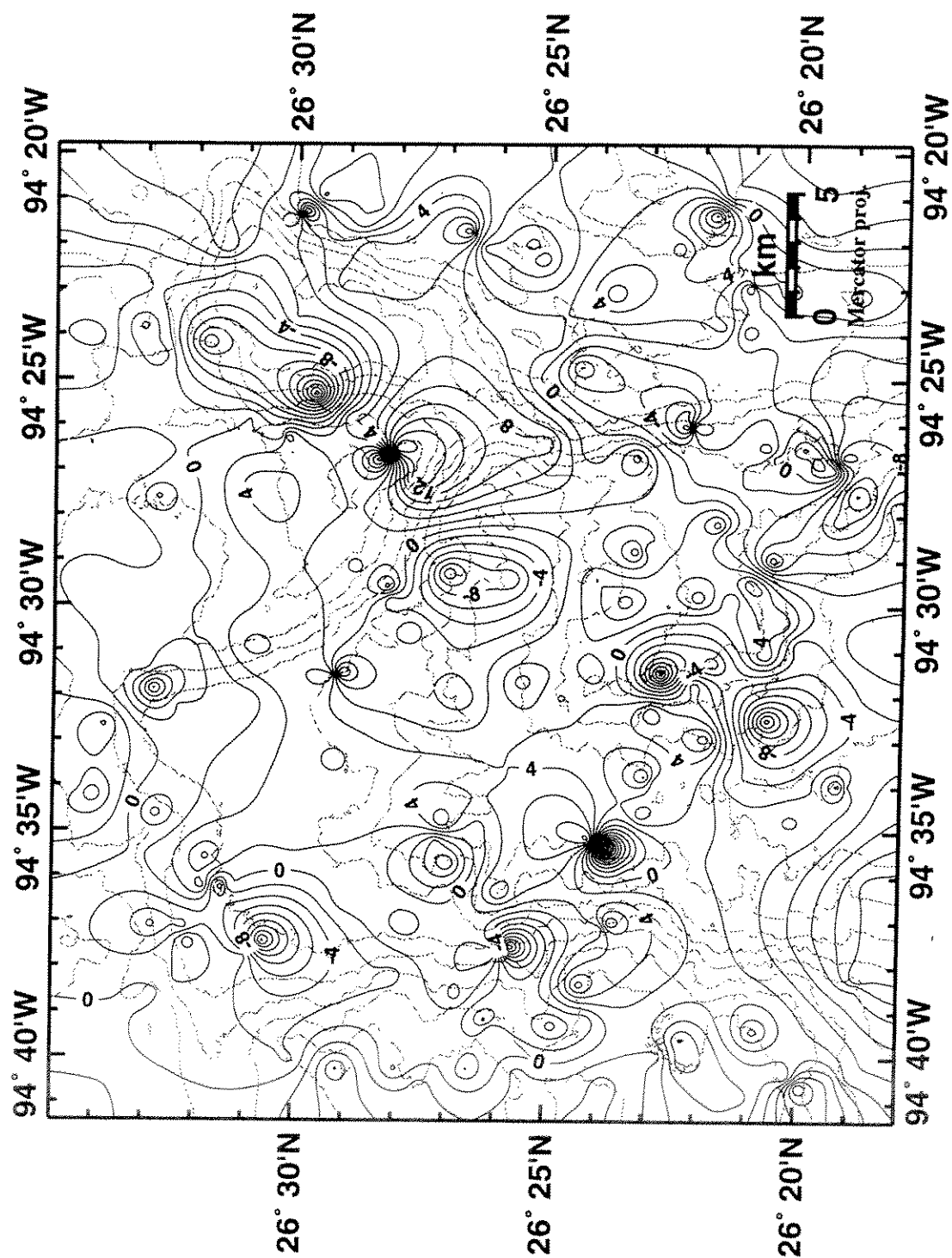


Figure 18-Depth sounding residual contour map-UKI (universal kriging method with a linear model). Contour interval 2 m.

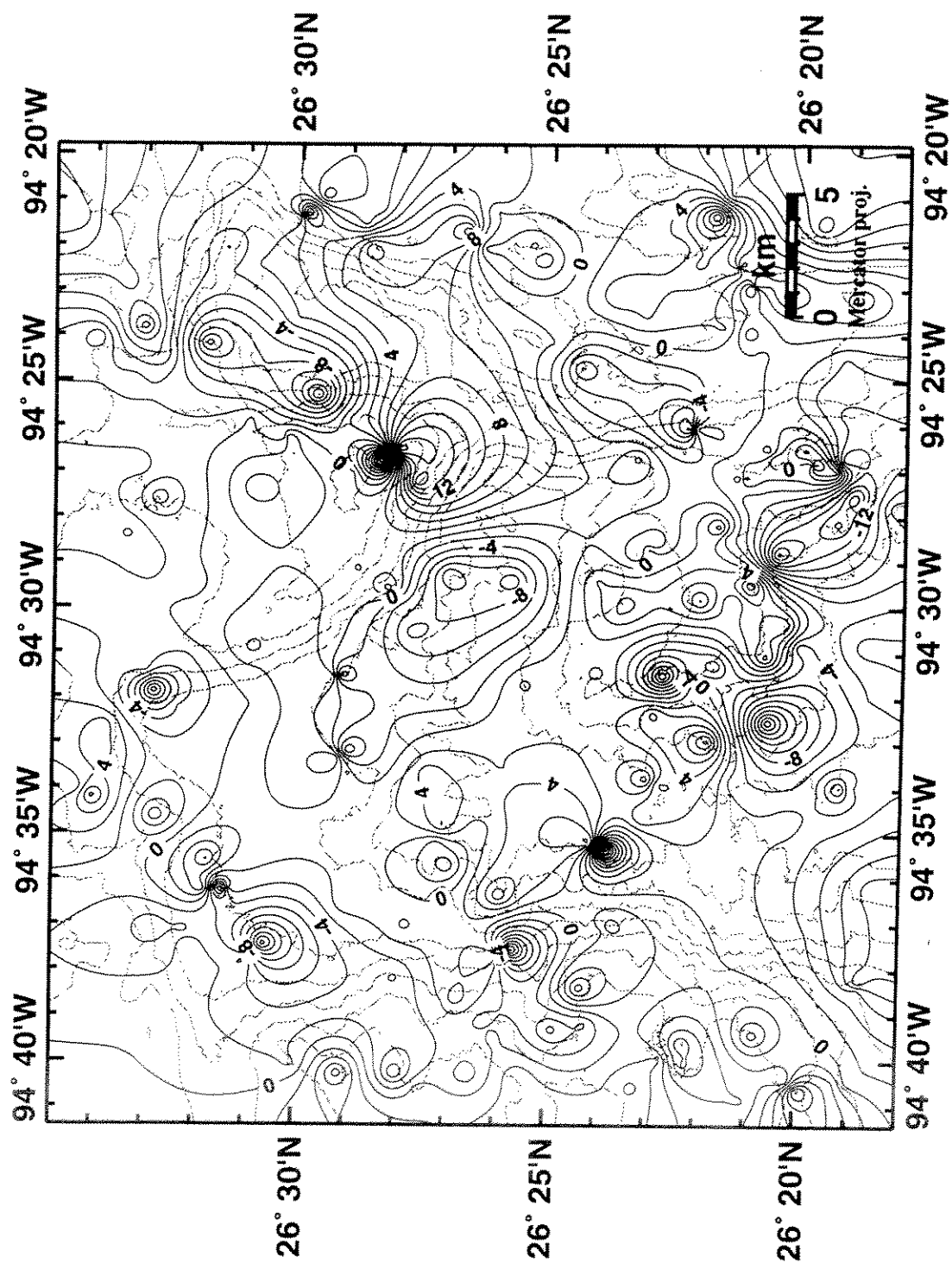


Figure 19-Depth sounding residual contour map-UKq (universal kriging method with a quadratic model). Contour interval 2 m.

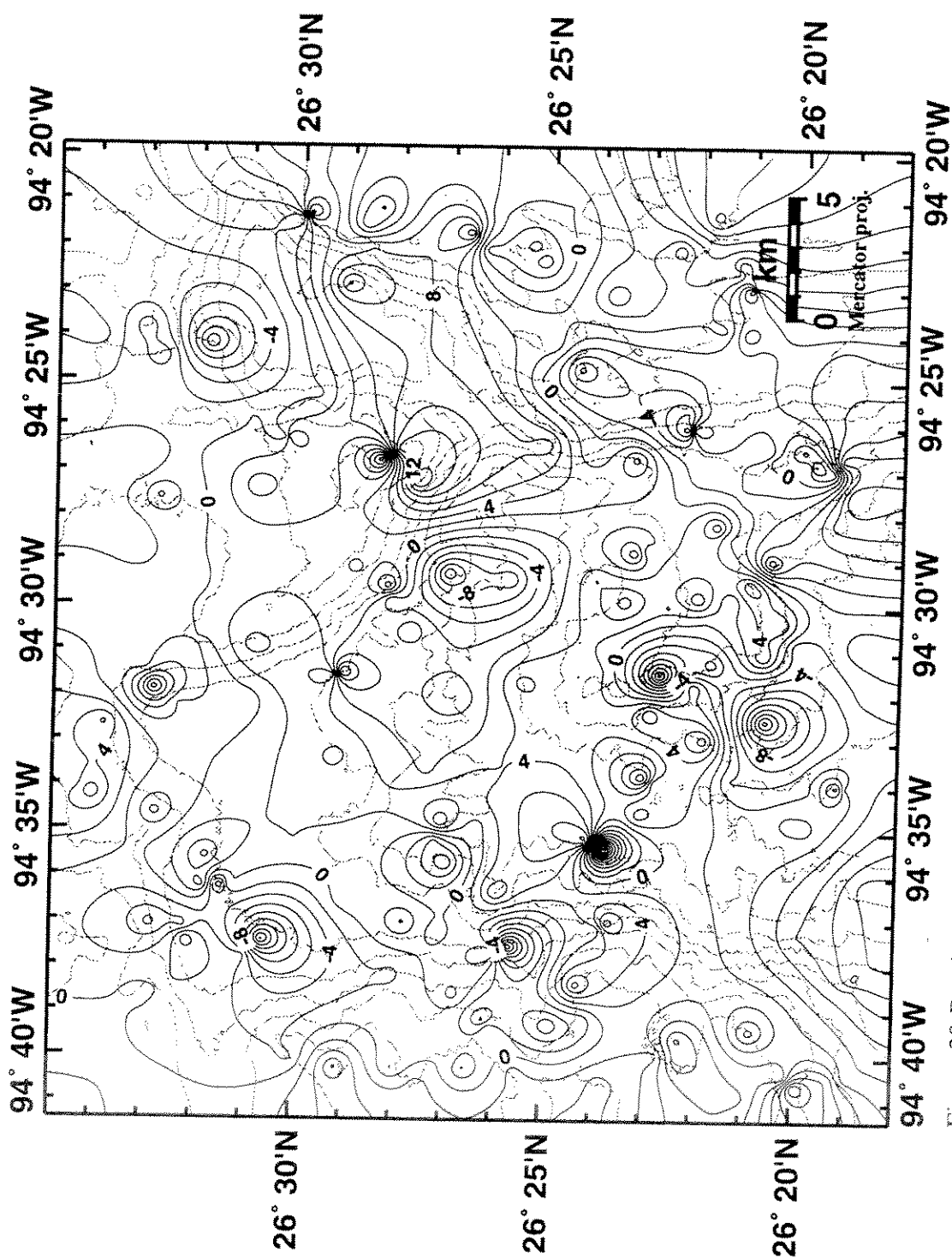


Figure 20-Depth sounding residual contour map-SubUK (subdivisoned UK method with a linear model). Contour interval 2 m.



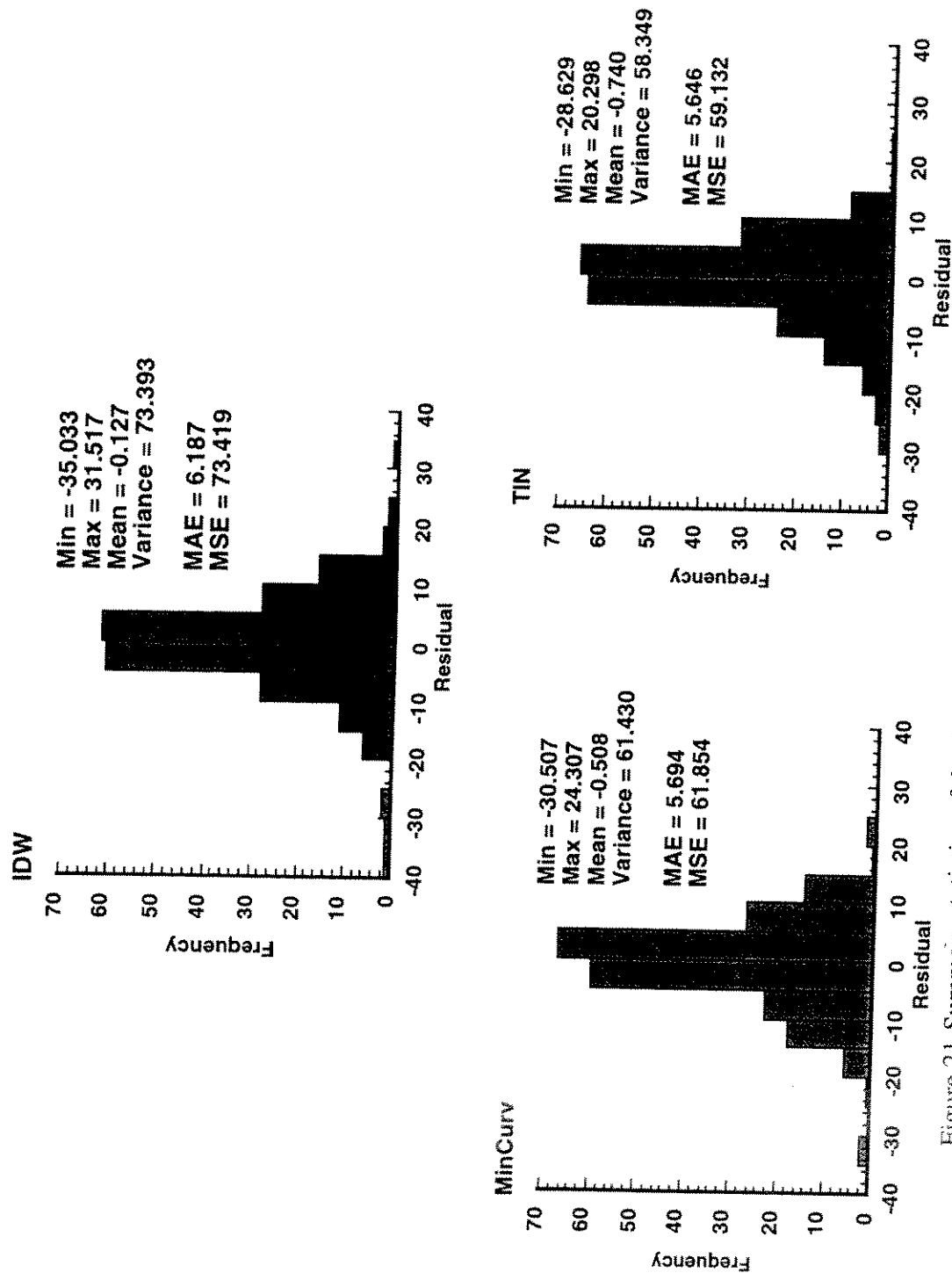


Figure 21-Summary statistics of depth sounding residuals based on IDW (inverse distance weighting), MinCurv (minimum surface curvature), and TIN (triangulated irregular network) methods.

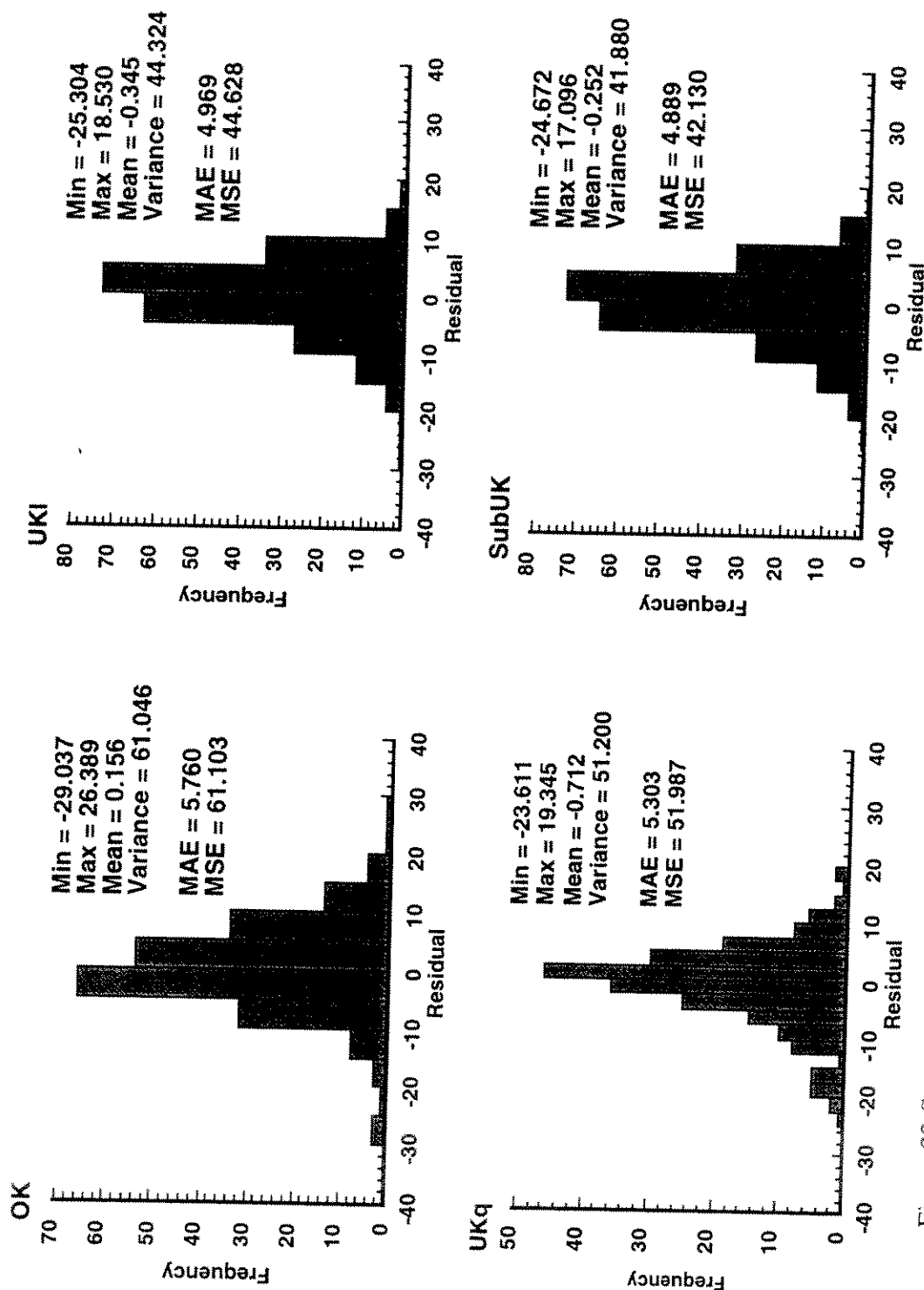


Figure 22-Summary statistics of depth sounding residuals based on kriging methods. OK is ordinary kriging. UKI is universal kriging with a linear model. UKq is universal kriging with a quadratic model. SubUK is subdivided universal kriging with a linear model.

of searching radius is arbitrary and can change the data points that contribute to the interpolated value. Fourth, the IDW method is subject to clustering.

The MinCurv method gives the second greatest variability in the experiment (Figures 15 and 21). The residuals vary from 24.3 m to -30.5 m, and the MAE and MSE are 5.7 and 61.9, respectively. The extreme values of the residuals have similar distribution patterns as the IDW method but are less variable. One of the three minutes in diameter, high positive residuals observed in the IDW method in the northeast of the canyon has disappeared. Unlike most of the interpolation methods, this method is a global interpolator which uses all known points in the study area to infer the unknowns. The MinCurv method flexes a thin plate and attempts to fit the known points. Since the tension of the fitting function is adjustable, the thin plate can become a membrane that drapes and conforms with the known values. As a result, the interpolated result is eye pleasing and is good for contouring. However, in the case of bathymetric studies, the seafloor is disrupted by faults and channels which makes the estimates prone to errors. Besides, the method used to divide the surface into patches for fitting the bicubic splines is not unique and can be troublesome.

The distribution of the residuals for the TIN method is very similar to the MinCurv method but is less variable (Figure 16). The residuals of the TIN method have a maximum value of 20.3 m and a minimum value of -28.6 m. The MAE is 5.6, and MSE is 59.1 (Figure 21). The TIN method considers the irregular distribution of known points by connecting them to triangles. If the desired interpolation points have varied densities or are from different sources, this approach can conserve computer storage disk space by varying resolutions according to the density of the data. In this study, although the density of depths derived from Sea Beam data is a function of water depth, the variation is not significant (less than 60 m). Although the TIN method is very useful during data collection when morphologic relief is known, the interpolation results based on the TIN

method are at a disadvantage compared with the IDW method where estimated values are influenced by their adjacent known values. The TIN method is also usually not used for extrapolation. Because of triangulation, the interpolated results from TIN method can be jagged. Another disadvantage of using TIN method is that for visualization purpose, the resultant irregular grids are usually converted to a regular grid for final viewing.

The OK method shows similar residual distributions as IDW method but with less variations, and less high negative residuals in the northeast portion of the canyon (Figure 17). The extent of the residuals is the second largest among the methods tested, with a maximum of 26.4 m and a minimum of -29 m. The MAE and MSE is the second or the third largest with values of 5.8 and 61.1, respectively. All the UK methods show similar residual distributions as TIN method. The extreme residuals of UKI and UKq are comparable, with UKI values between 18.53 m and -25.3 m, and UKq values between 19.3 m and -23.6 m. The maximum and the minimum residuals of SubUK are 17.1 m and -24.7 m and are the least among the seven tested methods. For the UK methods, from the largest to the least MAE/MSE values are: UKq (5.3/52.0), UKI (5.0/44.7), SubUK (4.9/42.1).

Overall, the geostatistical or kriging methods all perform better than the IDW method, and the UK methods perform better than the MinCurv and TIN methods. That spatial distribution of the OK's residual is analogous to the IDW's can be explained by the fact that both are weighting algorithms. However, in the IDW method, the choice of the search window size and the weighting function are arbitrary. For a larger searching radius, the long-range variation will be emphasized, while the short-range variation will be neglected. In kriging, both the size of the window and the weighting function are determined statistically. That the OK method has residuals that are larger than the MinCurv and TIN methods suggests that kriging does not always give better estimates. For the UK, which considers the drift of the interpolation points, the residuals are smaller

than other methods. The UK with linear model also shows better estimates than the quadratic model indicating that a complex model does not necessarily improve the prediction. However, because the subdivided area satisfies the property of homogeneity, the UK with 9 km<sup>2</sup> subdivisions gives the least variation among all methods experimented.

Kriging can also tell the uncertainties associated with the interpolated results, estimate the error of confidence, and tell which areas need more samples. Since the weight is determined not only from the distance of observation and estimation points, but also in between observation points, kriging can decluster oversampled areas. However, kriging is time consuming, and it may generate anomalous lows and highs.

Other observations from the residuals include: The statistics show that all the estimates are within  $\pm 36$  m of the true values and have fairly symmetrical distributions. All the means, except OK, show negative values which means they tend to underestimate the true value. Except for the SubUK, the greatest variability occurred in the northeast portions of the canyon for all the methods examined. Another area showing large variability is the central west part of the canyon. The greater uncertainty in these two areas can be explained by the short wavelength features or rough relief.

Instead of only looking at the difference in 233 randomly selected locations, the variations of gridded results for different algorithms are examined. Although the SubUK gives the least MAE and MSE, the sample numbers in a search window sometimes fall below the required number for variogram evaluation and thus give voids in the interpolated grid. As a result, the UKI is chosen as a reference to compare the difference with other algorithms. Table 2 shows the statistics of the difference between an individual algorithm and the UKI results. Figures 23 to 28 show the difference in gray scales with lighter tones representing positive differences and darker tones representing negative differences.

Table 2. Statistics of interpolated difference with respect to UKI method

	IDW	MinCurv	TIN	OK	UKq	SubUK
Min. (m)	-225.678	-188.378	-364.795	-165.499	$-5.1 \times 10^{12}$	-195.457
Max. (m)	242.562	202.149	615.509	168.226	$1.4 \times 10^{13}$	181.000
Mean (m)	-0.143	-0.505	-0.011	-0.238	$2.7 \times 10^7$	0.076
$\sigma^*$ (m)	19.143	11.470	9.512	8.723	$2.4 \times 10^{10}$	5.282

\*standard deviation

Generally speaking, the greatest variations occur in the boundary regions of the Sea Beam coverage. The next greatest variations are located in areas with rougher surfaces, such as in the northeast portions of the canyon and along the canyon wall. The areas along ship tracks also show large variations. If the impossible values for UKq are excluded, the IDW and UKI interpolated results have the greatest difference with a standard deviation of 19 m (Figure 23). Besides the boundary of the Sea Beam coverage, the main differences occur in the northeast portions of the canyon, west of the canyon, in the main drainage path, and along the ship tracks. The prominent differences along the ship tracks suggest the IDW method is sensitive to Sea Beam's nadir noise.

For the MinCurv method, the differences along the ship tracks are generally negligible, except a few streaks in the northern half of the canyon (Figure 24). These differences are errors acquired during data collection, and the UKI interpolated results in these areas might not be correct. The other major differences occur in the short-wavelength features like the canyon wall, especially in the main drainage path that aligns from the northeast to southwest of the canyon.

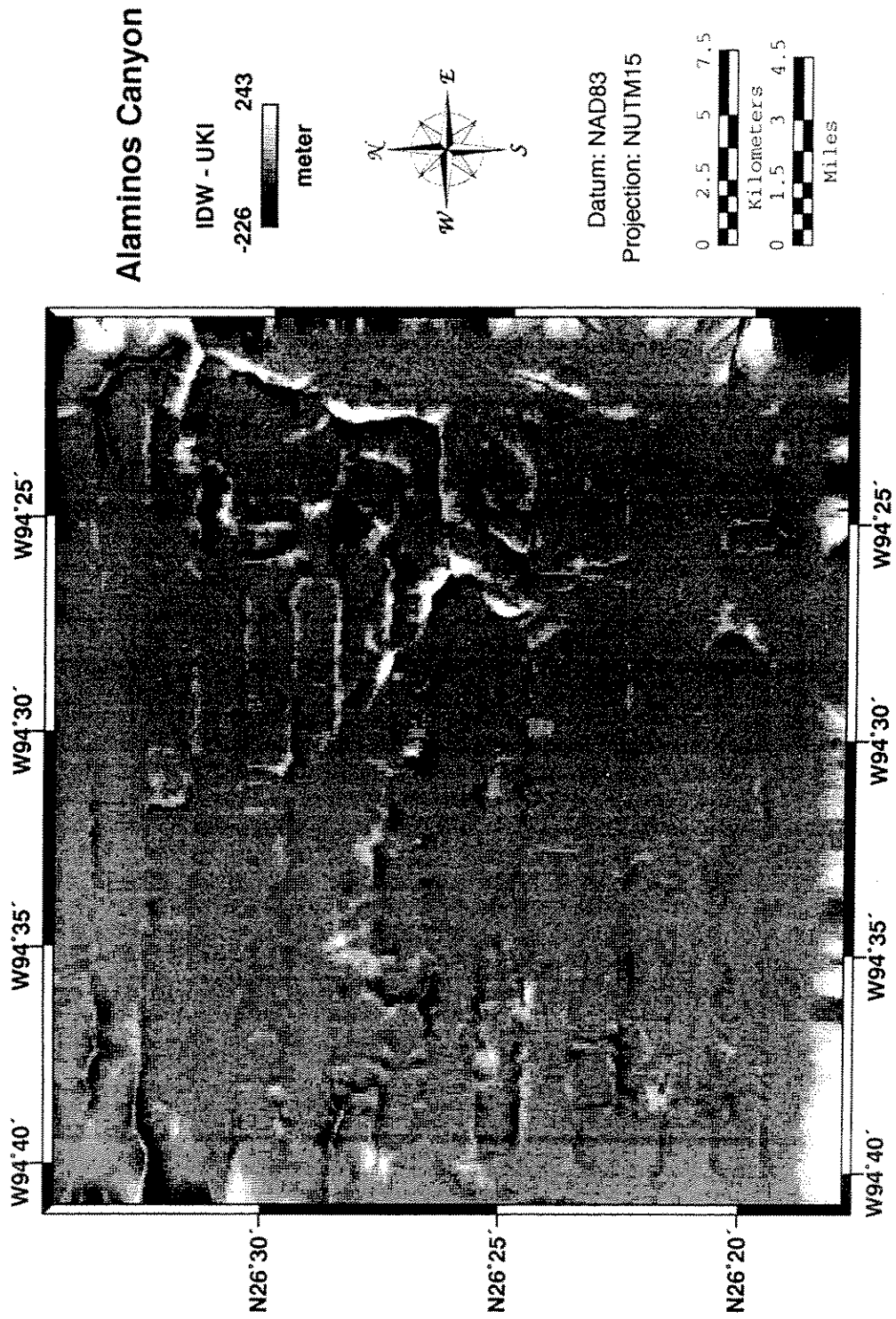


Figure 23-Depth difference between IDW and UKI methods.

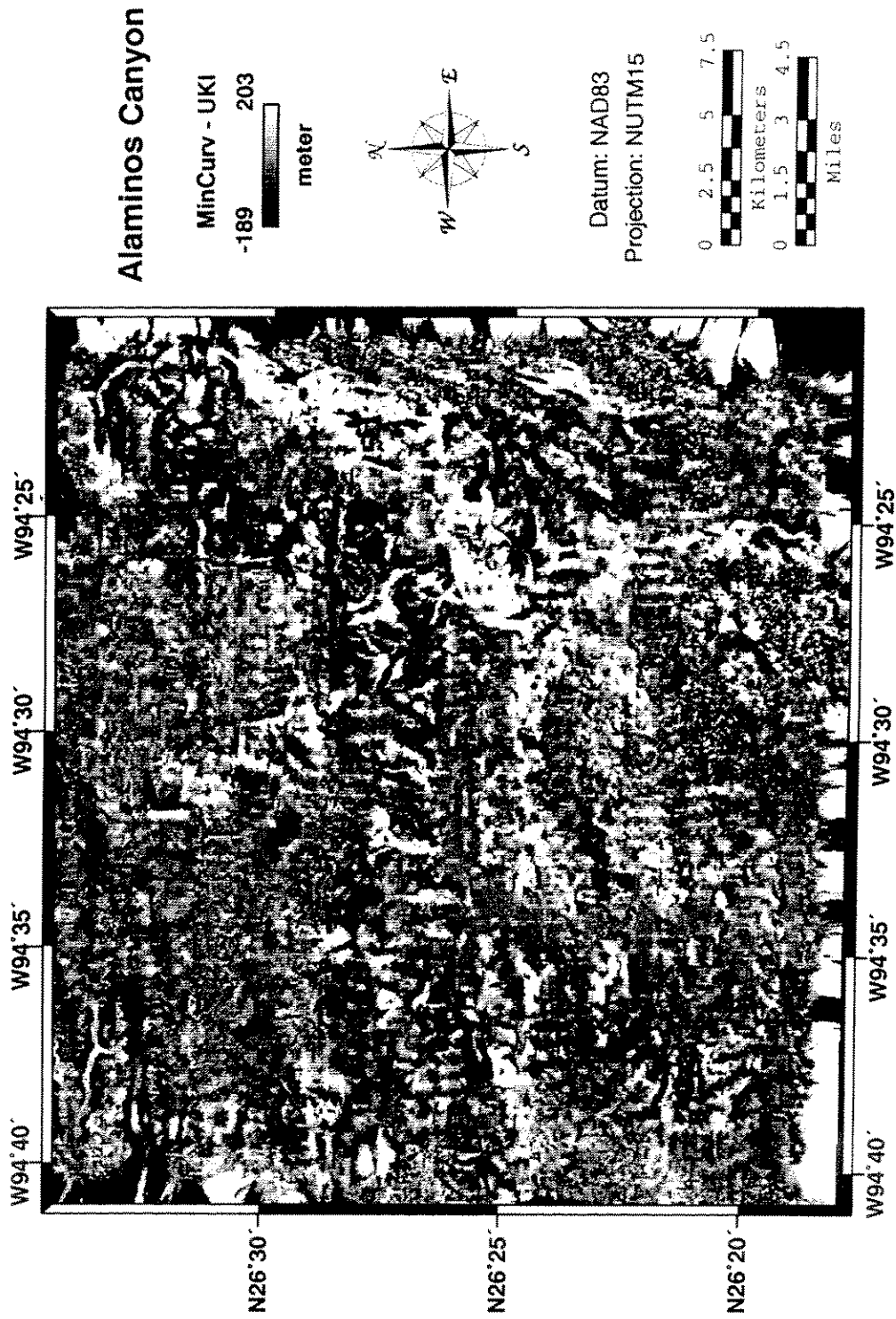


Figure 24-Depth difference between MinCurv and UKI methods.



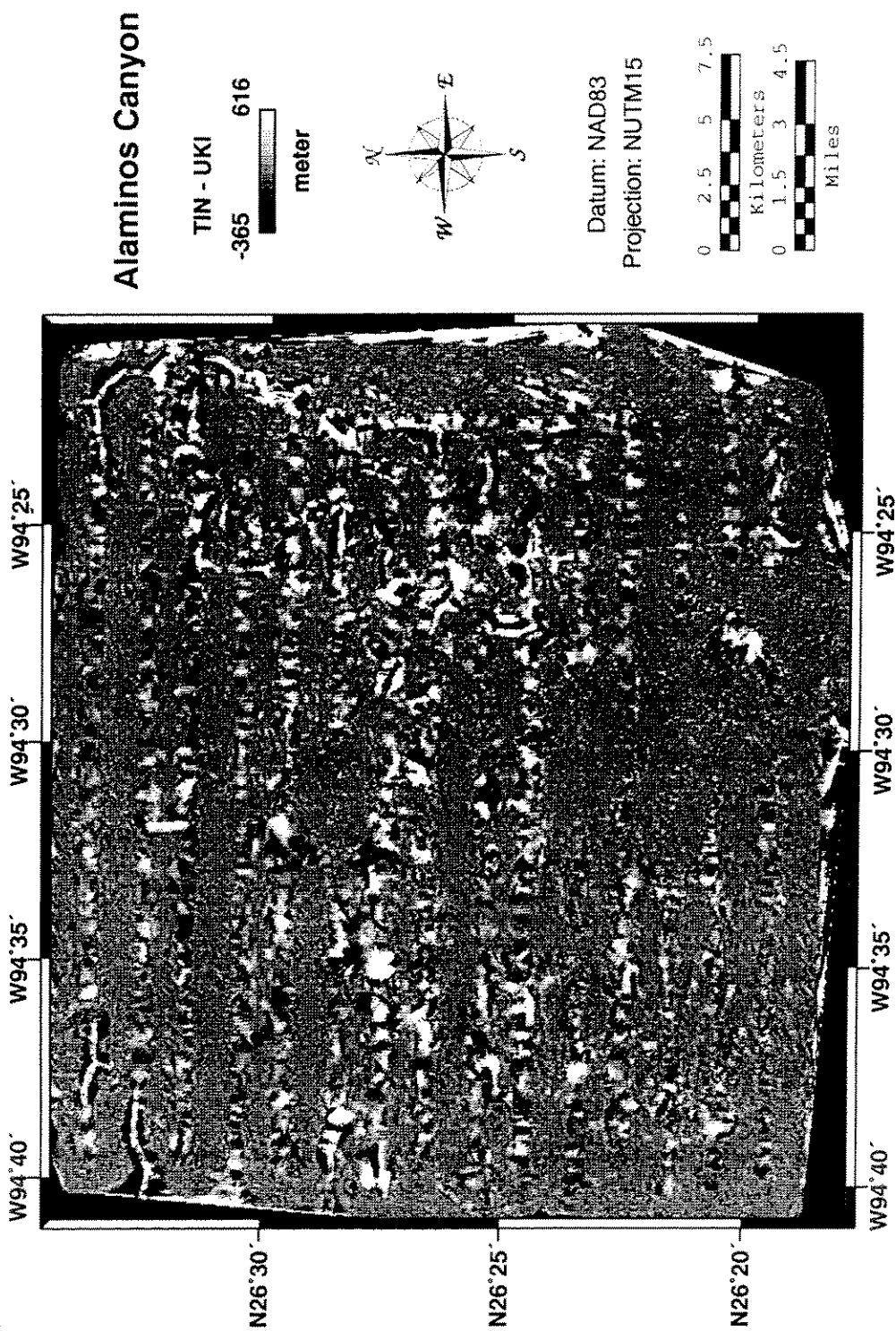


Figure 25-Depth difference between TIN and UKI methods.

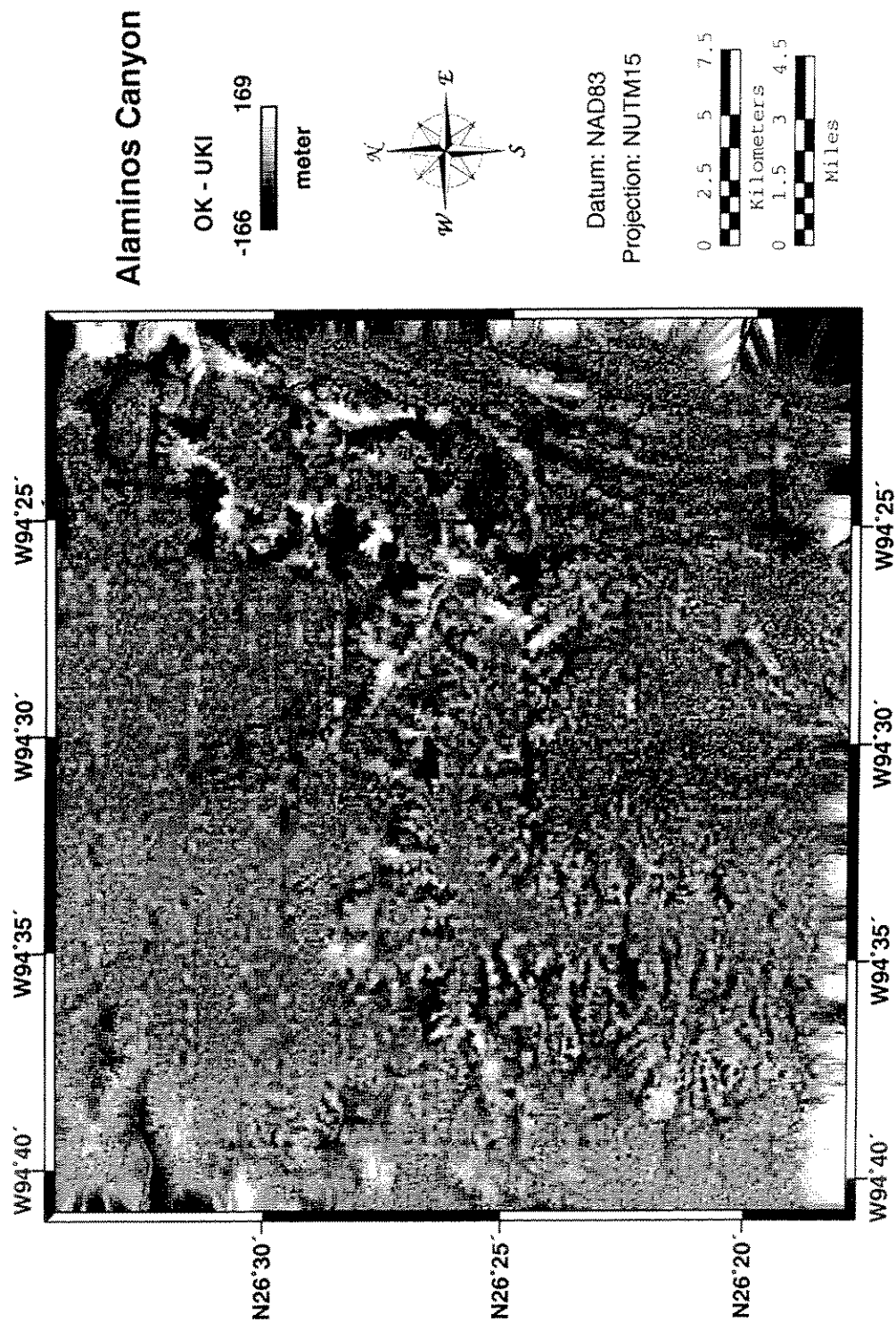


Figure 26-Depth difference between OK and UKI methods.

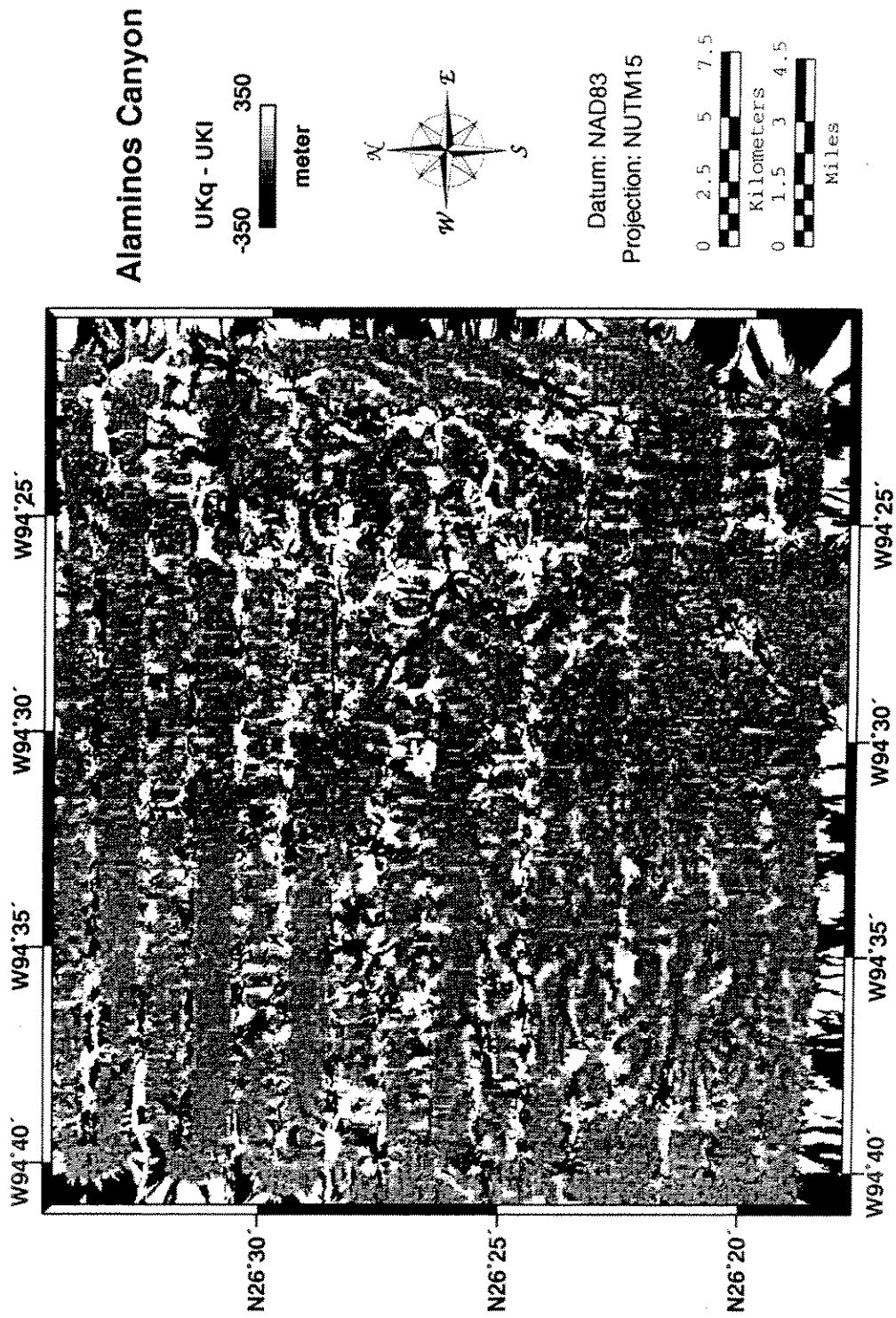


Figure 27-Depth difference between UKq and UKl methods.

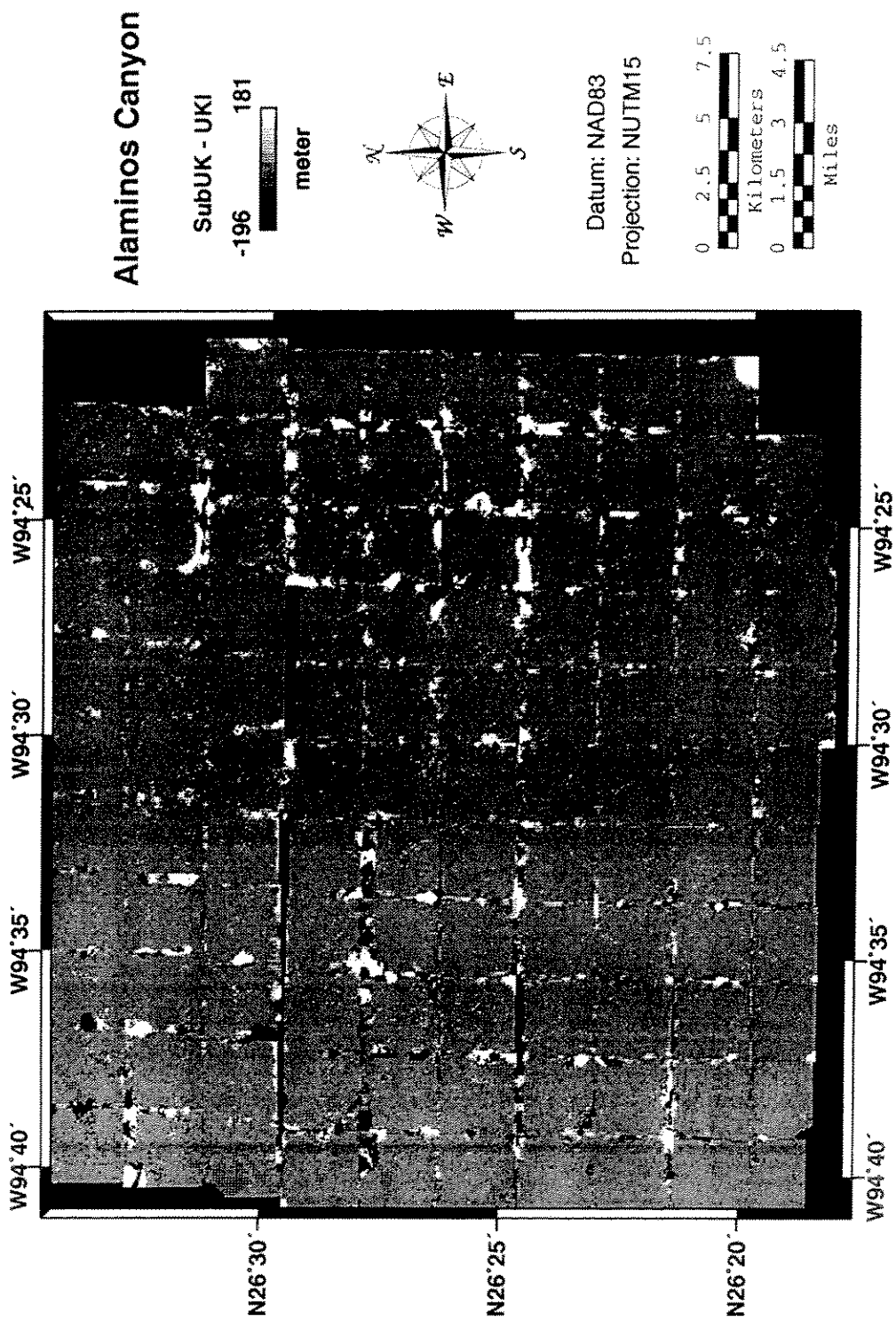


Figure 28-Depth difference between SubUK and UKI methods.

Because of the triangulation of the irregular points, the TIN method does not show much variation near the boundary of the Sea Beam coverage (Figure 25). The standard deviation is 9.5 m. The major differences seem to combine the differences of the IDW and MinCurv methods that lie in the northeast portions of the canyon and along ship tracks.

The comparison between OK and UKI results shows that the major differences occur from NE of the canyon to the main drainage path (Figure 26). Besides the lineation caused by ship tracks, the southeast portion of the canyon also shows NNE-SSW oriented linear patterns. The standard deviation is 8.7 m which is less than the IDW, MinCurv, and TIN methods. That the difference between UKq and UKI results reaches unreasonable numbers is attributed to the anomalous spikes and pits sometimes generated by kriging. By limiting the difference to -300 m and 300 m, the mean comes to 0.402 m, and the standard deviation is 29.1 m. The major difference occurred in the northern half of the canyon (Figure 27) indicating that the linear and quadratic models yield similar results in the southern side of the canyon. Comparing with UKI, SubUK has the least variation (standard deviation = 5.3 m) but has many voids (Figure 28). These voids occurred in the boundary of the Sea Beam coverage and along some ship tracks where not enough data points are available for interpolation. The differences between UKI and SubUK results are mainly along the boundaries of the subdivisions suggesting that the major difference between these two methods are the processing of the boundary values.

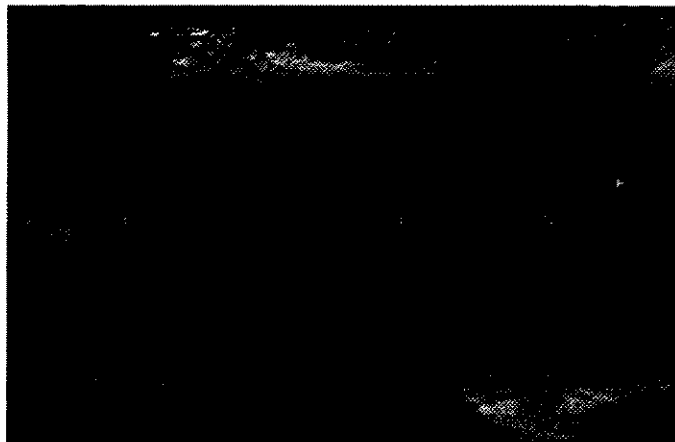
In summary, based on the same Sea Beam data in the study area, different interpolation algorithms do generate different results. The difference can be negligible when the seafloor is relatively low relief compared to the interpolated spacing. In the canyon wall and channel path, the difference of the estimates can be more than 35 m. According to NOAA (1992), the positional accuracy of a sounding is within 50 m of its true location, and the error in depth is less than 1% of the true water depth. In the study

area, the depth inaccuracy caused by the machine is less than 25 m. To limit further generation of the error, an optimum interpolation is desired. In fact, a proper interpolation method is more important in the study area than the depth correction using Carter's Table, as the adjustment based on the Carter's Table varies only from -5 m to -2 m in the area. With the density of the data and the size of the canyon, UKI seems to be able to generate a surface closest to reality, although occasionally errors acquired during surveys are included in the interpolation.

### **GLORIA II sidescan sonar image**

Because thermocline reflects the low-incident angle sound waves, the GLORIA II sonograph usually lacks non-zero DNs in the far range. Figure 29(a) is the plane view of a GLORIA II sonograph with a major portion of the far range being removed. The ship is traveling from west to east in the example. In this image, the lighter shades occur in the far range and in the nadir. Adjacent to the light shaded nadir are speckled lower DNs (darker). Two methods were used in correcting the nadir and near range noise within the columns of nadir  $\pm 70$  pixels. The first method uses normalization of DN values across the ship track. The result is shown in Figure 29(b) in which the nadir light color has darkened, but the scattered darker DNs along the nadir do not show improvement. The second method uses histogram matching. The result is shown in Figure 29(c). Although some of the DNs in the nadir become higher or brighter, the number of messy dark pixels in the near range has decreased.

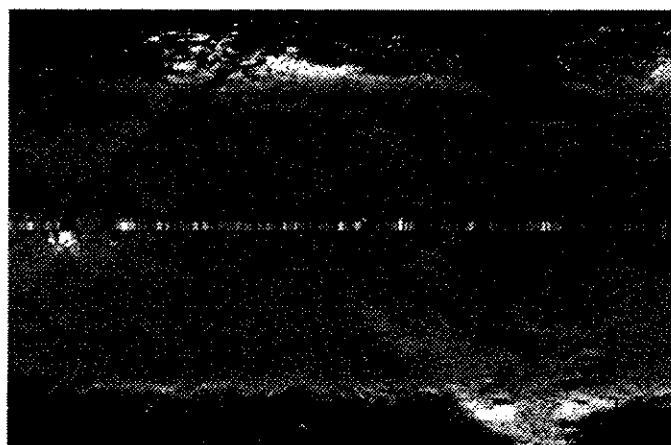
Figure 30 shows profiles of averaged columns for the nadir  $\pm 70$  pixels. Figure 30(a) shows that in the original image the DN "crests" in the nadir can exceed 40. Adjacent to the "crests" are the "troughs" with minimum DN values of 24. Next to the "troughs" are DN "bumps" then DN values stabilize to about 33. In the profile of the



(a) Original sonar image.

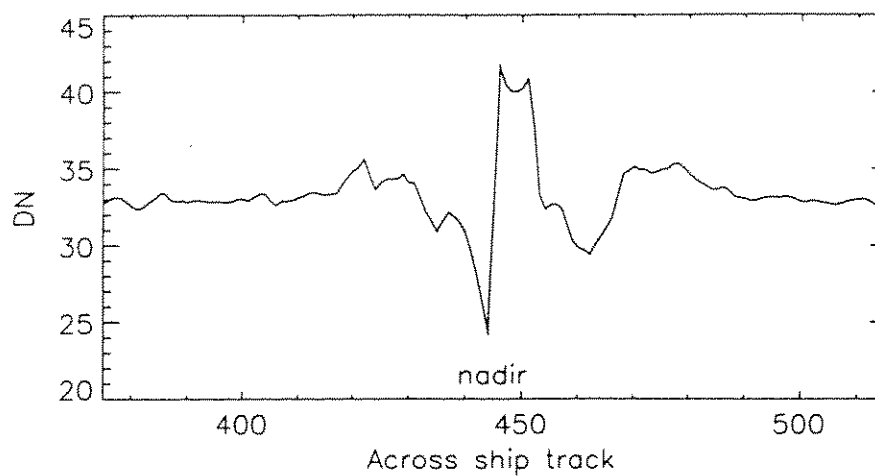


(b) Normalized sonar image.

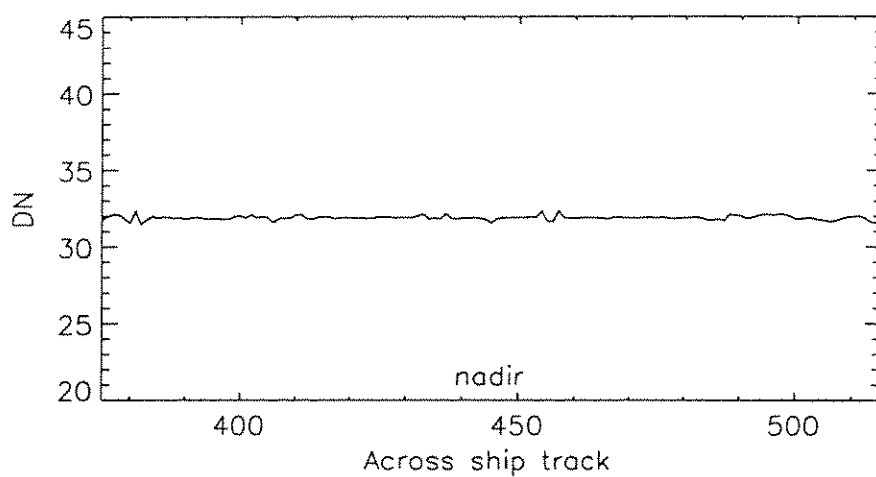


(c) Histogram-matched sonar image.

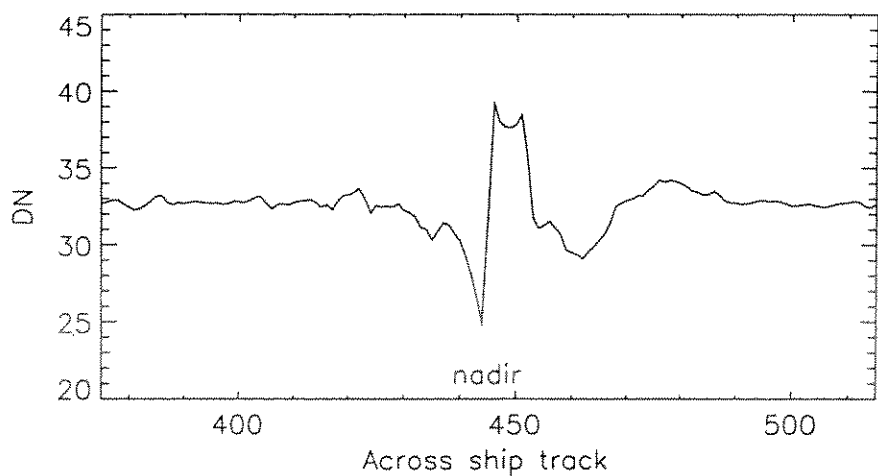
Figure 29-Example of a GLORIA II image strip.



(a) Original profile of a sonar image.



(b) Normalized profile of a sonar image.



(c) Histogram-matched profile of a sonar image.

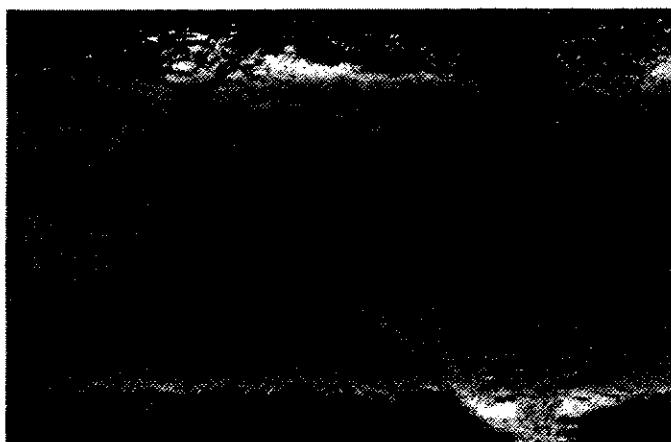
Figure 30-Averaged along ship track DN profiles of a GLORIA II image.



normalized method, the DN averages stay the same at about 32 indicating the effectiveness of the normalization (Figure 30(b)). However, as indicated in Figure 29(b), the resulted image is not satisfying. This might be explained by noting that the light toned nadir and dark toned “troughs” in the near range should not be the focus in the image processing. The focus should be on the “bumps” next to the “troughs” which are not prominent in the image strip. The histogram-matched method adjusts the near nadir DNs to levels comparative to their surroundings. As a result, the averaged columns show a similar distribution as the original image but have a decreased amplitude of the DNs (Figure 30(c)). The decreased amplitudes also make the “bumps” less visible and contain a decreased portion of the noise in the resulting image.

Based on the histogram matched image, the filtering criteria mentioned in Chapter III are applied to reject the uncorrectable messy DNs in the nadir and near range. Figure 31(a) shows the results if the DNs of the rejected pixels are replaced with 0's or voids. Figure 31(b) is the result of using spline interpolation in the across-ship-track direction to fill the voids. In this method, the interpolated values follow a spline function but make the interpolated image unsatisfying. Figure 31(c) shows the result if the voids are filled with randomly sampled DNs. The resultant image shows that the newly replaced DNs can blend with the rest of the image well. However, for both methods, locally the dark colored pixels still speckle in the near range, indicating the filtering of messy DNs is not one hundred percent successful.

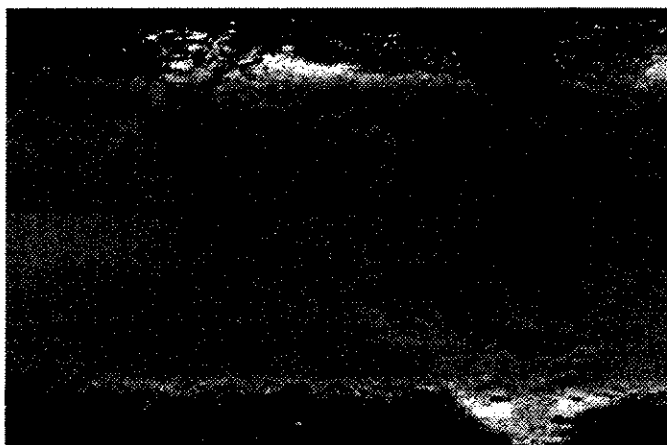
The same procedure is repeated for the rest of the image strips in the study area. The DNs are georeferenced according to the ship's position using the same georeferencing method as for the multibeam data. Unlike the traditional sonar image mosaic where aspect-ratio distortions are compensated by repetitive pings, the unknown values are interpolated using the MinCurv method. The processed image is then passed



(a) Histogram-matched sonar image with voids



(b) Interpolated sonar image



(c) Random points filled sonar image

Figure 31-The same GLORIA II image strip as Figure 29.

with a 5 by 5 median filter to constrain the noise. The DNs of the final GLORIA II image are then linearly stretched to 0-255 to highlight the variation (Figure 32).

In the reprocessed GLORIA II image, most of the artifacts shown in the extracted GLORIA II image have either disappeared or lessened. Some dubious pixels in the extracted image turn out to be artifacts which may have been introduced during mosaic generation. The reprocessed image also shows that the study area is mainly featureless except in the northeast and inside the canyon.

Besides visually examining the quality of reprocessed images, one way of checking the effectiveness of removing noise is to use signal-to-noise ratio (SNR) (Jain, 1989):

$$SNR = 10 \log \frac{\sigma_o^2}{\sigma_n^2} \quad (16)$$

where  $\sigma_o^2$  is the variance of the original image, and  $\sigma_n^2$  is the variance of the difference of the original and processed images.

As the individual sidescan sonar strip has many 0 values in the far range, the SNR is calculated with the whole image strip and with the area that has no 0 values. Table 3 shows the SNR of a processed sidescan sonar strip.

One assumption of using the SNR is that the removed or changed DNs are noise, such that if there are no DNs altered after the processing, the SNR will reach infinity. In this study, the SNR is more like an indication of the closeness of processed image to its original image. According to Table 3, the histogram-matched and random points methods show better resemblance to the original image. From visual inspection, the random points is the best method among all methods examined.

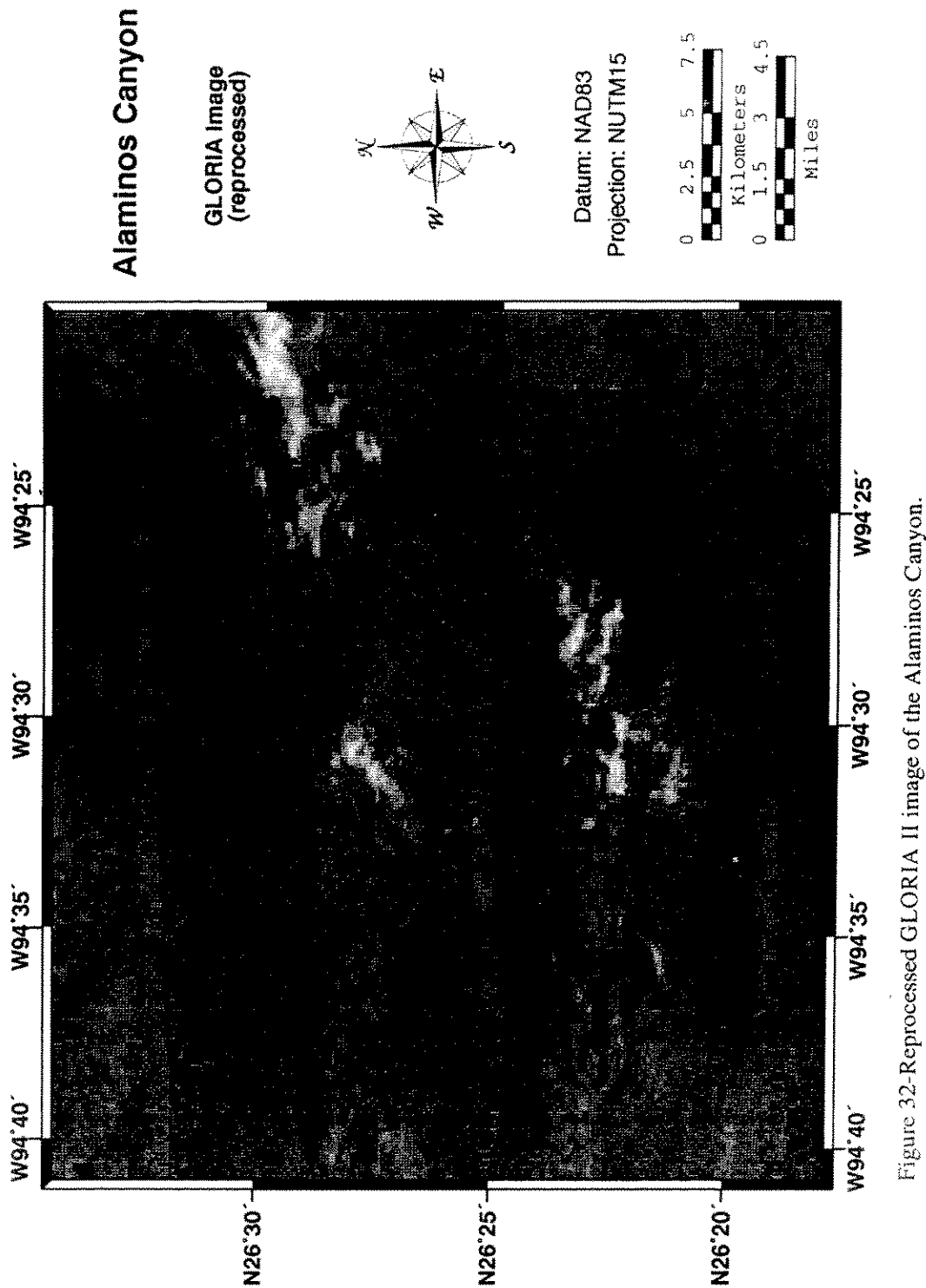


Figure 32-Reprocessed GLORIA II image of the Alaminos Canyon.

Table 3. Signal-to-noise ratio (SNR) of processed GLORIA II image

Methods	Whole Image	None-zero Coverage
Normalization	-37.21 dB	-40.01 dB
Histogram-matched	-13.90 dB	-28.18 dB
Interpolated	-16.24 dB	-30.28 dB
Random points	-13.99 dB	-28.21 dB

For the whole processed image, the SNR is -9.87 dB, which is much larger than the individual sonograph. However, the comparison is not appropriate, as visually a major portion of the higher DNs have changed their spatial locations. This is because during the georeferencing, the five ping averaged heading is used to project the locations of the fish and its corresponding footprints to geographic coordinates. The NGDC released image uses a straight heading (although it was said that the heading was adjusted every 30 minutes; EEZ-Scan 85 Scientific Staff, 1987). The reprocessed sonograph is also fuzzier than the one released by NGDC. This is because during the adjustment of the anamorphic-ratio distortion, the NGDC-released sonograph uses duplicate scan lines along the ship track direction, while the reprocessed sonograph uses MinCurv to fill the gap.

In summary, after reprocessing of the GLORIA II image, the messy nadir zone and near nadir areas are significantly compressed. The dubious variations of DNs are cleared, and the location of sidescan footprints is more closely georeferenced. In the reprocessed image, only the northeast, central east, and a small patch in the central west portions of the study area display intriguing variations. That the interpolated DNs that fill the void after rejecting the erratic DNs are not satisfying may be explained by the fact

that the backscattered image does not follow a mathematical function. Using radius limited random DN values to fill the void seems to be more natural and eye-pleasing.

### **Ground truth samples**

The four piston cores taken in the Alaminos Canyon in 1996 have lengths ranging from 780 cm to 849 cm. The depth profiles of P-wave velocity and corrected bulk density are shown in Figures 33-36. The velocities of AC01 are lower than 1,490 m/sec and slightly decrease downward. The velocities of AC02 are also less than 1,490 m/sec, except in the depths below 640 cm, where a few scattered measurements reach above 1,500 m/sec. AC03 has the greatest velocity variation. The velocity reaches 1,530 m/sec at 10 cm depth then drops to 1,484 m/sec between 90 cm and 170 cm. It increases to 1,520 m/sec at the depth of 240 cm then drops to 1,481 m/sec at 390 cm. It then gradually increases to near 1,530 m/sec downcore. The velocity of AC05 is less variable compared to AC03 with an averaged velocity of about 1,485 m/sec then increases to 1,508 m/sec downcore.

The densities of AC01-AC05 vary from 1.3 g/cm<sup>3</sup> to 1.86 g/cm<sup>3</sup>. AC01 has a density of about 1.34 g/cm<sup>3</sup> near the seafloor. It increases to 1.46 g/cm<sup>3</sup> at 150 cm then drops to 1.36 g/cm<sup>3</sup> at 250 cm. It then increases, but with fluctuations, downcore. The density variation of AC02 exhibits a similar trend to that of AC01 but in a different depth scale. The density distribution of AC03 fluctuates above 320 cm, then increases abruptly from 1.55 g/cm<sup>3</sup> to 1.86 g/cm<sup>3</sup> downcore. At depths shallower than 170 cm, the densities of AC05 do not vary much and average about 1.43 g/cm<sup>3</sup>. The density increases to 1.52 g/cm<sup>3</sup> at about 200 cm and remains near that value to 300 cm. It decreases to about 1.5 g/cm<sup>3</sup> for depth between 300 cm and 500 cm. It then increases steadily to 1.72 g/cm<sup>3</sup> at 800 cm.

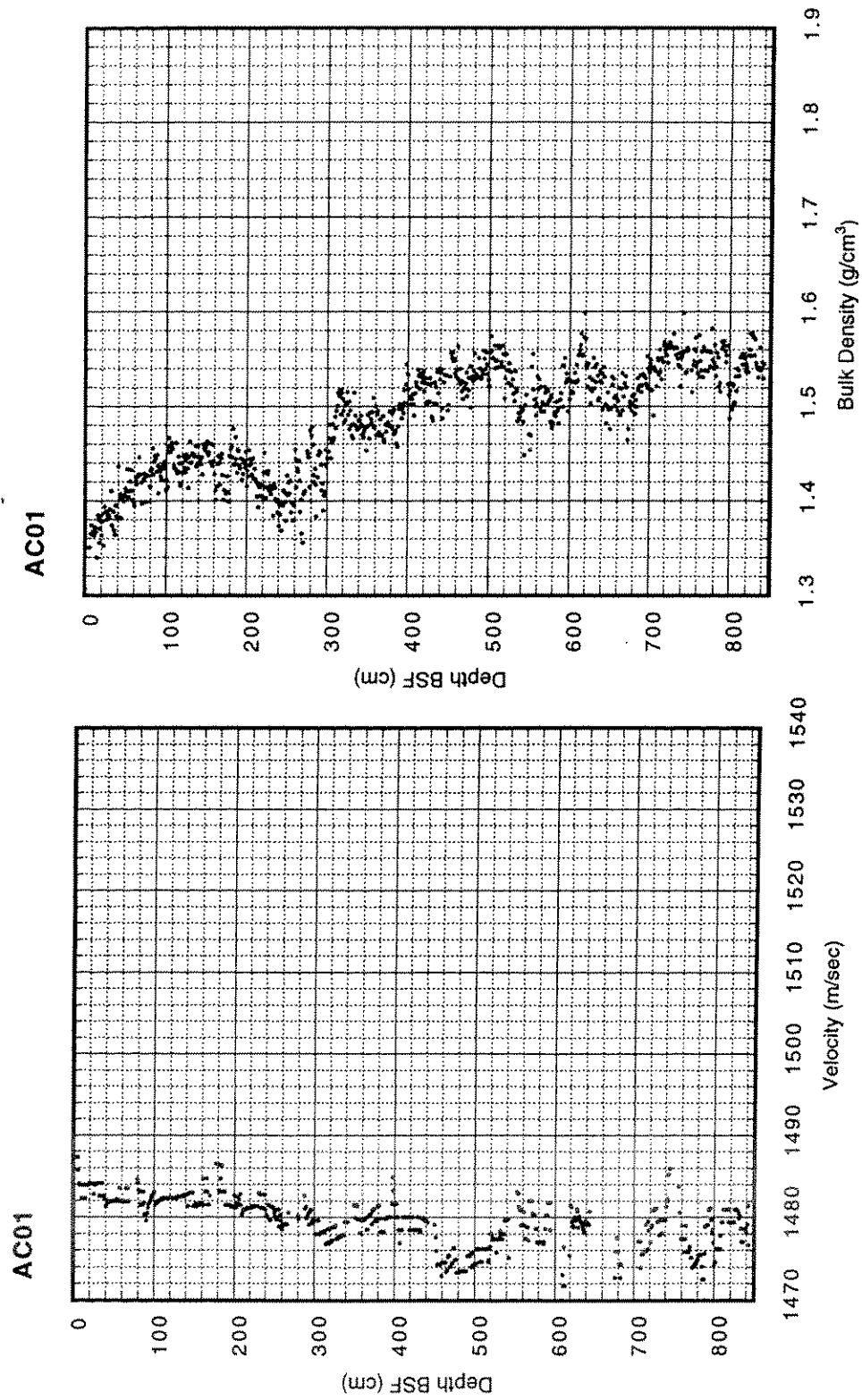


Figure 33-P-wave velocity and bulk-density plots of AC01.

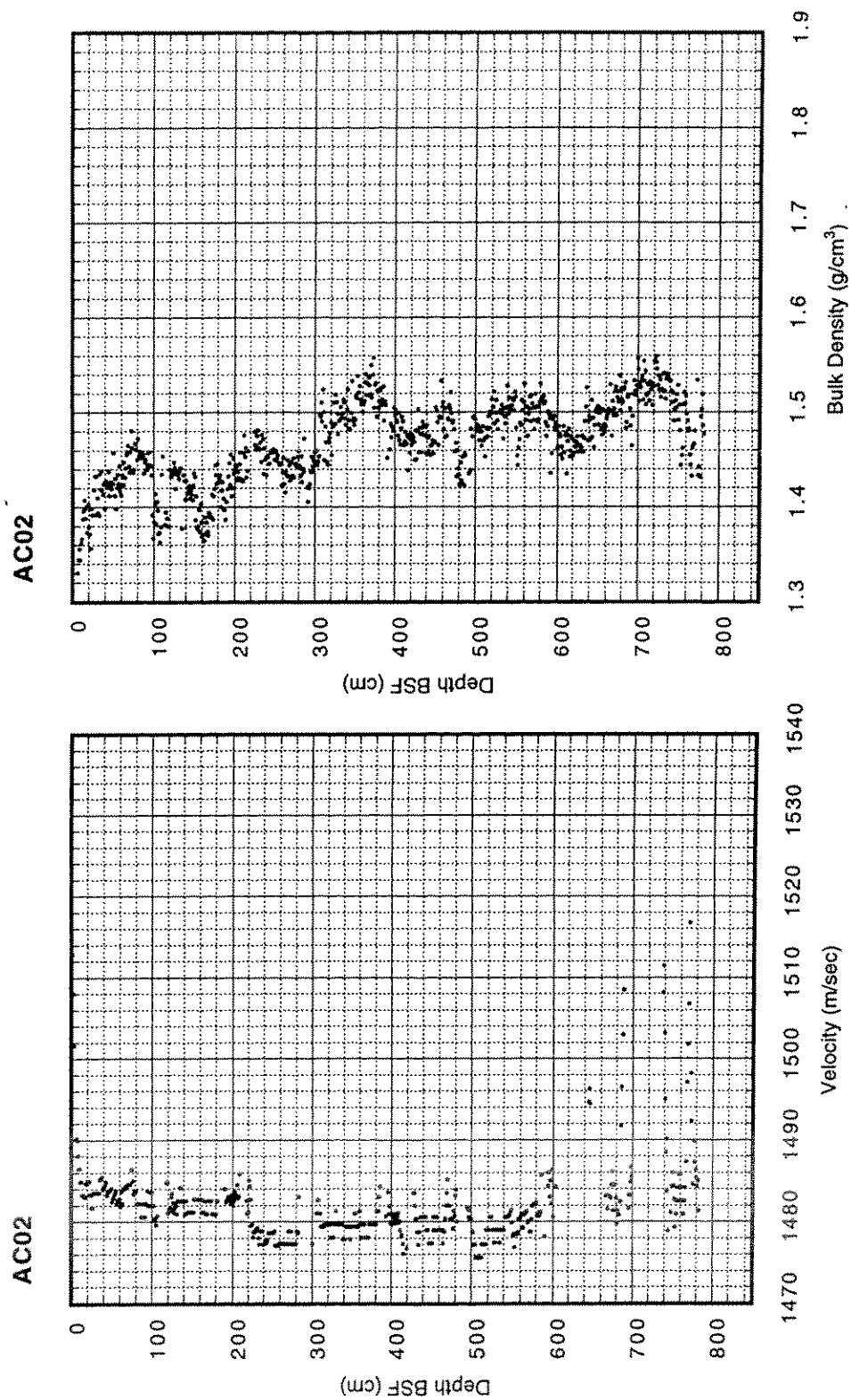


Figure 34-P-wave velocity and bulk-density plots of AC02.



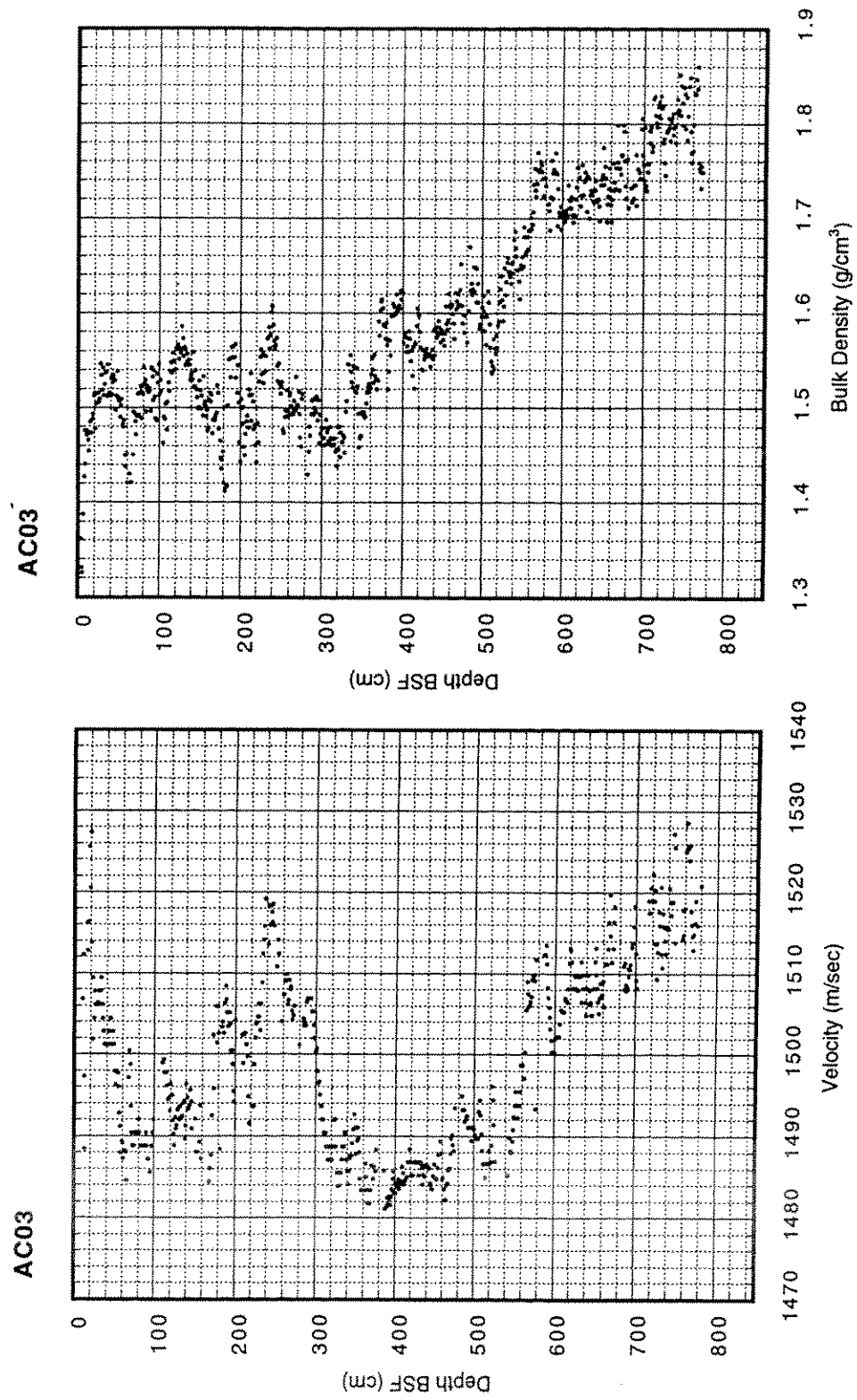


Figure 35-P-wave velocity and bulk-density plots of AC03.

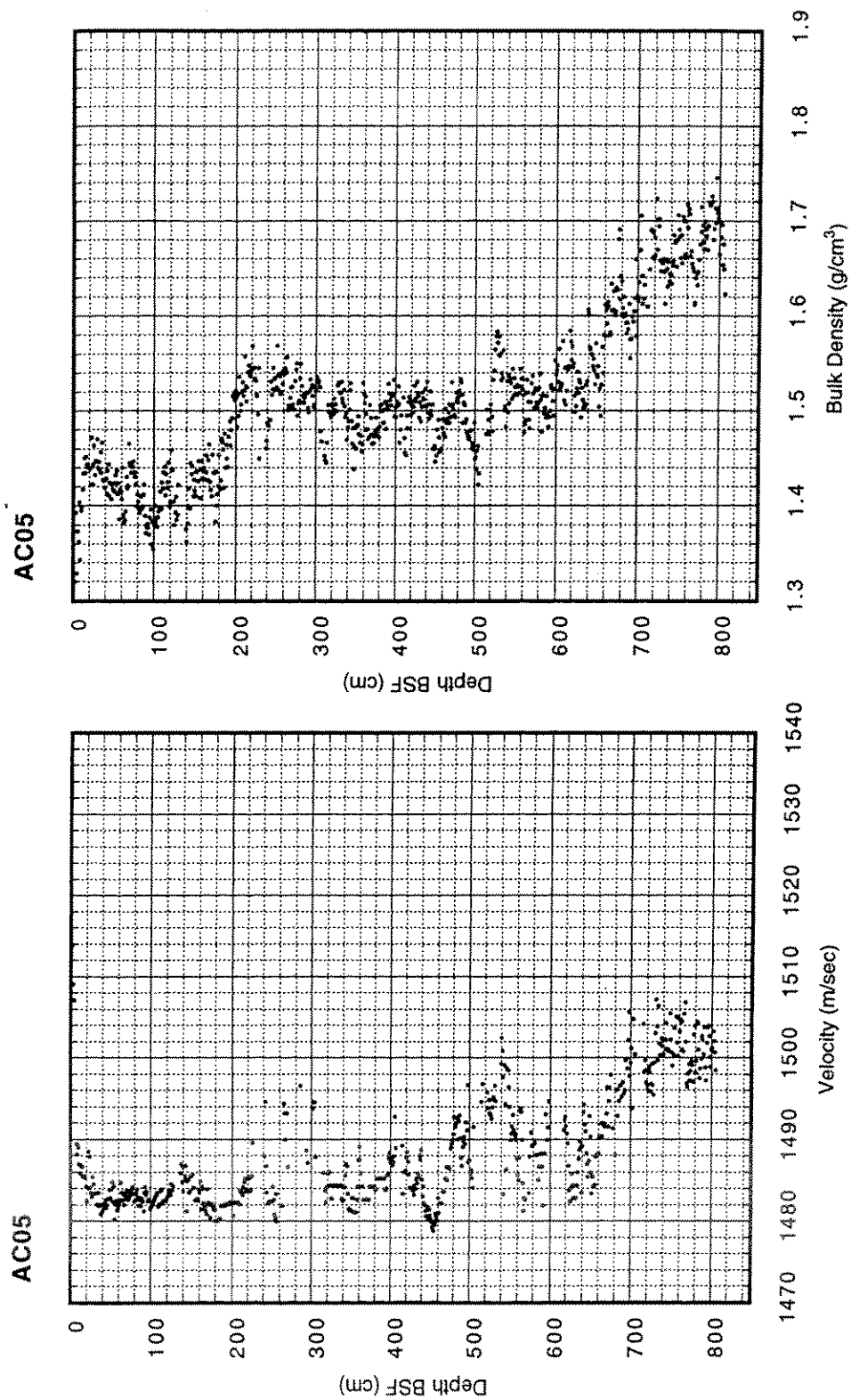


Figure 36-P-wave velocity and bulk-density plots of AC05.

### Sediment accumulation rate

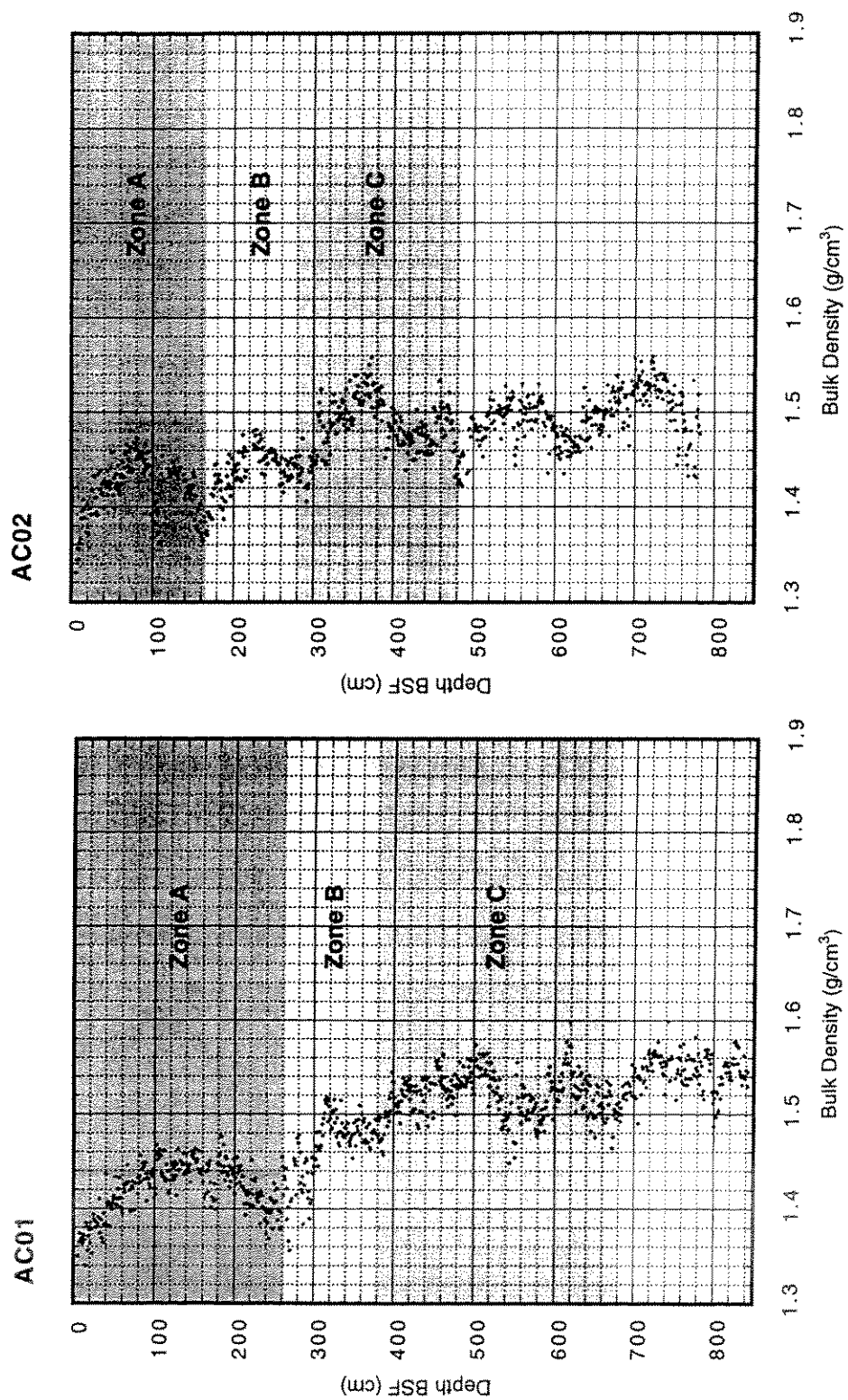
Ground truth samples, AC01 and AC02 are about 8 km apart and located inside the canyon near the main drainage path. A correlation based on the fluctuations of bulk density of these two cores is illustrated in Figure 37. Three time zones, Zone A, B, and C, are assigned. For AC01, Zone A extends from 0 to 264 cm, Zone B extends from 264 cm to 378 cm, and Zone C extends from 378 cm to 678 cm. For AC02, Zone A extends from 0 to 164 cm, Zone B extends from 164 to 280 cm, and Zone C extends from 280 to 482 cm. The ratios of sedimentation rate, defined as sediment thickness per unit time, of AC01 versus AC02 for Zones A, B, C are 1.6:1, 1:1, and 1.5:1, respectively. To compare the different sites objectively, compaction owing to overburden pressure needs to be compensated. The converted ratio is called accumulation rate and is defined as the mass of sediment deposited during a certain time period (Koczy, 1951):

$$\alpha = \omega \cdot \rho_d \quad (17)$$

where  $\alpha$  is accumulation rate in  $\text{g/cm}^2 \cdot 10^3\text{yr.}$ ,  $\omega$  is sedimentation rate in  $\text{cm}/10^3\text{yr.}$ , and  $\rho_d$  is dry-bulk density in  $\text{g/cm}^3$ . The dry-bulk density can be calculated from the wet-bulk density, and fractional porosity:

$$\rho_d = \rho_b - \rho_w \phi \quad (18)$$

$$\phi = \frac{\rho_g - \rho_b}{\rho_g - \rho_w} \quad (19)$$



where  $\rho_b$  is wet-bulk density,  $\rho_w$  is sea water density (assumed  $1.024 \text{ g/cm}^3$ ),  $\phi$  is porosity, and  $\rho_g$  is grain density (assumed  $2.67 \text{ g/cm}^3$ ). Table 4 is the averaged dry-bulk density for these three time zones. The calculated ratios of accumulation rate for AC01 versus AC02 are 1.7:1, 1.1:1, 1.6:1 for Zone A, B and C, respectively.

Table 4. Averaged dry-bulk density of AC01 and AC02 for Zone A, B, and C

	AC01*	AC02*
	logger / +15% / -15%**	logger / +15% / -15%**
Zone A	0.65 / 0.78 / 0.51	0.62 / 0.77 / 0.51
Zone B	0.71 / 0.87 / 0.51	0.66 / 0.81 / 0.51
Zone C	0.80 / 0.95 / 0.51	0.73 / 0.90 / 0.51

\*Units:  $\text{g/cm}^3$

\*\*"logger" means measurements from the multi-sensor core logger; " $\pm 15\%$ " means when the wet-bulk density is  $\pm 15\%$  of the core logger measured density.

AC03 has an averaged density of  $1.5 \text{ g/cm}^3$  and above which is the greatest density among all the samples. The fluctuating density above about 330 cm is consistent with the velocity variation. The density then steadily increases up to  $1.88 \text{ g/cm}^3$  with depth. The irregular density variation above 330 cm may suggest slumping deposits. The gradual increase in density in AC03 below depth of 520 cm is similar to the trend of AC05 in the depth below 510 cm. If the sudden density increase around 200 cm for AC05 is assumed to be the Holocene/Pleistocene boundary, with an averaged dry-bulk density of  $0.65 \text{ g/cm}^3$ , the accumulation rate during the Holocene is about  $13 \text{ g/cm}^2 \text{ } 10^3 \text{ yr}$ . This value seems to be a bit high compared to the accumulation rate observed in the Mississippi Fan area ( $1\text{-}10 \text{ g/cm}^2 \text{ } 10^3 \text{ yr}$ ; Wetzel and Kohl, 1986). This relatively high value may be explained by the inclusion of material other than hemipelagic sediment in

the calculation. For AC01 and AC02, a comparison with Deep Tow 3.5 kHz profile indicates that the recovered 800+ cm sediment may all belong to the Holocene material. In such a case, the accumulation rate exceeds  $50 \text{ g/cm}^2 \cdot 10^3 \text{ yr}$ . Again, this high rate is mainly attributed to mass wasting of sediment into the canyon.

### **Intrinsic morphologic properties**

Considering again the Sea Beam data, after determining the geographic locations of side beams, rejecting erroneous soundings, and rasterizing the surface in 50 m sized pixels; a detailed examination on the bathymetry within Alaminos Canyon is desired. Unlike the bathymetric contours which only reveal the depth variation in certain intervals, a solid surface usually can display finer features. Figure 38 is a rainbow colored seafloor relief map with sun shadings. The simulated sun is at  $43^\circ$  azimuth and  $53^\circ$  elevation. Based on the relief map, the canyon topography can be summarized. The canyon is mainly box-shaped with two re-entrants in the west of the canyon aligning in NNW-SSE and NNE-SSW directions. A third re-entrant is in the northeast, aligning in a NE-SW direction. A 100-200 m high ridge separates the third re-entrant from the main path of the canyon, which aligns from east to west then turns to the south. There are numerous gullies along the main path of the canyon. The depth difference from the canyon rim to the center of the canyon is about 600 m. A few inconspicuous NNE-SSW oriented faults are in the southeast of the canyon. This relief map also shows the erroneous depth values generated from the UKI method. These areas are along the margin of the map where there is no Sea Beam data, plus a few artifacts in the along-ship track direction which are also shown in the depth difference map using the MinCurv method (Figure 24). In the following, to help relate the re-entrants of the canyon with other observations, the NNW-SSE aligned re-entrant, the NNE-SSW aligned re-entrant, and the

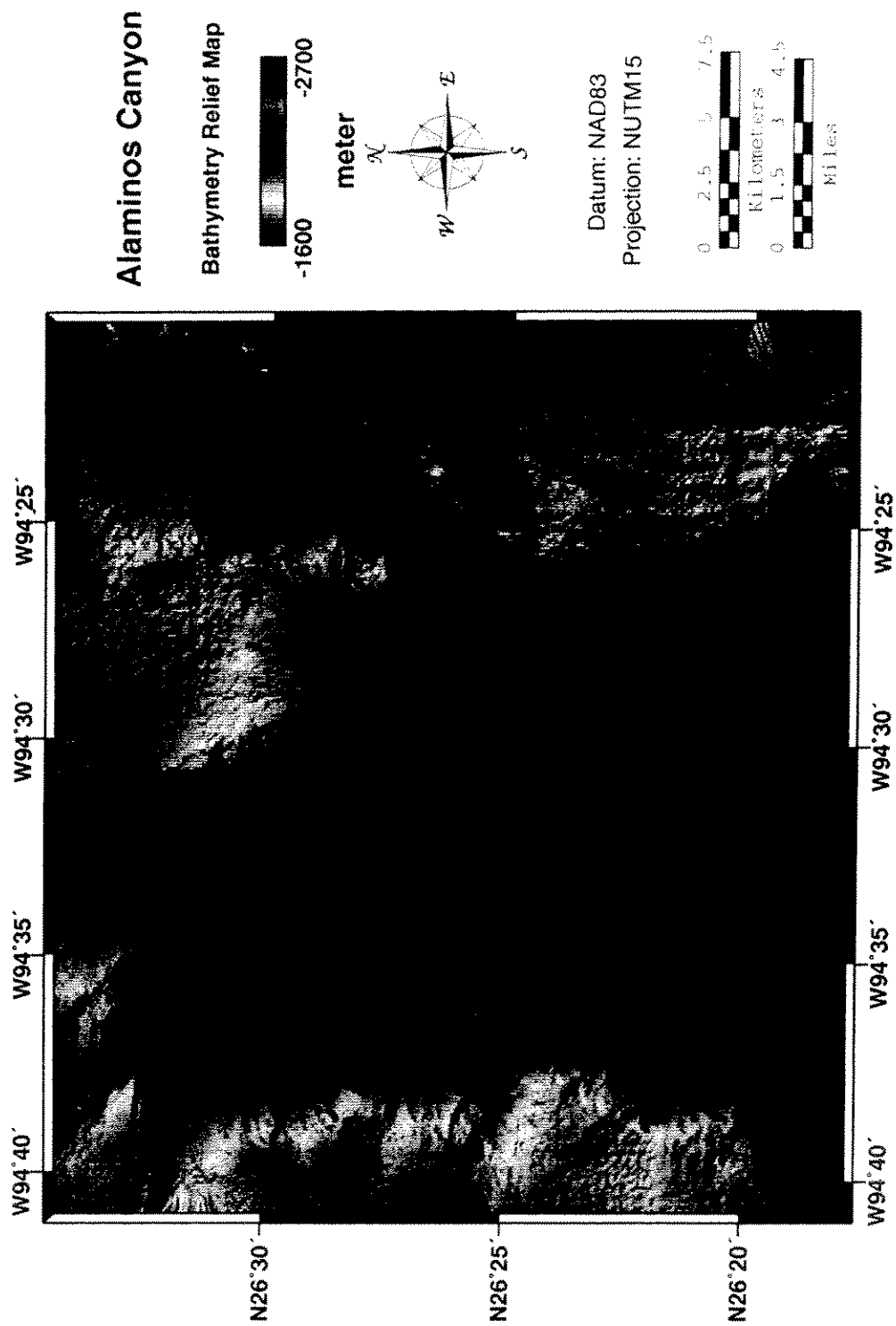


Figure 38-Bathymetric relief map of the Alaminos Canyon.

northeast re-entrant will be called Re-entrant W (west re-entrant), Re-entrant C (central re-entrant), and Re-entrant E (east re-entrant), respectively.

Based on the bathymetry, some intrinsic properties are derived. These properties include: slope gradient, seafloor roughness, slope directions, and drainage patterns. The slope gradient is determined by the vertical distance drop according to the horizontal displacement. A 150 m (3 x 3 neighborhood around each cell) shifting window is used to calculate individual cell's slope gradient in degrees. The resultant map is shown in Figure 39. The slope gradient of the canyon varies from less than 5° to more than 40° with high angled slopes along the canyon rim and in the center along the main channel path. The steepest slope, > 20°, occurred in the rim of Re-entrant E, the ridge that separates Re-entrant E to the main channel, and the central southwest rim of the canyon. Except to its east, Re-entrant C shows a moderate slope gradient of 10° and less. The NNE-SSW trending faults in the southeast of the canyon have slope gradients greater than 10°.

Seafloor roughness is calculated from the difference of the estimated depth and the mean depth of its surroundings (Figure 40). The depth difference has a mean of 0.002 m and standard deviation of 4.25 m suggesting that most of the canyon is relatively smooth. Noises along the ship tracks and the margin of the Sea Beam coverage are evident and give a maximum roughness of 97.3 m and minimum roughness of -103.7 m. The high values (less than -5 m or greater than 5 m) are surrounding Re-entrant E and the main drainage path of the canyon. Moderate roughness (-3 m to 3 m) occurs in the southeast portions of the canyon where NNE-SSW oriented faults occur. Re-entrant W, Re-entrant C, and inside the main drainage path seem to be smooth and have values of -1.5 m to 1.5 m.

A slope direction map is generated by assigning pixel values according to the direction of a cell's adjacent greatest slope (Arc/Info, 1997). For example, if the steepest drop is in the north of the processing cell, the processing cell will be assigned a value of



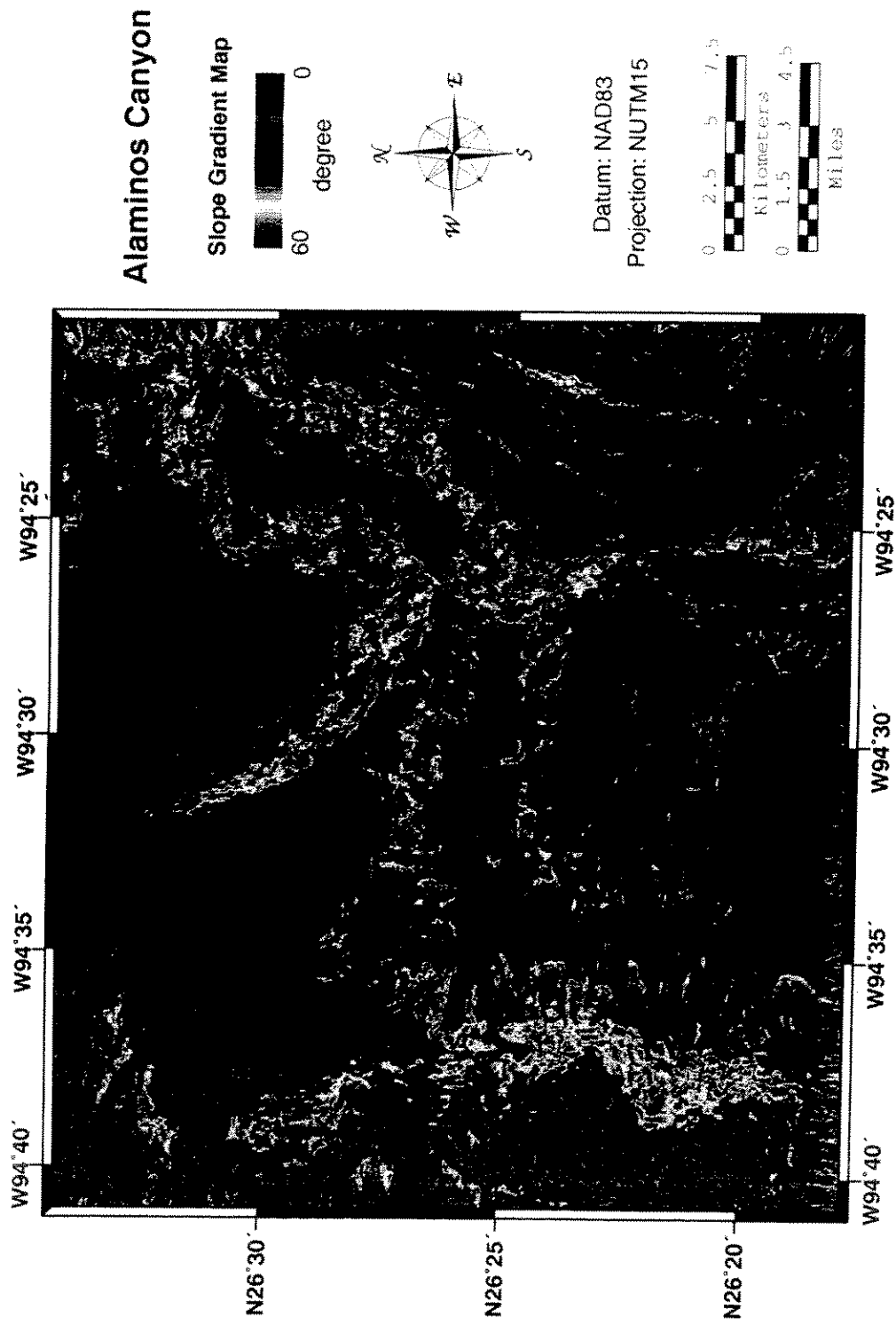


Figure 39-Slope gradient map of the Alaminos Canyon.

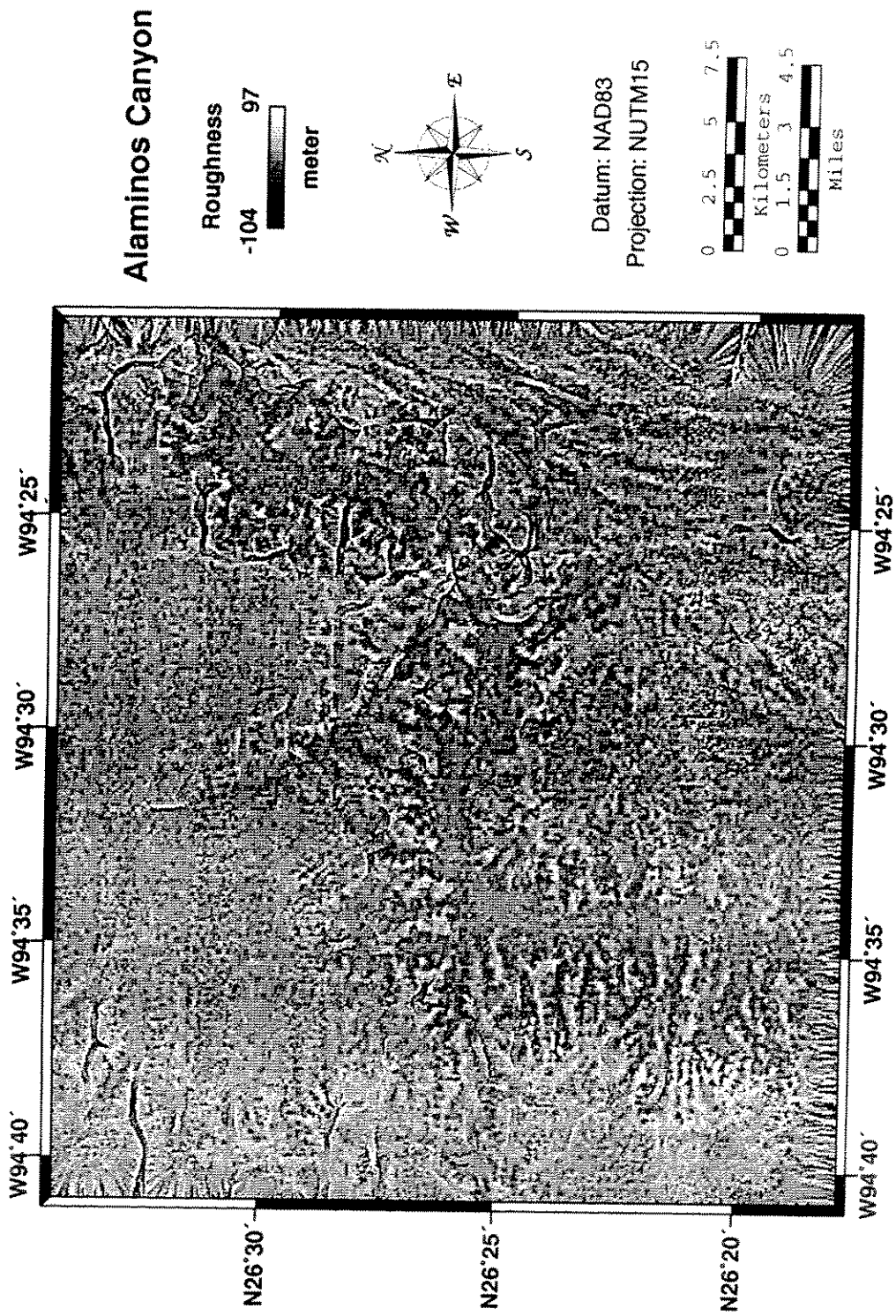


Figure 40.-Seafloor roughness map of the Alaminos Canyon.

64. If a processing cell is lower than its eight neighbors, the cell is given the value of its lowest neighbor (Figure 41). The slope direction map also works like a filter that emphasizes linear structures.

32	64	128
16		1
8	4	2

Figure 41-The assigning of pixel values for a slope direction map (after Arc/Info, 1997).

In the slope direction map, Figure 42, the main drainage path cuts through a series of terraces from east to west then from north to south. Along the northern side of the main path are approximately 2 km wide gullies that are spaced 2 km apart. Along the western side of the main path, the gullies are approximately 1 km wide and 1 km apart. There are fewer and less prominent gullies in the southern and eastern sides of the main path. The faults in the southeast of the canyon are prominent in the slope direction map. These faults seem to continue to the southern central portion of the canyon but are interrupted by the canyon wall. A similar interruption is also observed in the southeast wall of Re-entrant E.

The drainage network is extracted by running a watershed model (GRASS, 1993), which traces the local bathymetric lows and indicates the potential routes for turbidity currents and debris flows from the upper slope to the canyon. Figure 43 shows the drainage paths overlying the slope direction map. The dendritic pattern is analogous to subaerial river systems. The heads of the stream start from the three re-entrants of the canyon and converge to the main drainage path that meanders from east, west, then to the

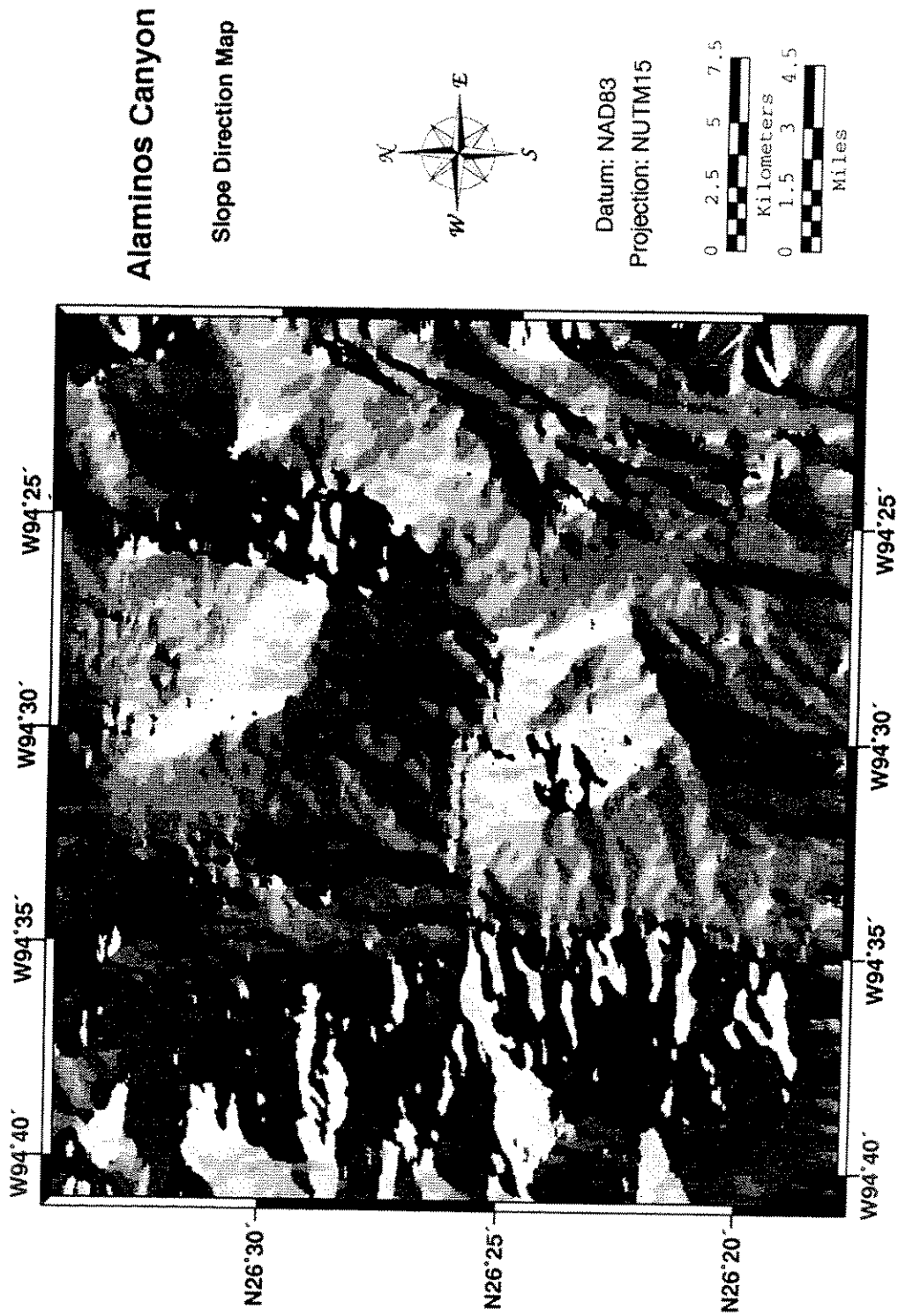


Figure 42-Slope direction map of the Alaminos Canyon.

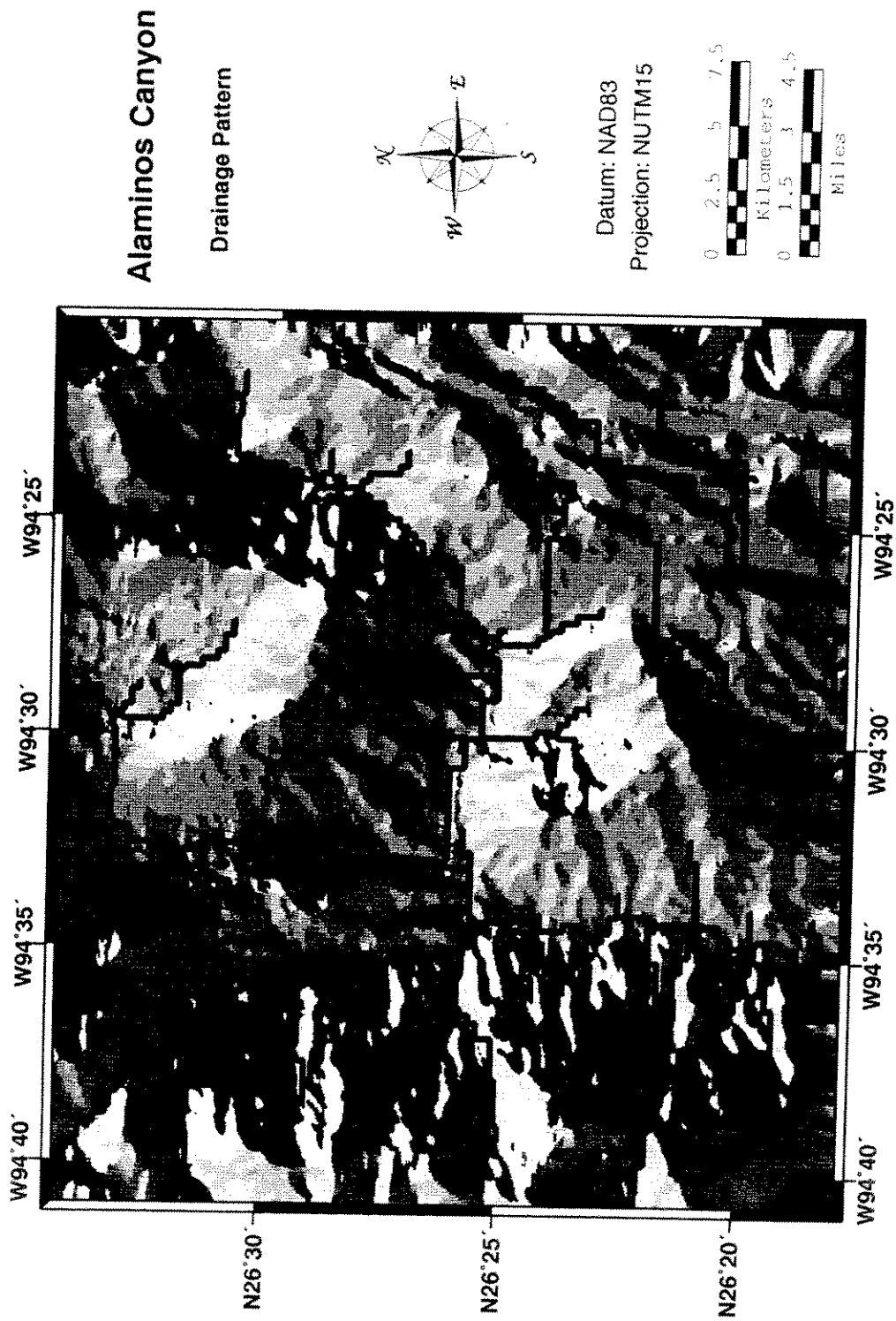


Figure 43-Drainage pattern of the Alaminos Canyon. Blue lines represent drainage paths.

south. In the northern and western sides of the main path, many channels lie in between the ridges indicating the validity of the watershed model. There are very few channels in the southern and eastern sides of the main path suggesting lack of sediment sources. Another separate drainage system occurs in the southeast of the canyon and tends to follow the fault planes. To illustrate the size and shape of the channels and the main drainage path, some bathymetric profiles are drawn. Figures 44-45 show the locations of the profiles, and Figures 46-47 are the profiles.

Lines A-D are the profiles of a channel along the north of the main drainage path (Figure 46(a)). Each profile is about 900 m apart. The channel starts in line A with a V-shape and an about 40 m incision. It becomes narrower and is incised about 60 m in line B. In line C, it has the same 60 m incision but becomes more U-shaped and is confined in a 500 m wide conduit. In line D, the channel flattens out and is incised about 10 m.

Lines E-J are located in the central south of the canyon with each profile spaced about 500 m apart. Lines E-H are along the west of the main drainage path (Figure 46(b)): Two channels are identified by the drainage pattern. The channel on the north starts with a U-shape, with a width of about 600 m, and a 60 m incision. It becomes more V-shaped with a 50 m incision. The conduit becomes less prominent in Line G and flattens out in Line H. The channel in the south starts with a U-shape and an incision of about 20 m. The conduit becomes wider and deeper (about 60 m) in Line F. It becomes shallower and narrower in Lines G and H. The channel on the east side of the main drainage path, Lines I and J, have incisions of about 40 m and 10 m, conduit widths of about 400 m and 600 m, respectively.

Figure 47 shows the profiles of three segments of the main drainage path. Lines 1-4 are in Re-entrant E (Figure 47(a)). Lines 5-8 are profiles of the east-west trending main path (Figure 47(b)). Lines 9-12 are across the southern portion of the main path (Figure 47(c)). Inside each segment, the space between profiles is about 2,000 m. From Lines

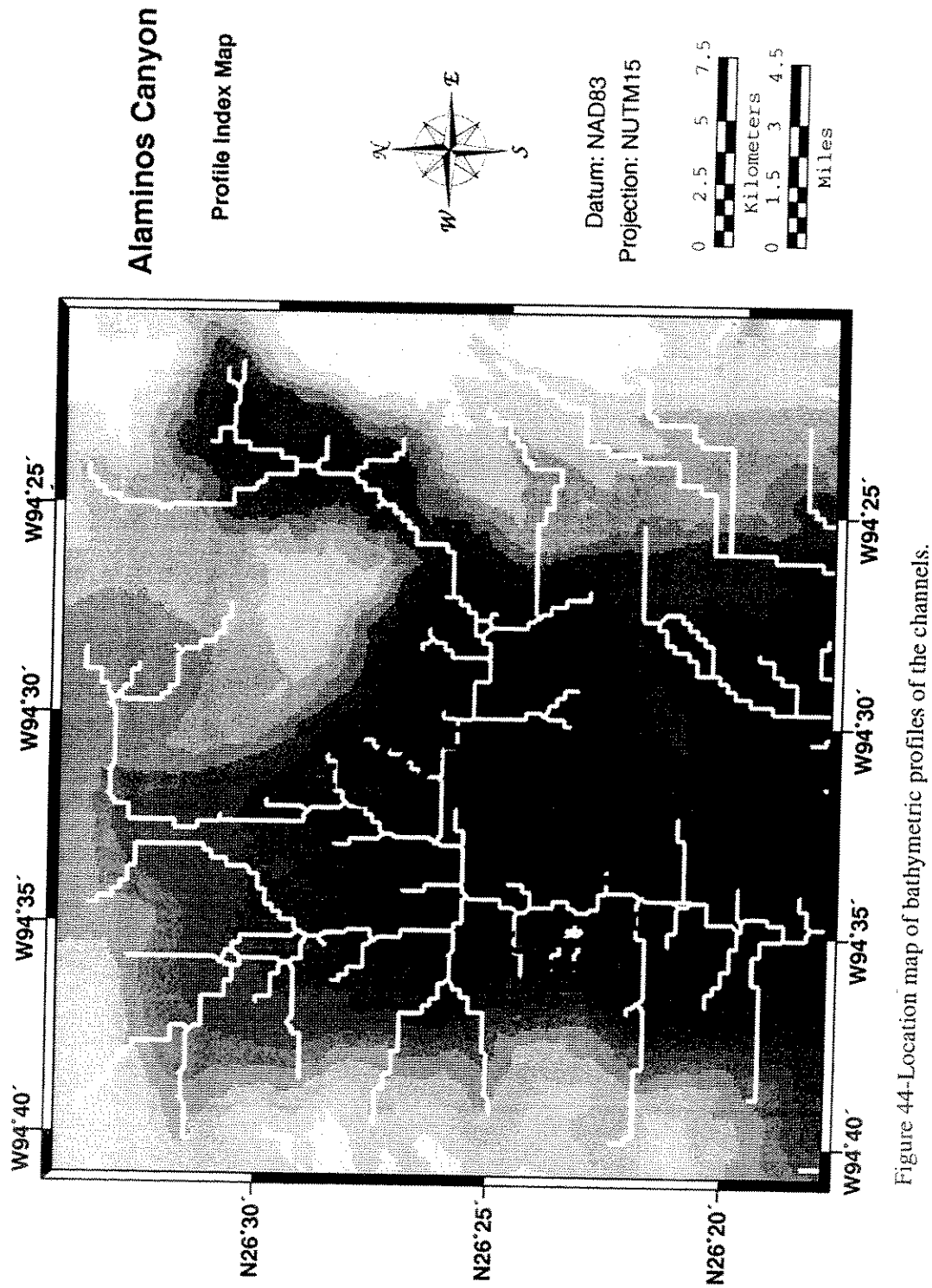


Figure 44- Location map of bathymetric profiles of the channels.

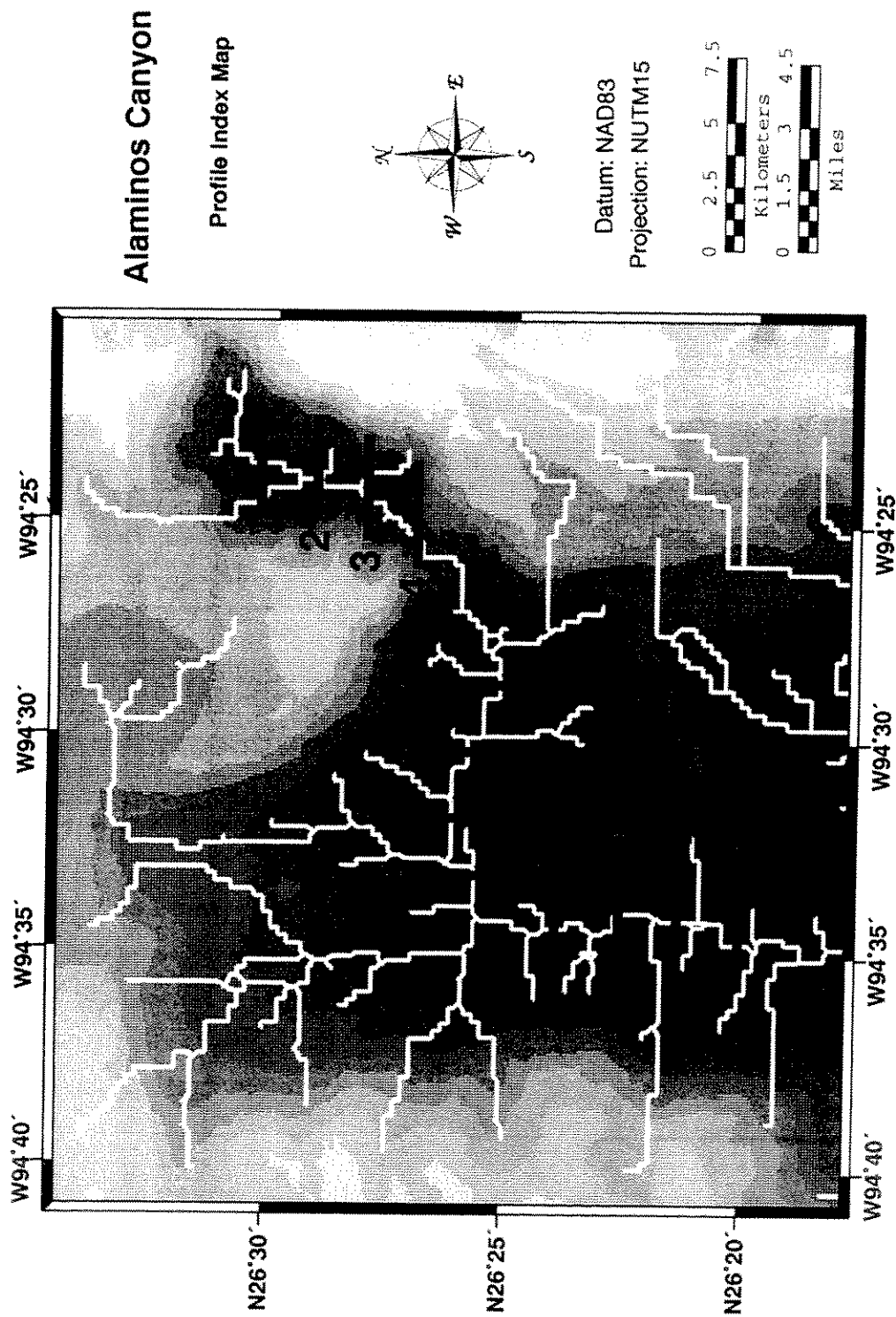
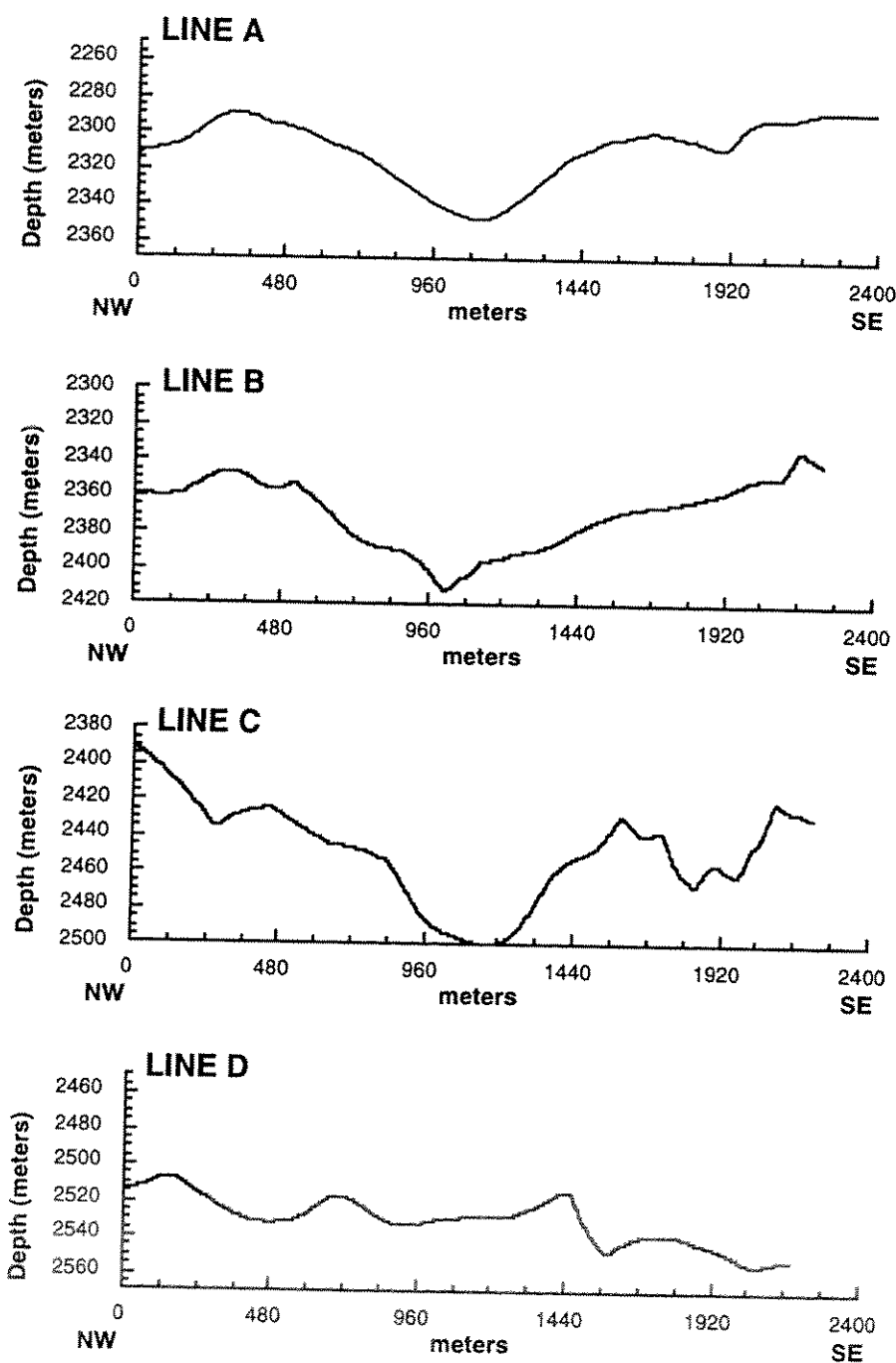


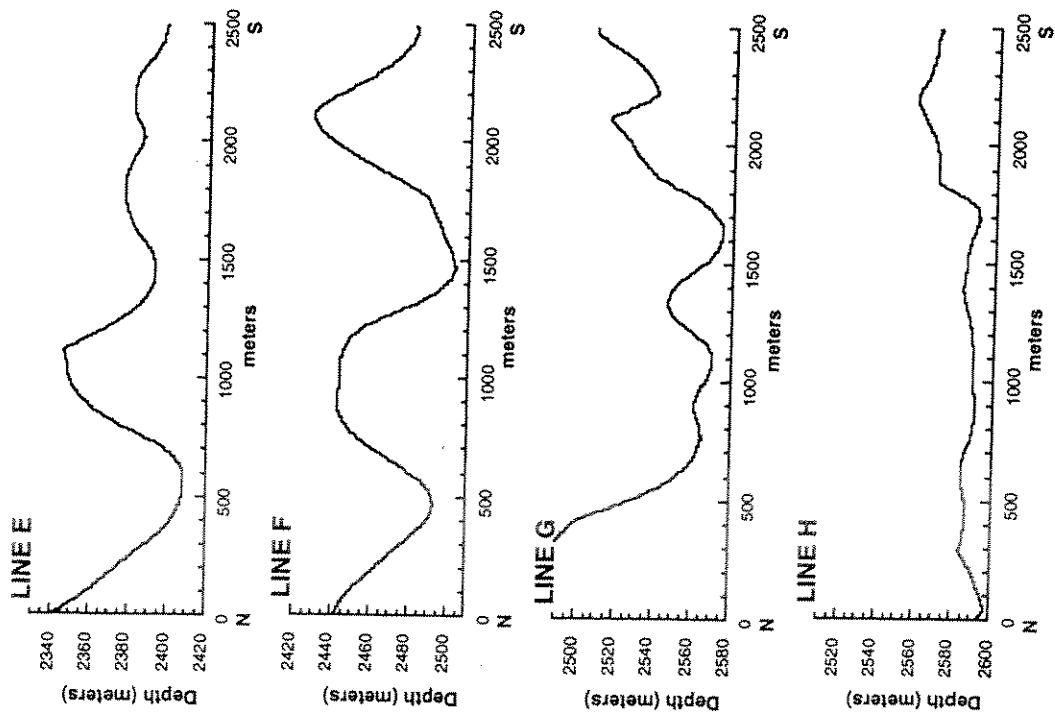
Figure 45-Location map of bathymetric profiles of the main drainage path.



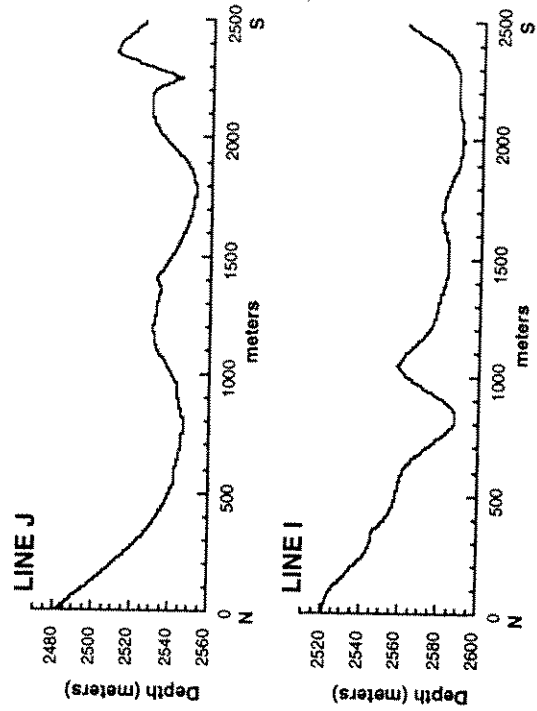


(a) Along the north of the main path

Figure 46-Profiles of the channels along the canyon wall.



(b) Along the west of the main path



(c) Along the east of the main path

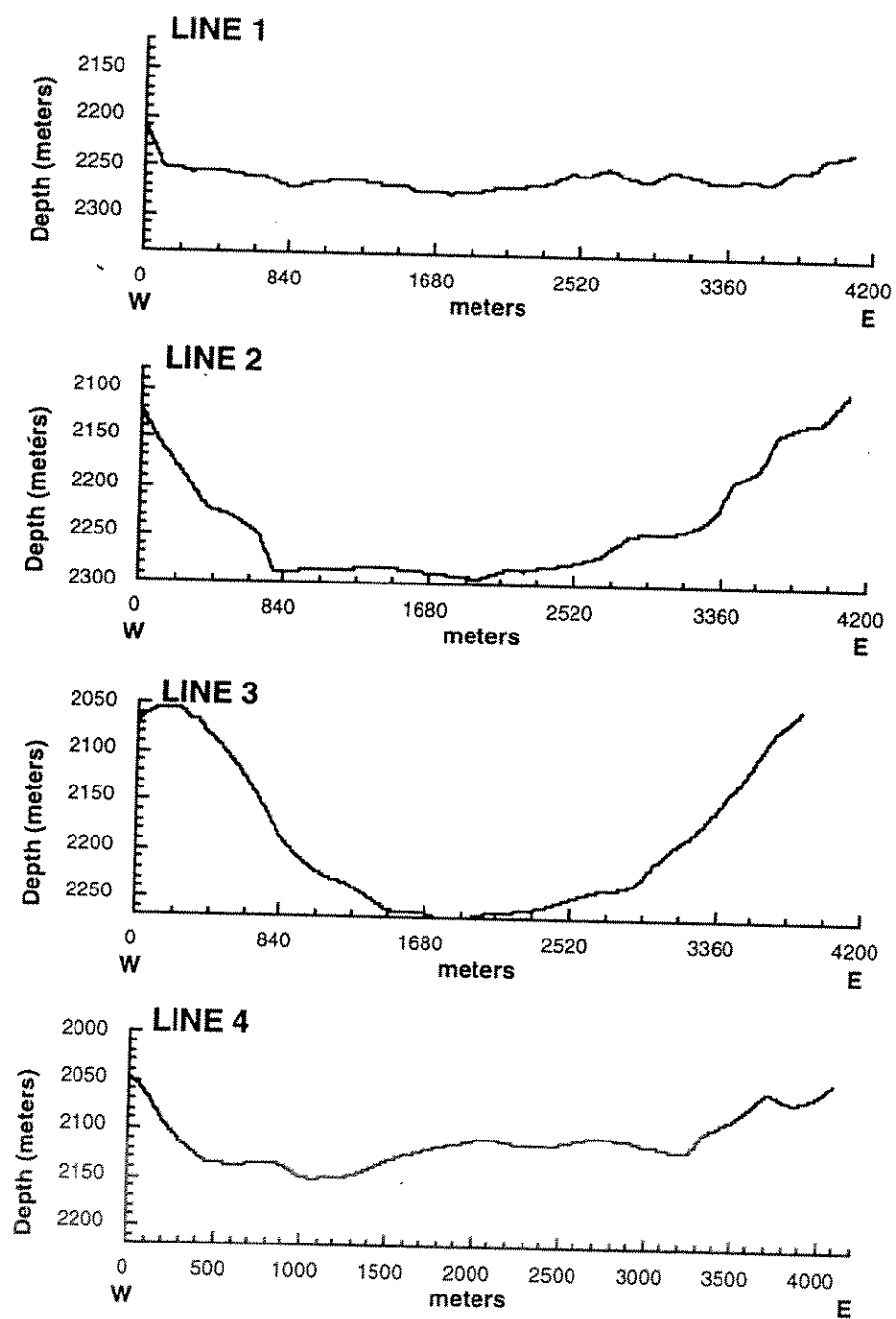


Figure 47-Profiles of the main drainage path of the canyon.

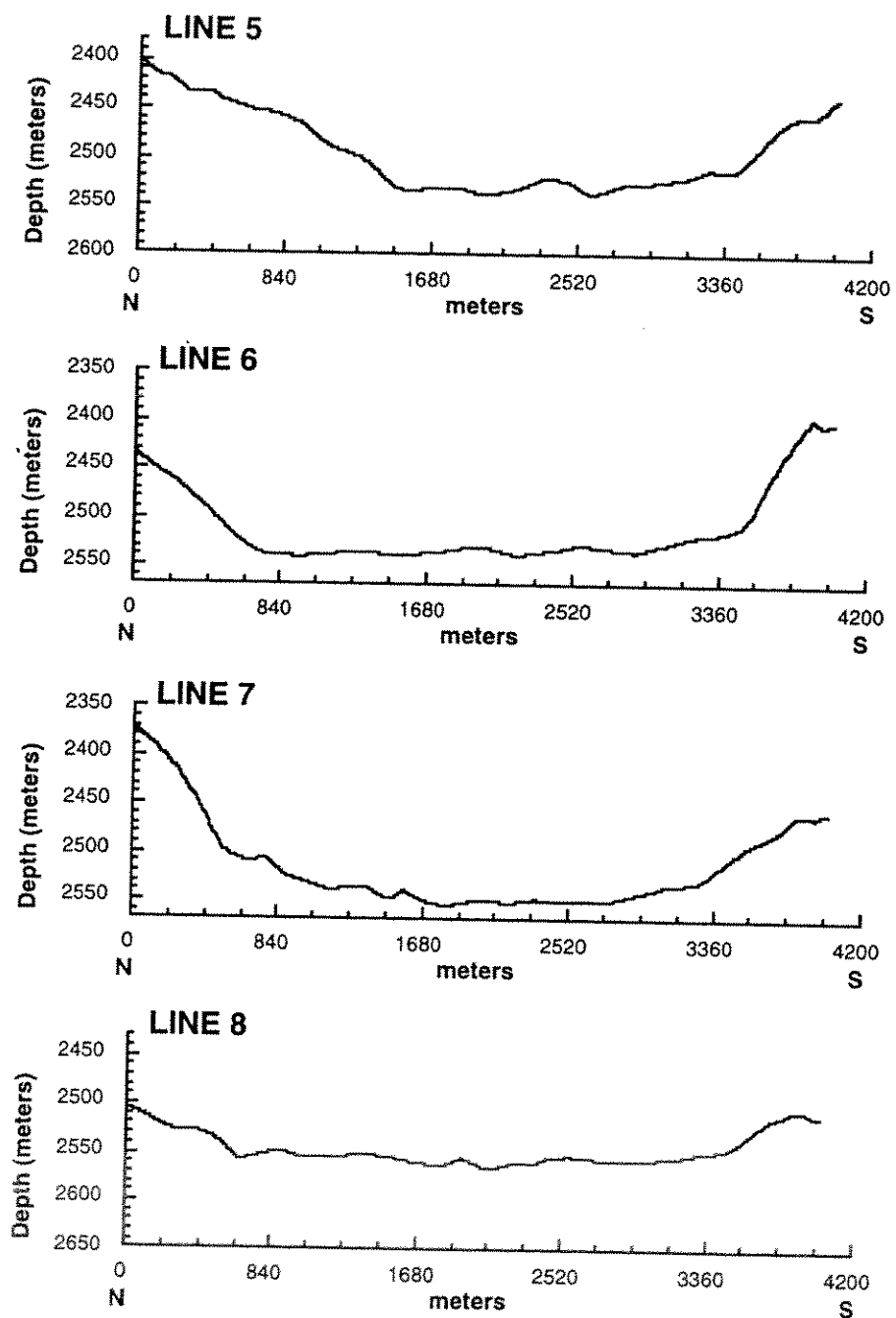


Figure 47-Continued.

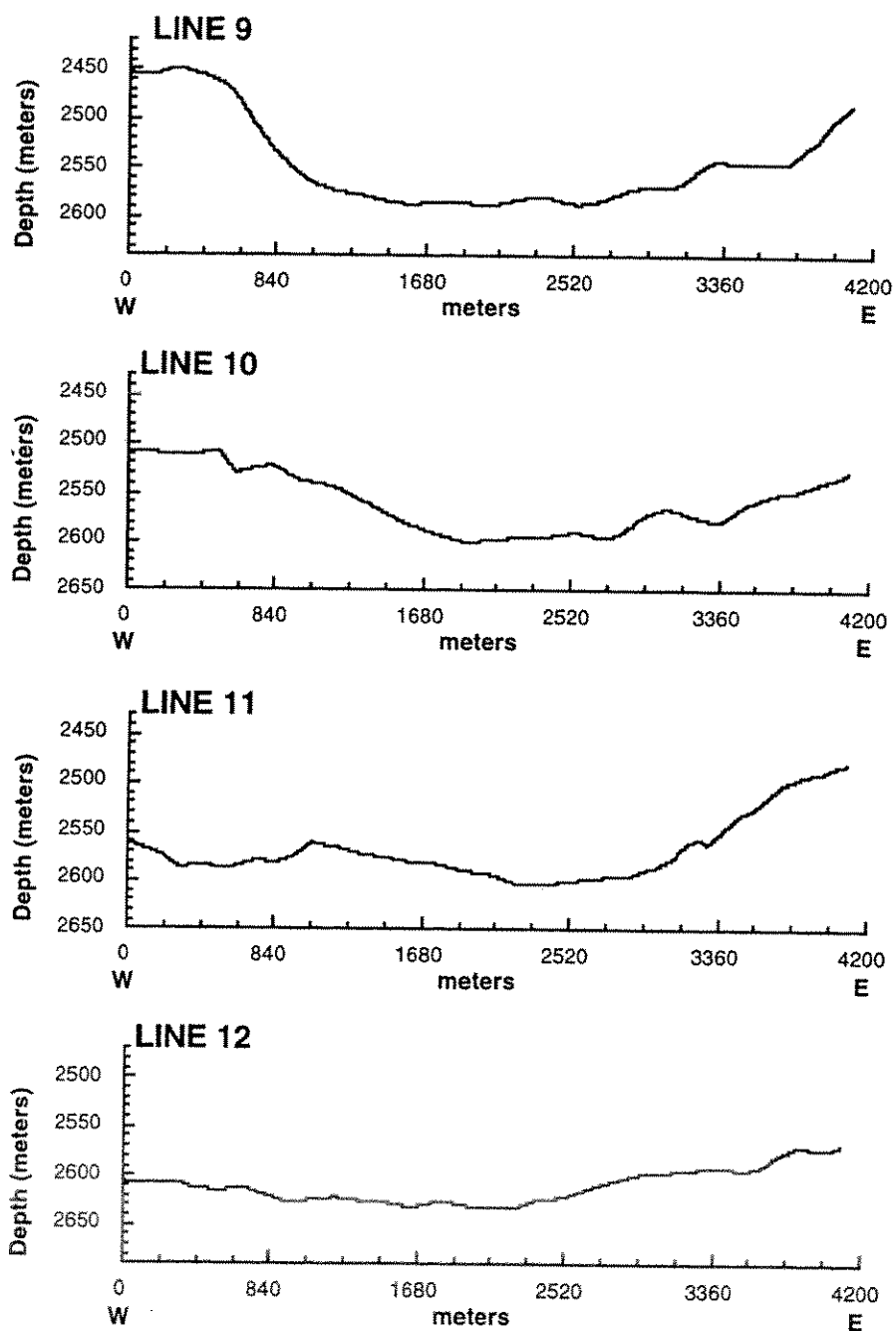


Figure 47-Continued.

1-4, north to south, the drainage path starts with an almost untraceable conduit in Line 1. The conduit becomes U-shaped and has a width of about 4,200 m and incision of about 200 m in Line 2. In Line 3, the width narrows to about 3,500 m and a deeper incision of about 220 m. The main path flattens out, has a nonprominent conduit, and has an incision of about 100 m in Line 4. From Lines 5-8, east to west, the path starts with a less prominent conduit and an incision about 130 m. The conduit becomes more restricted (about 3,800 m), deeper (about 150 m to 200 m), and U-shaped in Lines 6 and 7. In Line 8, the width of the conduit remains the same, but the incision decreases to about 30 m. From north to south, Lines 9-12, the conduit has about the same width of 3,500 m in Lines 9 and 10, becomes about 300 meters narrower in Line 11, and almost untraceable in Line 12. The incision starts with about 150 m in Line 9, then becomes shallower and flattens out in Line 12.

Several patterns and interpretations are concluded from the bathymetric profiles: The small channels on the canyon wall have an average width-depth ratio of 8:1, while the main drainage path has a larger width-depth ratio of 20:1. The large width-depth ratio indicates that the main path carries larger quantities of sediment canyonward. The small channels along the canyon wall appear to be more V-shaped than the main path suggesting that the channels are younger features and are more subject to recent forces. Neither the small channels nor the main path exhibit levees suggesting that the current morphology is caused by debris flows or slumpings and a lack of the kinetic energy of turbulence.

The profiles of the channels on the northern and western walls of the canyon show a downwearing or decreasing in slope angles toward the main path. However, the profiles on the east of the main path display a reverse pattern with an increased slope angle toward the main path. The increase in slope gradient suggests a surface incision of rejuvenating source that might be ascribed to the underlying uplifting salt. The profiles of

the three segments of the main path show an undulation in slope angles in each segment which suggest the main path was not formed by a one time force but by multiple events.

### **Implication of reprocessed GLORIA II image**

Like other sidescan sonar systems, the amorphous DNs shown in the reprocessed GLORIA II image may be attributed to: the inclination of the relief (gradient), microtopography (the roughness of the water-seafloor interface), and sediment texture (sediment characteristics of the seafloor). Unlike backscattering emphasized by the Sigsbee Escarpment and Mississippi Canyon, in the Alaminos Canyon, it is still impossible to identify the canyon wall and channels from the reprocessed GLORIA II image. In the following sections, the GLORIA II image is combined and correlated with Sea Beam bathymetry and ground truth samples, and the factors that contribute to the backscattered image are illustrated.

The size of the footprint is the area where the sonar receives the backscattered energy from the seafloor. In the along-track direction, the footprint is a function of the fore-aft beamwidth and the range. It also increases with distance from the trackline:

$$F_a = \frac{\theta}{57.3} \cdot \sqrt{Z^2 + H^2} \quad (20)$$

where  $F_a$  is the footprint size in the along-track direction,  $Z$  is the sonar altitude,  $H$  is the horizontal range normal to the ship track,  $\theta$  is the fore-aft beam angle ( $2.7^\circ$  for GLORIA II). In the study area, an average altitude of the fish is 2,086 m, the horizontal range in the mosaic image can be up to 6,000 m. The resultant footprint varies from about 98 m in the near range to about 300 m in the far range.

In the across-track direction, the size of the footprint is a function of pulse length, sound speed and grazing angle. It decreases with distance from the trackline (Kleinrock, 1991):

$$F_t = \frac{C \cdot L_p}{\cos(\tan^{-1}(\frac{Z}{H}))} \quad (21)$$

where  $F_t$  is the footprint size in the across-track direction,  $C$  is the two-way sound velocity (750 m/s),  $L_p$  is the length of the pulse in seconds (typical effective pulse length of GLORIA II is 0.01 sec.),  $Z$  is the sonar altitude and  $H$  is the horizontal range. The resultant across-track footprint can vary from about 8 m in the far range to about 86 m, if a near range grazing angle of  $85^\circ$  is assumed.

The spatial resolution is the ability of the sonar to differentiate different characteristics of the seafloor. Theoretically, resolution has the same dimension as the footprint. However, resolutions are determined by some other factors for a sidescan sonar sonograph, in which the seafloor is not totally covered by the footprint. In the near range, there are gaps between footprints in the along-track direction. In the far range, the footprints are overlapped. In the across-track direction, the footprints are overlapped in the near range and gapped in the far range. This is because the sizes of the footprints are varied, but the spacing of the footprint is fixed. In the along-track direction, the spacing is determined by the rate of the signal being emitted and received, and by the traveling speed of the fish (ship speed). In the across-track direction, the spacing is determined by the sample digitization rate; it equals the swath width divided by the number of digitizing data points. For the GLORIA II data used in this study, there are 1,000 points for each scan.



The pixel size is the size of the DNs displayed on the sonograph. Usually, it is the optimum size determined by the across-track spacing to avoid losing any data in the final display step. As the pixel size has an equal dimension, in the along-track direction, the sonograph is usually oversampled. Another factor determining whether an object can be detected by the sonar is the object's size compared to the wavelength of the acoustic signal. The minimum detectable size lies between a twelfth and half of the wavelength of the signal. With an averaged wavelength of 23 cm for GLORIA II, the size will be 1.9 cm to 11.5 cm. In summary, the resolution is determined by the size of the footprint, the space of the digitization, the size of the pixel, and the frequency of the sonar system.

The released GLORIA II data has a swath width of about 45 km or about 22.5 km on each side with a far-range grazing angle close to 0°. In this study, the meaningful DNs are located in between the 280th to 340th pixels (including the near-range noisy zone). Excluding the far-range no value zones, the minimum grazing angle is about 15°. The grazing angles for the locations of the ground truth samples can be approximated based on the georeferenced bathymetry data, distance of the pixel to nadir, and the water depth. According to the grazing angle, the size of the footprint in these locations can also be calculated (Table 5). The averaged size of the footprint in the ground truth locations is about 150 m by 10 m. A gridding space of 50 m is used for both bathymetry and sidescan imagery in this study to look for other properties in these ground truth locations.

To evaluate the factors affecting the backscattered image, a method adapted from Gardner et al. (1991) is used. First, the Rayleigh criterion is used to determine the effects of the seafloor roughness:

$$R = k \cdot H \cdot \sin \phi \quad (22)$$

where  $k$  is the acoustic wave number ( $2\pi/\lambda$ ),  $\lambda$  is the wave length of the signal,  $H$  is the surface roughness or the height of the surface regularities, and  $\phi$  is the grazing angle. When  $R \ll 1$ , it represents a smooth surface where all the incident energy is reflected; when  $R \gg 1$ , it represents a rough surface where incident energy diffusely scatters at all angles. Table 6 lists the parameters derived from the bathymetry, resulted  $R$  values and the DNs of the extracted NGDC GLORIA II image and reprocessed image.

Table 5. Grazing angle and footprint size (F.S.) in the ground truth locations

	AC01	AC02	AC03
Fish altitude (m)	2492.5	2330.1	1781.0
Horizontal range (m)	1863.2	2498.7	1967.7
Grazing angle ( $^{\circ}$ )	53.2	43.0	42.2
Along-track F.S. (m)	146.6	161.0	125.1
Across-track F.S. (m)	12.5	10.3	10.1

The resultant  $R$  values are all greater than 1. If we consider that the sonograph used in this study has been corrected for the influence of grazing angles, the  $R$  values will be even greater than shown in the table. As a result, all the ground truth locations are classified as rough seafloor, which is different from what has been observed from the seafloor roughness map. However, the DNs in these locations only suggest moderate backscattering in the study area. This is because the DN values are relative (after conversion from 12-bit recorded backscatter amplitude to 8-bit Bell mu law compression and from later modification, the values are redistributed between 0 to 255).

Table 6. Rayleigh roughness and DN values in the ground truth locations

Core	Slope gradient (°)	Roughness (m)	R	DN (NGDC/reprocessed)
AC01	3.5	0.7	15.3	68 / 51
AC02	2.8	1.3	24.2	152 / 89
AC03	4.3	0.3	5.5	106 / 63

As to the sediment depth extent the sonar signal represents, we can examine the percent of the energy passed through the sediment below the seafloor:

$$E_n = \frac{E_i \cdot T}{10^{(\alpha \cdot D_p / 10^3)}} \quad (23)$$

where  $E_n$  is the percent of energy passed through each interface,  $E_i$  is the incident energy,  $T$  is the transmission coefficient,  $\alpha$  is attenuation in dB/m, and  $D_p$  is the length of the traveling path in cm. In this study, a sediment interval of 1 cm is used for the calculation.

The transmission coefficient,  $T$ , can be calculated from Zoeppritz' equations (1919). For a P-wave at normal incidence:

$$T_n = \frac{4\delta}{(\delta + 1)^2} \quad (24)$$

$$\delta = \frac{V_{p2}\rho_2}{V_{p1}\rho_1} \quad (25)$$

where  $T_n$  is the normal transmission coefficient,  $\delta$  is the impedance contrast, and  $V_{p1}$ ,  $\rho_1$  and  $V_{p2}$ ,  $\rho_2$  are the P-wave velocity and density for the overlying layer and calculated

layer. When the angle of incidence is not normal, the P-wave transmission coefficient can be expressed as (Cerveny and Ravindra, 1971; Young and Braile, 1976):

$$T = \frac{V_{p2}\rho_2P_3}{V_{p1}\rho_1P_1} R_d \quad (26)$$

$$R_d = \frac{2V_{p1}\rho_1P_1(V_{s2}P_2X + V_{s1}P_4Y)}{D} \quad (27)$$

where  $R_d$  is the refraction coefficient in terms of displacements,  $V_{s1}$  and  $V_{s2}$  are the S-wave velocity of the overlying layer and calculated layer, and

$$P_1 = \sqrt{1 - V_{p1}^2\Theta^2}, \quad (28)$$

$$P_2 = \sqrt{1 - V_{s1}^2\Theta^2}, \quad (29)$$

$$P_3 = \sqrt{1 - V_{p2}^2\Theta^2}, \quad (30)$$

$$P_4 = \sqrt{1 - V_{s2}^2\Theta^2}, \quad (31)$$

$$\Theta = \frac{\sin \theta}{V_{p1}}, \quad (32)$$

$$X = \rho_2 - q \cdot \Theta^2, \quad (33)$$

$$Y = \rho_1 + q \cdot \Theta^2, \quad (34)$$

$$Z = \rho_2 - \rho_1 - q \cdot \Theta^2, \quad (35)$$

$$\text{and } q = 2(\rho_2 V_{s2}^2 - \rho_1 V_{s1}^2) \quad (36)$$

The sea water velocity of 1,521 m/sec (Fofonoff and Millard, 1983; assuming salinity of 35 ‰ and temperature of 20°C) is used for the calculation of the incidence angle ( $\theta$ ) between the sea water and seafloor interface. Shear-wave velocity is adopted from Hamilton's (1976) in-situ silt-clay measurement for depths less than 40 m in water-saturated silt-clay:

$$V_s = 116 + 4.65D \quad (37)$$

where  $V_s$  is the shear-wave velocity in m/sec, and  $D$  is the depth below seafloor in meters.

The P-wave attenuation,  $\alpha$ , in dB/m is calculated from Hamilton (1972):

$$\alpha = kf^n \quad (38)$$

where  $f$  is frequency in kHz,  $n$  is the exponent of frequency and is close to 1, and  $k$  is a constant that can be calculated from porosity ( $\phi$ ):

$$\begin{aligned} \text{for porosity from 46.7\% to 52\%: } & k = 0.04903\phi - 1.7688 \\ \text{for porosity from 52\% to 65\%: } & k = 3.3232 - 0.0489\phi \\ \text{for porosity from 65\% to 90\%: } & k = 0.7602 - 0.01487\phi + 0.000078\phi^2 \end{aligned} \quad (39)$$

The length of the signal travel path for every sediment interval,  $D_{tp}$ , is calculated from:

$$D_{ip} = \frac{D_2 - D_1}{\cos(\sin^{-1}(\sin \theta (V_{p2} / V_{p1})))} \quad (40)$$

where  $D_1$  and  $D_2$  are the depths of the overlying layer and calculated layer.

Figure 48 shows the transmitted energy in dB versus depth for the ground truth locations. At the bottom of AC01 (842 cm), AC02 (782 cm), and AC03 (771 cm), the energy levels are 6.34 dB, 6.51 dB, and 18.47 dB down, or they retain 23.21%, 22.34%, and 1.42% of their incident energy, respectively. Both AC01 and AC02 show near linear transmitted energy attenuation because of their closeness in physical properties.

However, the attenuation rates are about 0.76 dB/m for AC01 and about 0.84 dB/m for AC02. The higher attenuation rate of AC02 can be explained by a smaller surficial incident angle (Table 5) and longer signal travel path for a same normal incidence depth. The acoustic energy attenuation curve of AC03 shows two linear segments. From 0 cm to about 540 cm, the energy decreases at a rate of about 1 dB/m, while from about 540 cm to 771 cm, the rate of decrease is about 5.6 dB/m. As the surficial incident angles for AC02 and AC03 are about the same, the higher energy attenuation rate of AC03 is more related to the material of the sediment. This is especially true at depths below 540 cm, where both P-wave velocity and bulk density increase drastically (Figure 35). All of these calculated attenuation rates are higher than the 0.5 dB/m from Gardners' study in the Monterey Fan off south central California (Gardner et al., 1991). The higher attenuation rate may be explained by the more dense material of the sediment and the shallower water depth of the study area (4,450 m for Gardners' study).

In terms of attainable depth into the sediment for the recorded GLORIA II imagery, a deep towed 3.5 kHz profiler can record about 60 ms (TWTT) of sediment. In the study area, a typical surficial P-wave velocity is about 1,480 m/sec, thus the penetration depth is about 44 m. For a surface towed 6.5 kHz GLORIA II, the sonar

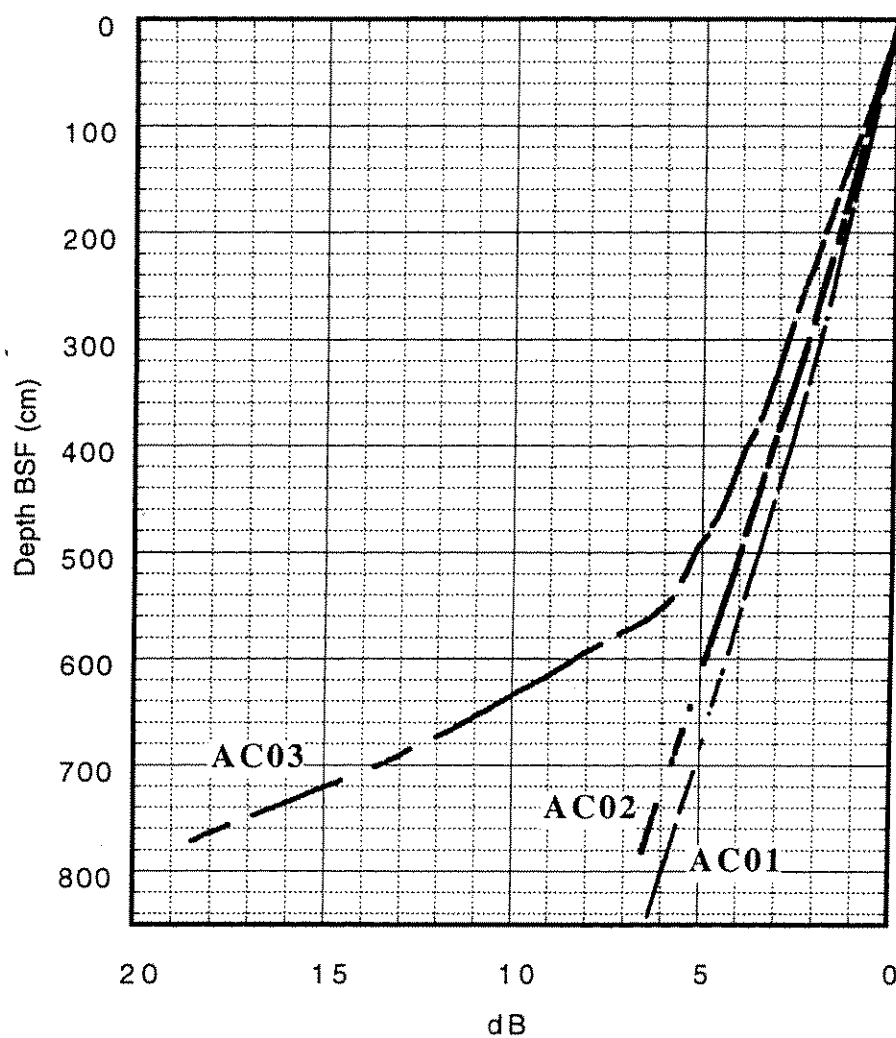


Figure 48-Transmitted GLORIA II acoustic energy versus depth in the ground truth locations.

energy has dropped 3 dB or 50% of incident energy at depths of 440 cm, 384 cm, and 325 cm for AC01, AC02, and AC03, respectively. At a depth of 700 cm, the sonar energy can drop from 5.2 dB (AC01) to 13.5 dB (AC03). Assuming the same attenuation rates for the sonar energy to reach the recorder from the detected target, the GLORIA II imagery might represent the characteristics of less than 10 meters of surficial sediment.

During the calculation of transmission coefficient (T), regardless of the incidence angle, all values in the ground truth locations are close to 1 throughout the sampled depths. To check whether the resolution of the sonar signal may have affected the result, the transmission coefficients based on a 5 cm sediment interval were calculated for AC01. The resultant T values still show close to 1. This might be explained by the almost identical properties or the homogeneity of adjacent layers in the ground truth locations.

Location accuracy is another factor to consider. It can be grouped into accuracy of navigation, fish position, and flat floor assumption. The navigation system used for the GLORIA II during the survey of Alaminos Canyon was loran-C, while Global Positioning System (GPS) was also logged for comparison. The estimated position accuracy is about 200 m (EEZ-Scan 85 Scientific Staff, 1987). During pre- and post-processing, the fish is assumed to be at the same position as the ship whereas in fact the fish is towed behind the ship about 400 m. The displacement caused by the assumption of a flat seafloor can be expressed by (Li, 1992):

$$\Delta D_h = \sqrt{D_h^2 + 2D_f\Delta Z + \Delta Z^2} - D_h \quad (41)$$

where  $\Delta D_h$  is the displacement of the pixel,  $D_h$  is the horizontal distance from the fish to the correct position,  $D_f$  is the altitude of the fish,  $\Delta Z$  is the depth difference of the corrected position and nadir. In this study, for a  $D_f = 23,000$  m, in the near range situation with a  $D_h = 1,000$  m and  $\Delta Z = 30$  m, the  $\Delta D_h = 67$  m; in the medium range situation with



a  $D_h = 3,000$  m and  $\Delta Z = 100$  m, the  $\Delta D_h = 77$  m; in the far range situation with a  $D_h = 6,000$  m and  $\Delta Z = 200$  m, the  $\Delta D_h = 79$  m. All the displacements caused by the flat seafloor assumption seem to be only a few pixels away from the real positions. Overall, the greatest location inaccuracy is caused by the fish's position.

Another consideration is "Lambert's Law" which states that when a surface has uniform microscale roughness, then the backscattering strength is a function of the square of the sine of the incidence angle (Urlick, 1983). This causes features that are perpendicular to the survey routes to be muted while features that are parallel to the survey routes are enhanced. In the case of the study area, this might explain the lack of variation in backscattering strength of the north-south oriented canyon wall.

### **Other support data**

Outside the Sea Beam coverage, the digitized contour lines based on the Petty-Ray seismic data (Bryant et al., 1990) are converted to digital elevation models (DEMs) using iterative finite difference interpolation technique (Wahba, 1990; Arc/Info, 1997). Figure 49 is the composite contour map along with the locations of other support data. It appears that the canyon starts from the north of the Sea Beam coverage with two re-entrants. There is a depositional fan to the southwest of the canyon mouth.

The salt distribution in the Alaminos Canyon area has been mapped by Simmons (1992). Seismic interpretation suggests that except in the northeast, the canyon is free of shallow salt (less than 4 secs TWTT). A recent paper published by Trudgill et al. (1997) indicates that inside the canyon there are salt structures at depths below 7 secs TWTT. In the following sections, two TAMU Deep Tow lines collected in 1996 and one seismic profile published by Fiduk et al. (1996) are used to illustrate the sediment structure and geomorphology.

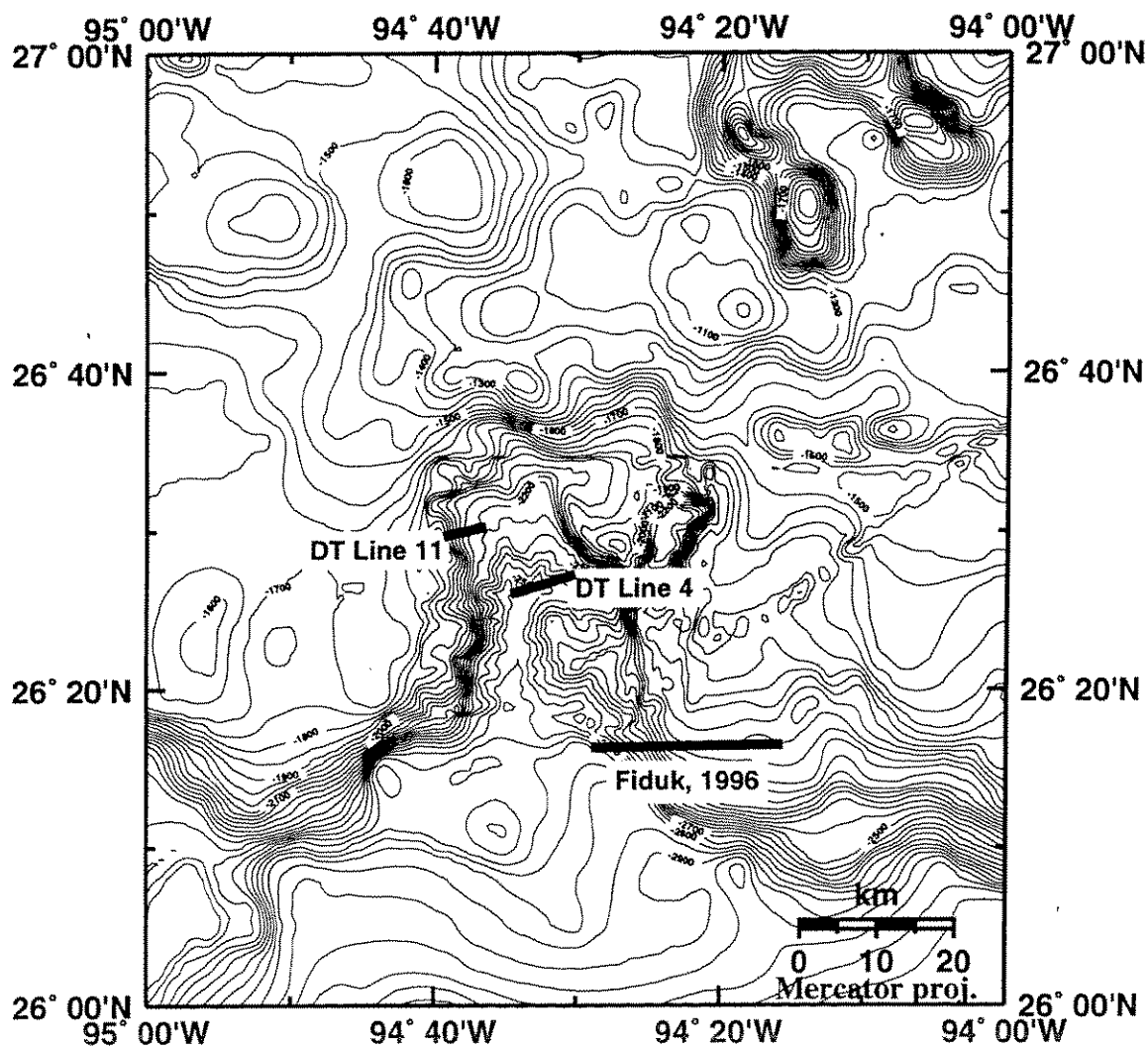


Figure 49-Composite contour map of the Alaminos Canyon area with locations of support data. Contour interval 50 meters.

Line 11 is a TAMU Deep Tow line running across the northwest wall of the canyon. Figure 50(a) is the original record, and Figure 50(b) is the interpreted profile. Starting from the southwest portion of Deep Tow Line 11, the upper 10 msec contains a semi-transparent zone. This zone thins toward the canyon rim and pinches out against contorted bedding on the canyon wall. A broad band reflector in the bottom of the semi-transparent zone may be traced down canyon where it thickens and becomes translucent. To the southwest of the line, underlying the semi-transparent zone are tightly-spaced continuous reflectors. These continuous reflectors become chaotic and contorted toward the canyon wall then become transparent with linear strikes canyonward. Between the continuous and contorted reflectors are a few normal faults. Folding occurs near the southwest of the line. The faulting and folding indicate a lateral compressional force and an underneath salt uplift on the margins of the profile. A reflector inside the semi-transparent zone indicates a sudden change in sediment property and may reflect the influence of intermittent uplift of the canyon rim. The contorted and chaotic reflectors in the middle portion of the profile indicate slump deposits. These slumps are overlain by few non-uniform reflectors which suggest the slumps might still be creeping canyonward. The boundary between semi-transparent zone and continuous reflectors may represent the Holocene/Pleistocene boundary which separates mainly pelagic deposits from turbidity current dominated deposits. However, the nonuniform thickness of the Pleistocene facies suggest that the deposition of the canyon during the Pleistocene is either subject to underlying salt movement, active creeping of slumps, or other deposition source than pelagic sediment.

TAMU Deep Tow Line 4 lies across the main drainage path of the canyon. Figure 51(a) is the original record, and Figure 51(b) is the interpreted profile. The broad band reflector at TWTT about 15 msec below seafloor may be the speculative Holocene/Pleistocene boundary observed in Deep Tow Line 11. The highly faulted and

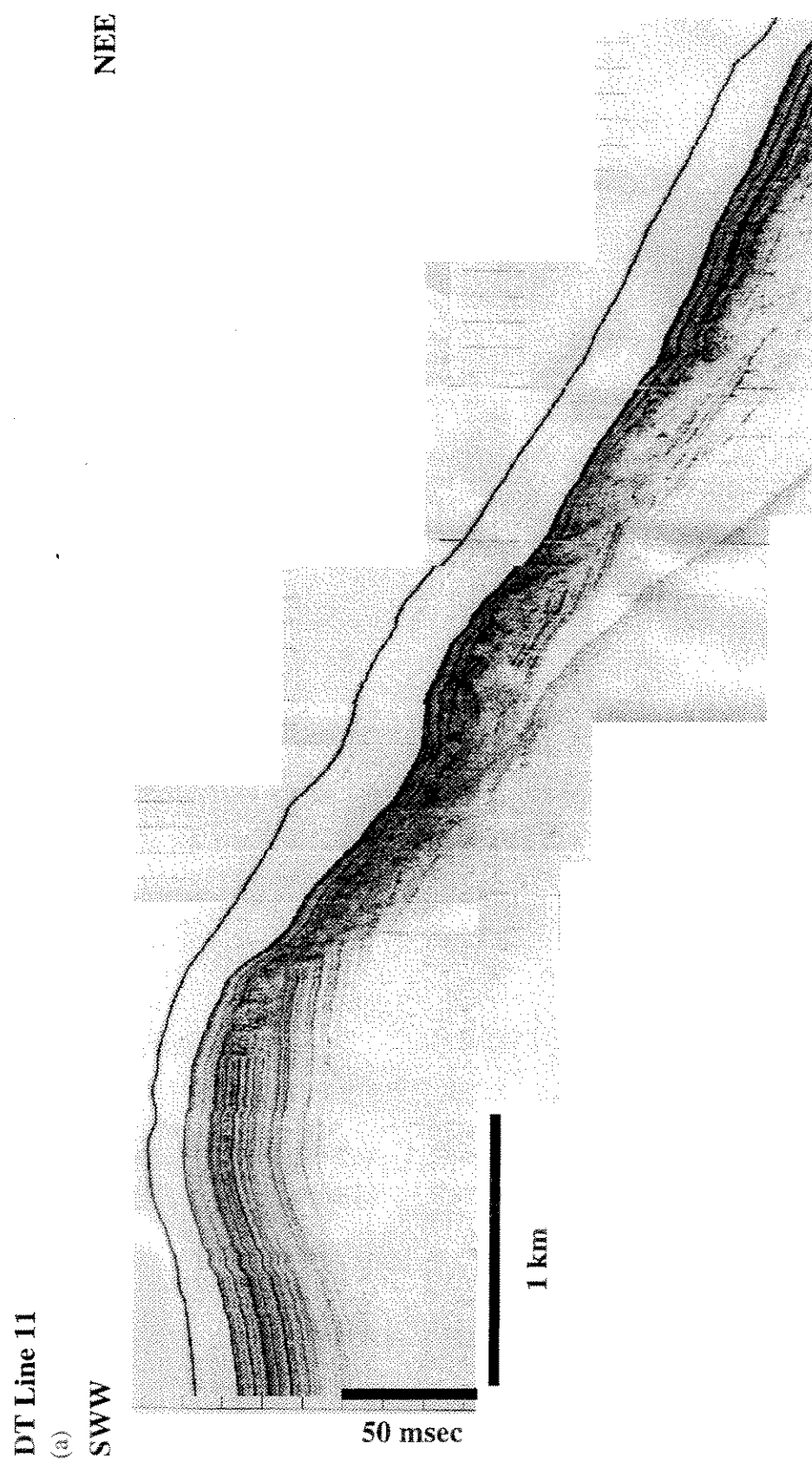


Figure 50-TAMU Deep Tow Line 11. (a) Original record. (b) Interpreted profile.

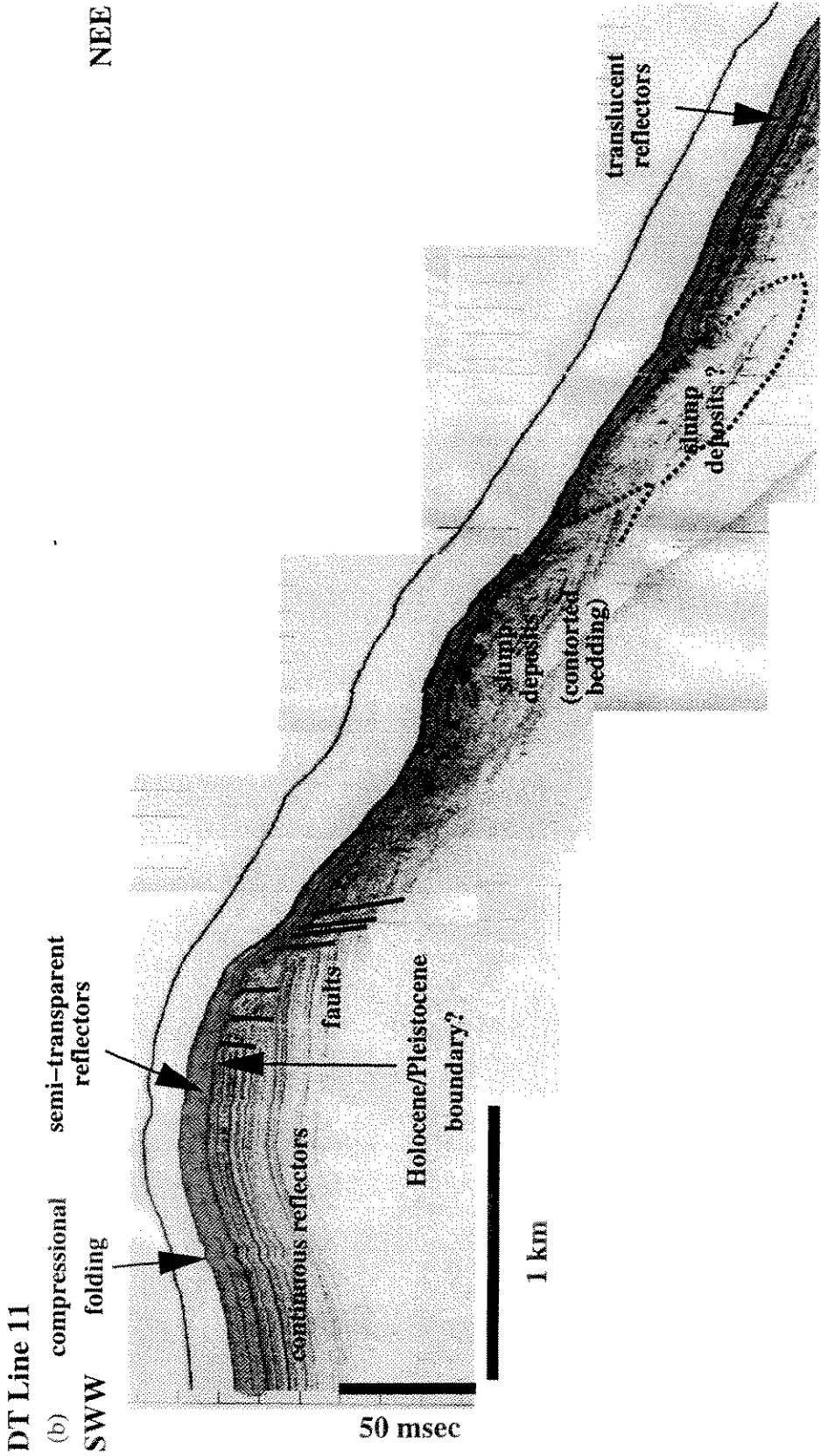


Figure 50-Continued.

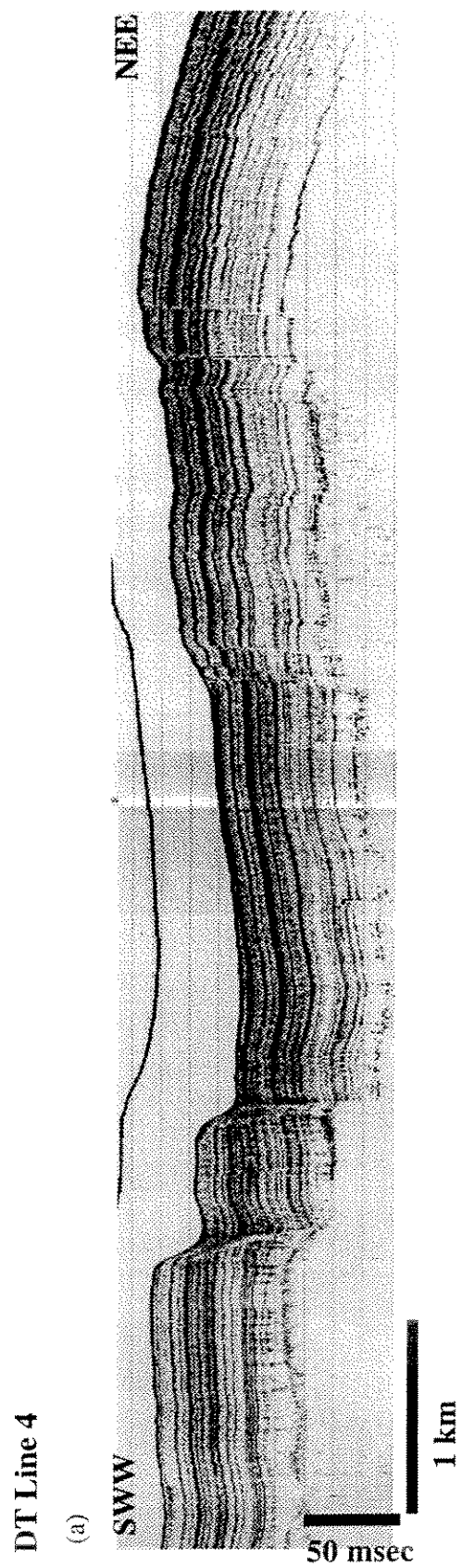


Figure 51—TAMU Deep Tow Line 4. (a) Original record. (b) Interpreted profile.

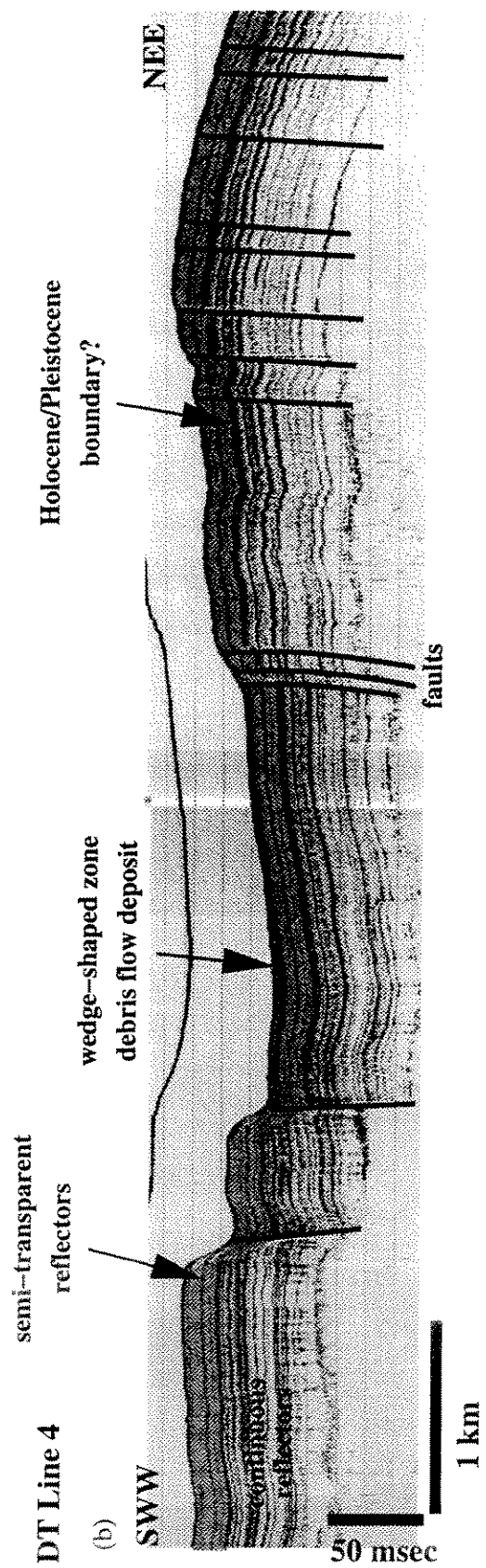


Figure 51-Continued.

graben-like features along the main channel path may be explained by the underlying salt uplifting. Most of the faults penetrate the seafloor, and sediment across these fault planes have equal thickness, indicating these faultings are very recent events. The small channels identified by the drainage pattern map are believed to follow these fault planes and flow in a direction toward the viewer. Except a wedge shaped zone in the uppermost middle portion, the presumed Holocene deposits are uniformly distributed in Line 4. If debris flow contributes to this Holocene layer, it must have similar influence across this profile. The wedge shaped zone that has same semi-transparent reflector may represent a local debris flow deposit that was transported through upper channel.

The seismic line published by Fiduk et al. in 1996 is adjacent to the linear faults observed in the southeast portion of the canyon (Figure 52). The top of the salt is about 0.5 secs TWTT below the seafloor. According to their interpretation, the faults are caused by the contraction folding of salt and the overthrusting of sediments. As the faults cut through both 5.5 Ma horizon and the seafloor, the thrusting was dated after 5.5 Ma. In Fiduk's published paper, the seismic profiles are located on an about 6.5 km spaced grid. In this study, the spaces between soundings used from Sea Beam are about 75 m to 120 m. Although it is impossible to predict normal faults or reverse faults from bathymetry data, it is apparent that the multibeam generated bathymetry can delineate the extent of shallow faults at a resolution of more than 50 times of the 2-D seismics.

### **Geological interpretation**

By combining all the observations, Figure 53 is a line drawing illustrating the surficial geology of the study area. The study area is located in the lower slope with shallow allochthonous salt surrounding the canyon. Re-entrant W and Re-entrant C in the central northwest of the canyon have low slope gradient and lack of gullies on the wall.



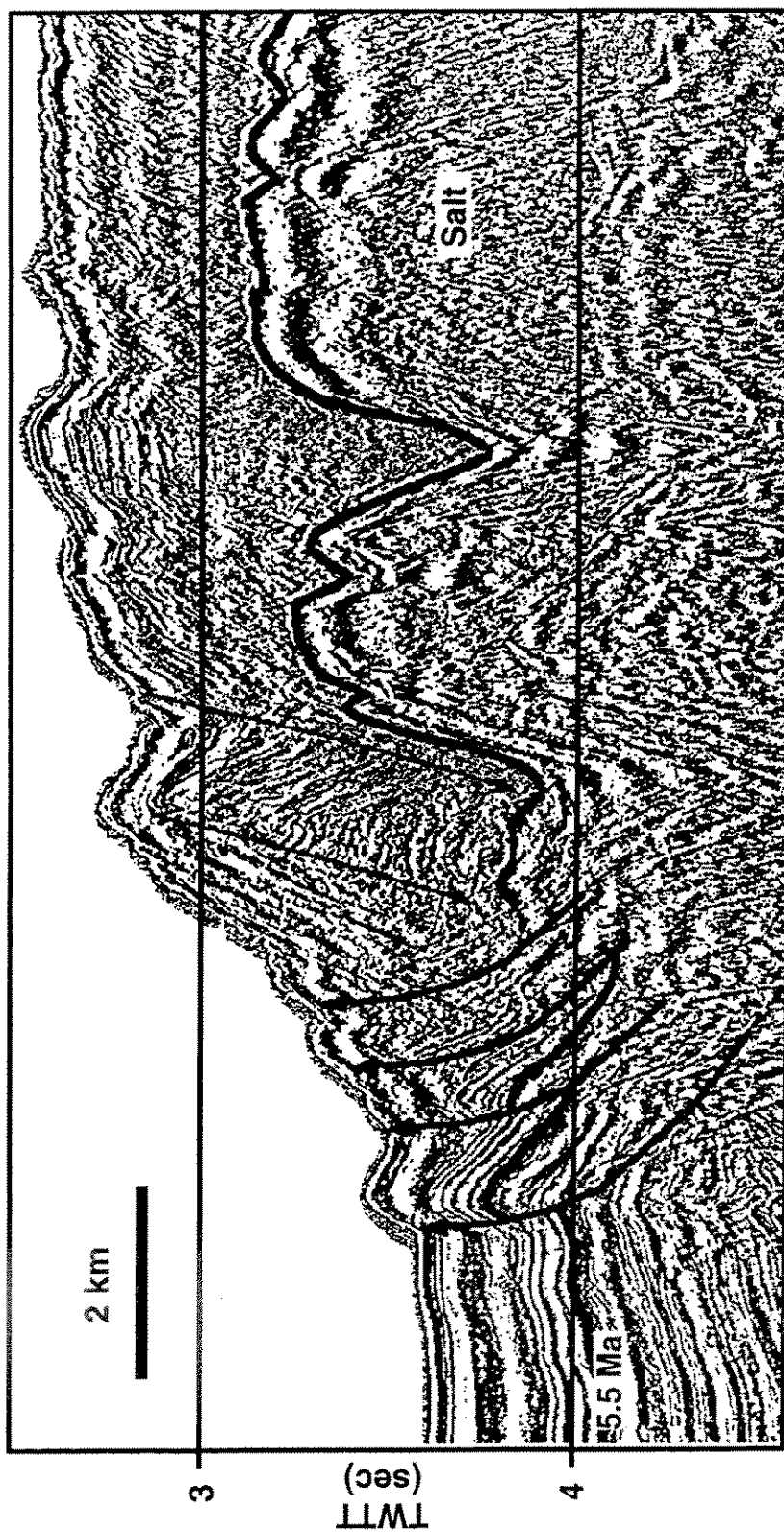


Figure 52—Seismic profile in the southeast of the Alaminos Canyon (After Fiduk et al., 1996)

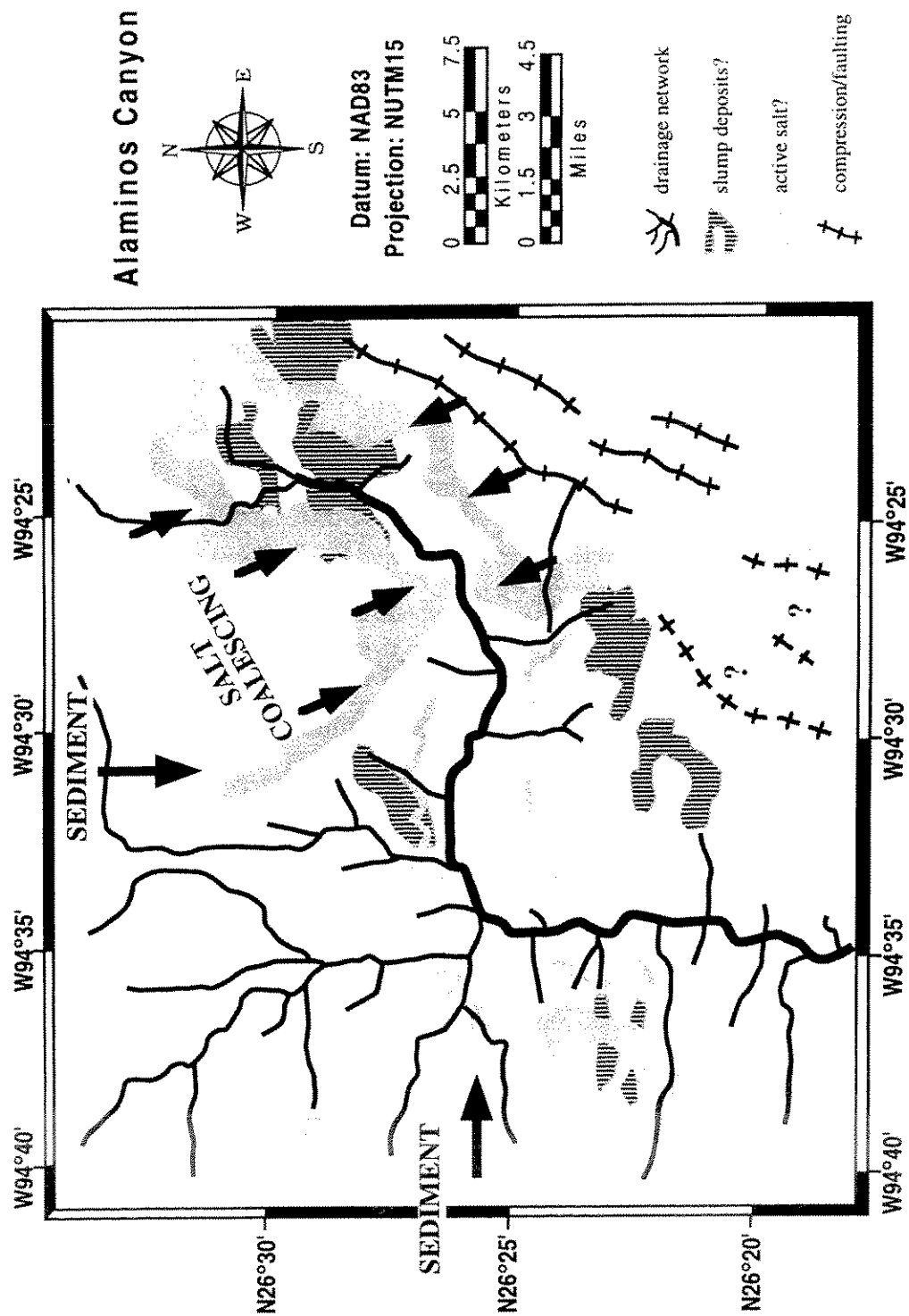


Figure 53-Line drawing of geological interpretation of the Alaminos Canyon.

These two re-entrants might be old sediment transportation routes that received sediments of the Colorado and Brazos rivers from the north and the Rio Grande river from the west. These sediment paths are also documented by the drainage patterns extracted from morphology. Re-entrant E exhibiting high slope gradients and a rugged seafloor is the product of the underlying coalescing salt. The major drainage path passes through this re-entrant from northeast, through a 100-200 m high ridge, and on to the southwest inside of the canyon. This segment of drainage path may be an old drainage path, and Re-entrant E is closing up and may eventually become a basin.

There are many channels in the northern and western walls of the main drainage path, but there are very few channels in the southern and eastern walls. Because the major sediment sources are from the north and west, the channels in the northern and western walls are traceable and better defined. The channels in the southern and eastern walls may be salt uplift motivated features. The U-shaped main drainage path does not have a smooth and continuous shape but shows a series of terrace steps which might be caused by intermittent sediment input or underlying salt movement. These sporadic events are also supported by other findings: The channels flowing toward the main path show mixed U-shaped and V-shaped walls and suggest old and recent sediment transport conduits. The recent or rejuvenating routes might have been triggered by the uplift of underlying salt. Episodic uplifting can form semi-continuous reflectors observed in the speculative Holocene Deep Tow records. The correlation of sediment accumulation rates in cores AC01 and AC02 also suggests intermittent sediment input. The lack of channel levees suggest sediment transporting mechanism other than turbidity currents. The high sedimentation rate and near seafloor semi-transparent reflectors suggest the presence of debris flow deposits. These debris flow deposits can be deposited over a wide area or locally.

From the sedimentation point of view, the upper slope is an extension zone that is dominated by normal faulting with a high subsidence rate, and it can trap a major portion of the sediment that prograded from the shelf. The lower slope receives less sediment and is a compression zone to compensate for the extension of the upper slope. The faults in the southeast portion of the canyon shown on the seafloor relief map (Figure 38) and a seismic profile (Figure 52) indicate the compression regime. In the bathymetry derived slope direction map (Figure 39), these faults can be traced inside the canyon. These old fault planes were interrupted by the uplifted canyon wall and further subdued by sedimentation. These NNE-SSW oriented faults display a similar trend as the Perdido Foldbelt. Small faults occur in the north of the main drainage path align in the same NNE-SSW direction and serve as channel conduits. Although there is no evidence that the channels in the west of the main drainage path follow another set of fault planes, it is possible that NNW-SSE direction conjugate faults do exist.

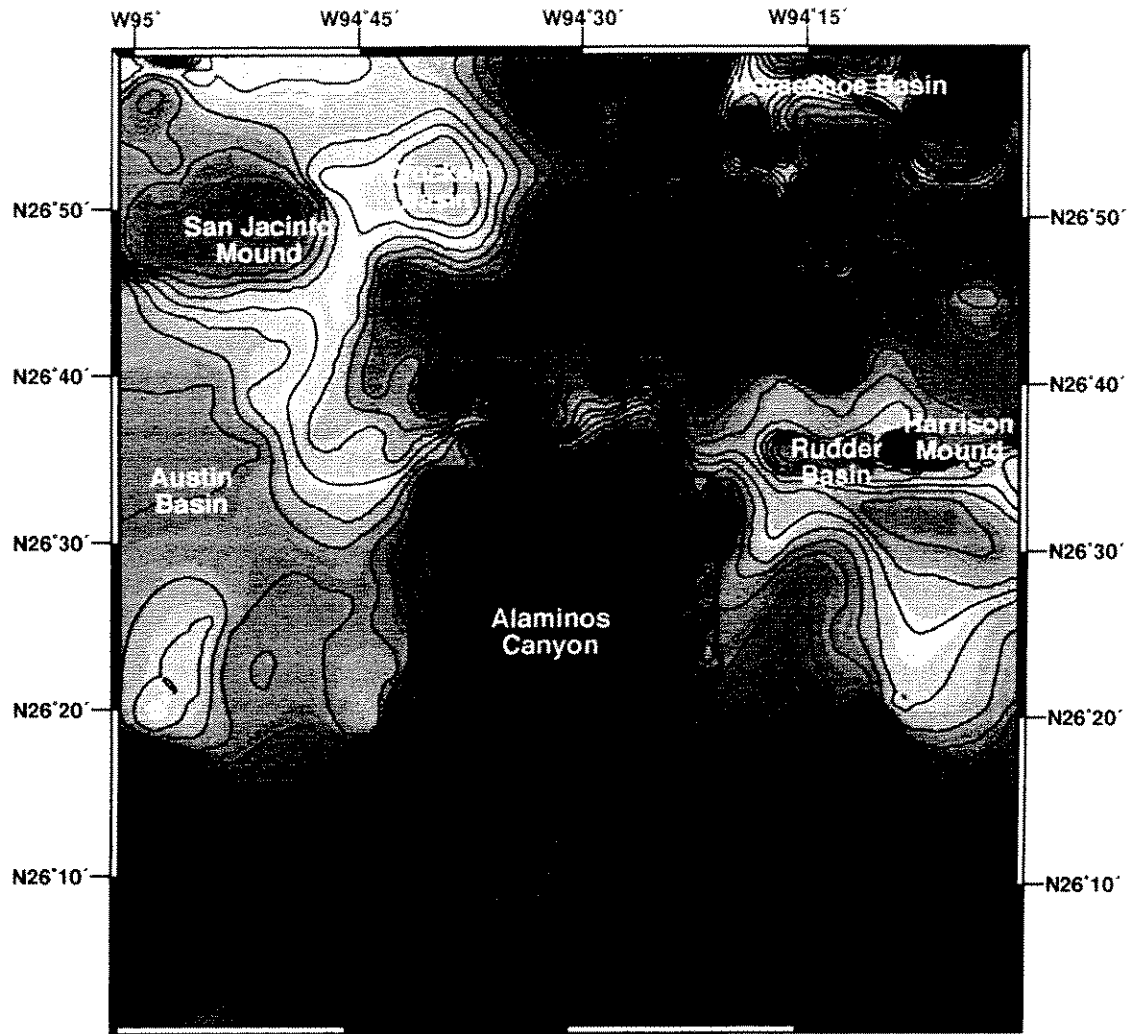
The relatively featureless sidescan sonar image suggests that the study area is a homogeneous, and because of the water depth, most likely a low-energy environment. The high toned or high backscattered areas occurring in the northeast and central west of the canyon coincide with the areas with the highest slope gradients and roughest seafloor. However, a major portion of the area with steep slope and rough seafloor do not show high backscattering. These areas usually align in a north-south direction and can be explained by Lambert's Law. According to Lambert's Law, the area that should have enhanced backscattering is the middle segment of the main drainage path, which has steep slopes, a rough seafloor, and aligns in an east-west direction. However, the sonograph of this area is hindered by the messy near range. North of the ridge, the area which separates Re-entrant E from the canyon, has a high slope gradient but not a rough seafloor, and displays moderate backscattering, suggesting that seafloor roughness plays a more important role than the slope gradient in the study area. Other areas that show

high backscattering with moderate slope gradients lie in between the canyon rim and main drainage path. The high backscattering patch in the north of the main drainage path corresponds with a ridge identified by the flow direction map. Different sediment characteristic is believed to be the cause of high backscattering in these two areas. A possible explanation is the presence of slump deposits that were shed from the highly active salt fronts. While in the high slope gradient salt front, sediment creep instead of mass wasting is more common. According to the energy attenuation rate of the study area, these slump deposits should be within meters range to the seafloor.

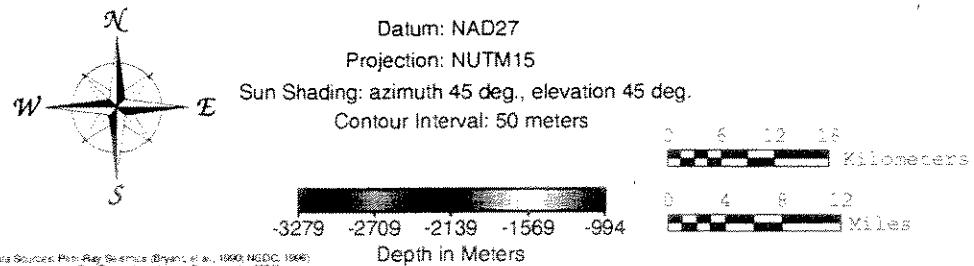
### **Visualization and data sharing**

Like Figure 38, the composite relief map based on Sea Beam and seismic data can also be coded with color and an artificial incident light. Figure 54 shows this relief map overlain with depth contours. Special glasses using light wavelength varied refraction can be used to enhance 3-D feels on the 2-D map (Toutin, 1997). The relief map can also be combined with other data and displayed in 3-D perspective views. Figure 55 is the bathymetry relief overlain with slope gradient, drainage network, and ground truth locations. With three times of vertical exaggeration and an adjusted viewing angle, the drainage paths and spatial relationship between AC01 and AC02 are better revealed (Figure 56). The coalescing of salt in the northeast re-entrant is evident. In Figure 57, the color-coded GLORIA II image drapes the bathymetry. The high backscattered areas, shown in red and blue color, lying between the drainage paths in moderate slope inclination are interpreted as slumps caused by salt uplifting.

One problem with viewing 2-D maps is we always want to zoom in to a specific portion of the map. One problem with viewing 3-D perspectives is we need to manipulate the data for viewing in different directions. This is especially true when a simulated sun is



**Bathymetric Map of Alaminos Canyon and Vicinity**



Data Sources: Ron Ray Seismic (Bryant, et al., 1999; NGDC, 1996)  
and Sea Beam (Jensen and Sager, et al., 1999).  
Compiled and Plotted by Jia Y. Liu (jiauliu@smu.edu)  
Date: November, 1999

Figure 54-Composite relief map of the Alaminos Canyon area.



Figure 55—Color-coded slope gradient, drainage network, ground truth locations draped over bathymetry.



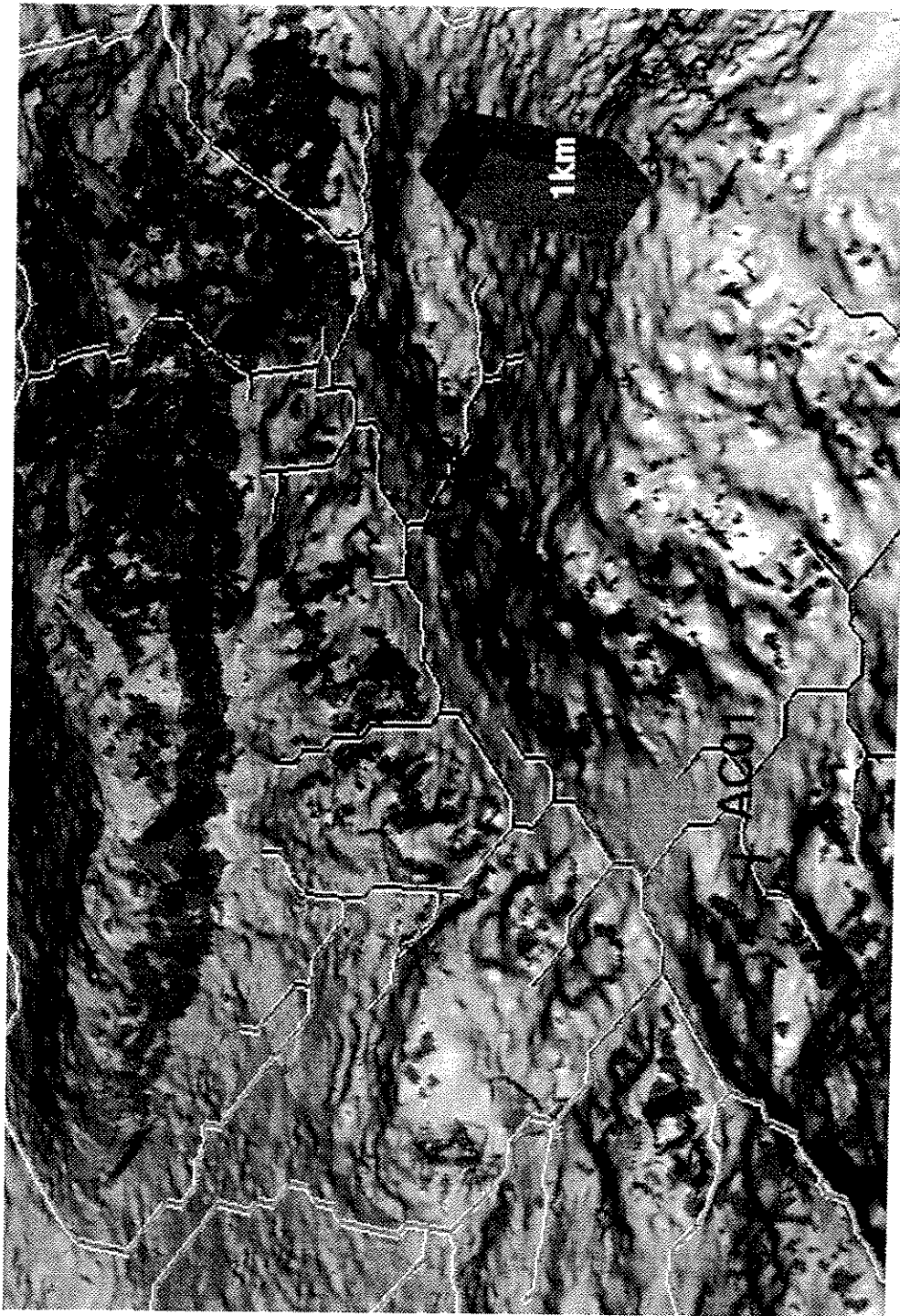


Figure 56—Same as Figure 55 but with three times of vertical exaggeration and a different viewing direction.



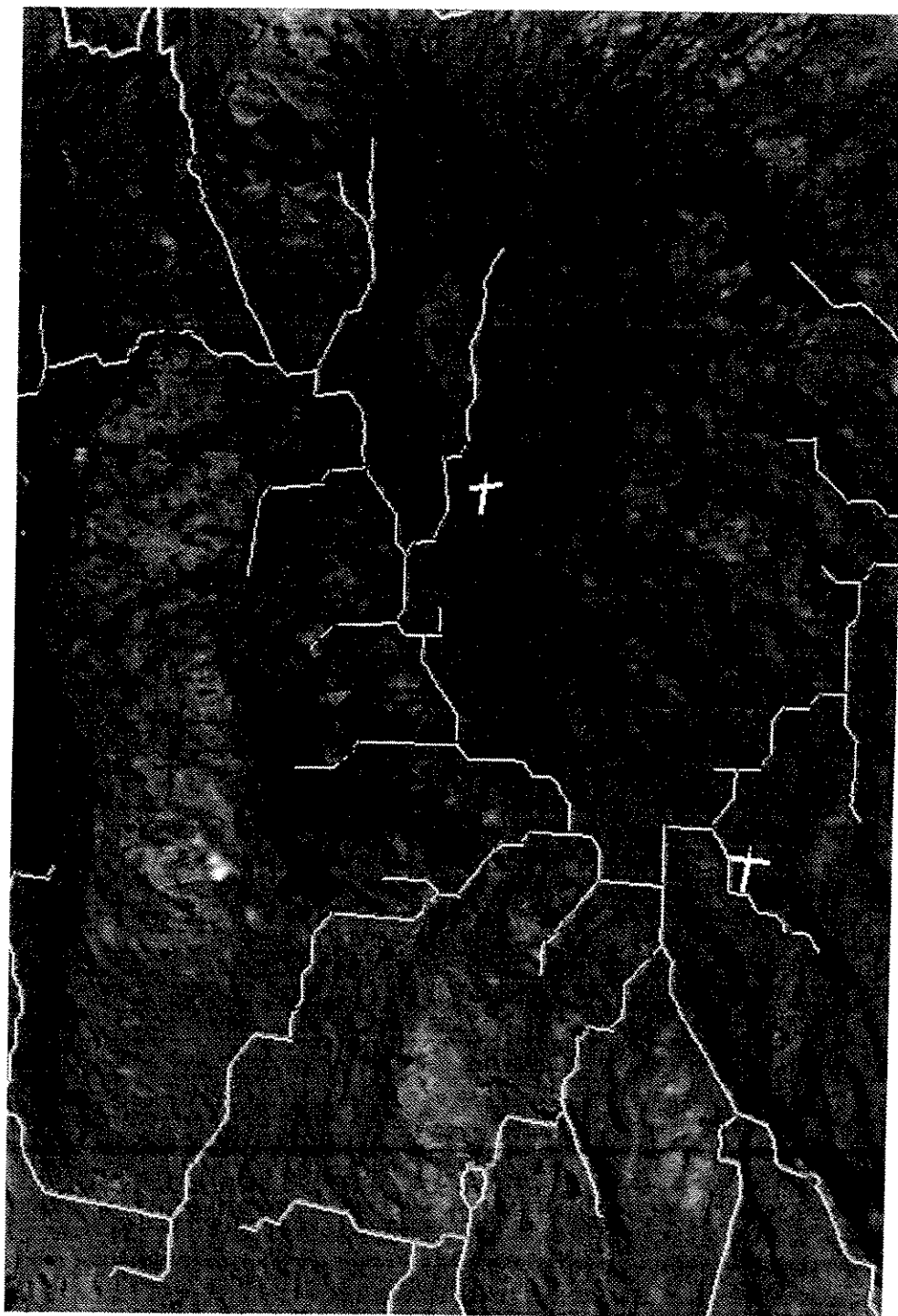


Figure 57—Color-coded GLORIA II image draped over Sea Beam bathymetry. Same vertical exaggeration and viewing direction as Figure 53.

applied and the emphasized features are always oriented orthogonal to the illumination direction. To overcome these deficiencies, much effort has been exerted by the computer industry to enable automatic mapping and virtual interaction in 3-D. By using the technique of Common Gateway Interface (CGI) script and Virtual Reality Modeling Language (VRML), it is possible to enable interactive mapping (Figure 58) and 3-D “fly-by” (Figure 59) through the Internet. Work remains to determine how to integrate different data sets and put geographic controls on a 3-D environment.

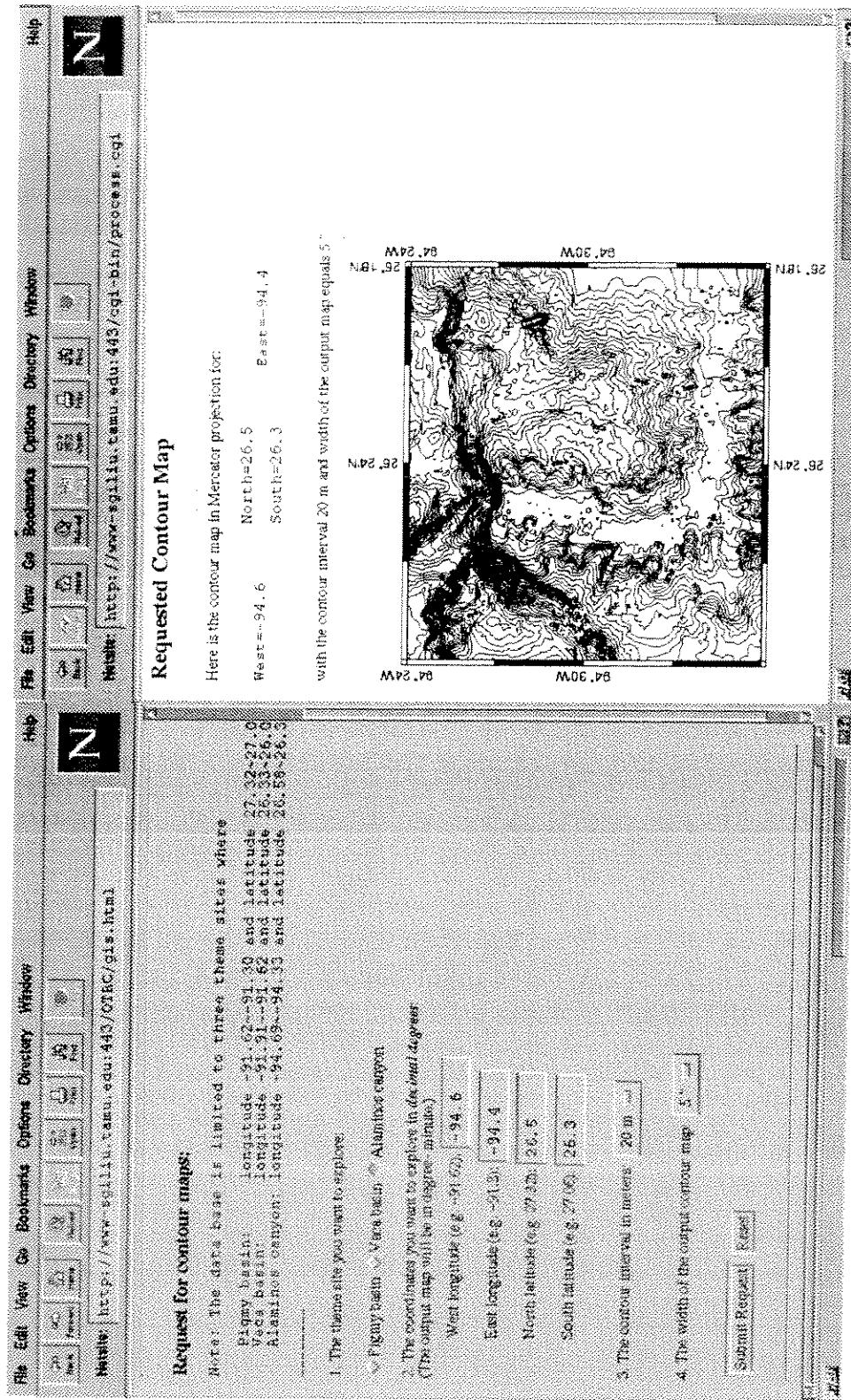


Figure 58—Interactive bathymetric contour mapping through the Internet.

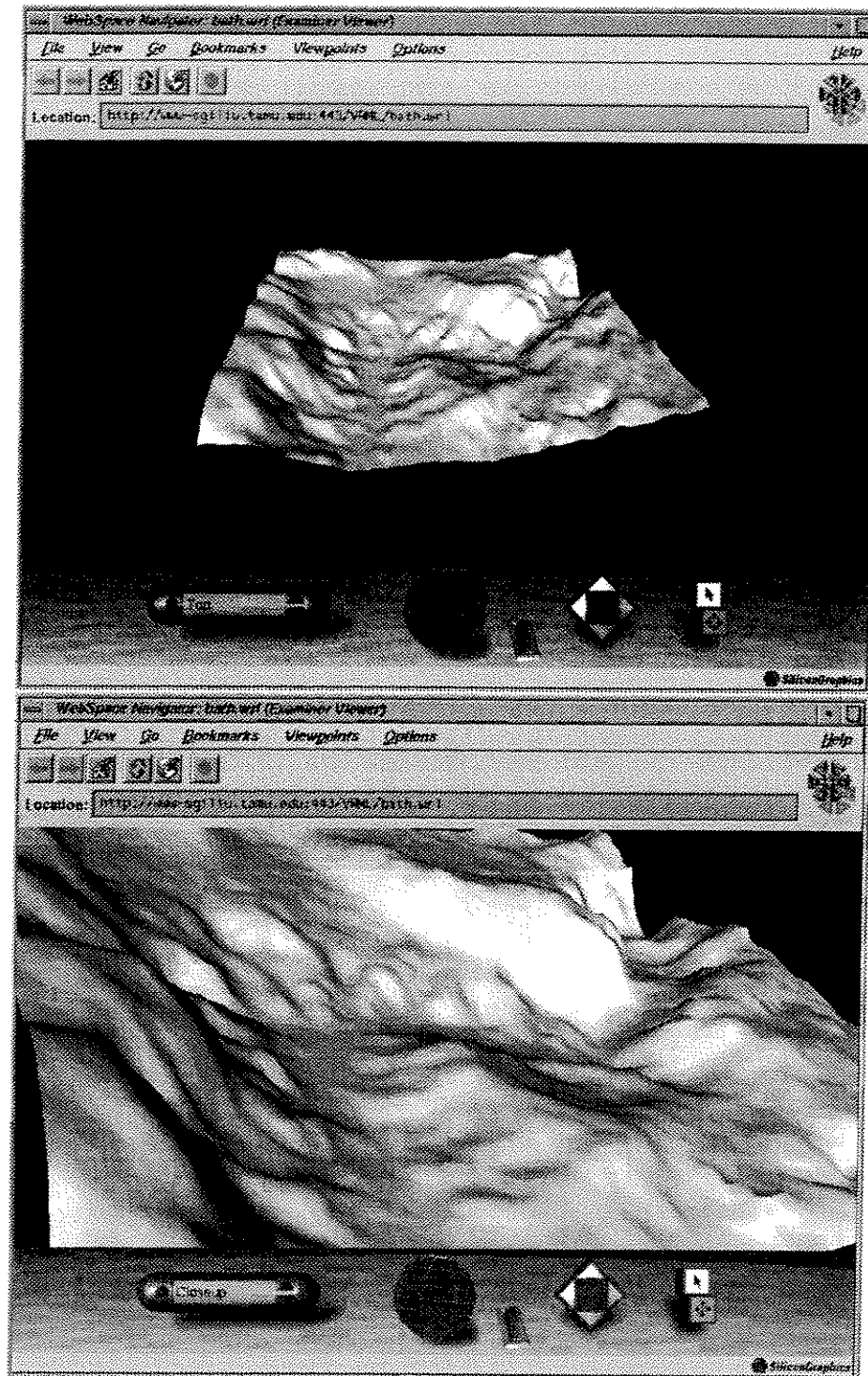


Figure 59—VRML enabled "fly-by" in the Alaminos Canyon.

## CHAPTER V

### SUMMARY AND CONCLUSIONS

This study reprocesses the multibeam data and sidescan sonar data for the Alaminos Canyon, Gulf of Mexico. The uncertainties of spatial interpolation for depth soundings and parameters affecting sidescan sonar backscattering are addressed. Ground truth samples and other supporting geophysical data are incorporated with the bathymetry and backscattered imagery to give geological scenarios for the canyon. In summary, the conclusions are:

1. A multibeam data error rejecting algorithm modified from Herlihy et al. (1992) is developed which can be used after the data are collected. Based on minimum surrounding data points and a tolerable depth range, the algorithm can reject most of the incorrect depth soundings collected during multibeam surveys, while good soundings remain intact.
2. Seven interpolation methods are examined to grid Sea Beam soundings to a 50 m spaced lattice. According to cross validation, the SubUK method shows the smallest residual and least variation ( $MAE = 4.9$  and  $MSE = 42.1$ ). Due to many voids generated by the SubUK method, the method with second least residual and variation, UKI, is adopted ( $MAE = 5.0$  and  $MSE = 44.6$ ). Depth difference caused by different interpolation methods can be more than 35 m, which is greater than the inaccuracy of the machine (25 m) and seven times the depth correction resulting from application of Carter's Table in the study area (-5 m to -2 m).

3. The reprocessing of GLORIA II imagery focuses on pixels' closeness to their true locations and differentiating true backscattering from artifacts. The technique used to remove messy near nadir zone values is experimental. The histogram-matching and random-points-filled methods are chosen rather than running another pass of "shading correction" and interpolated with cubic spline function. This is because the former methods give better signal-to-noise ratio (-14 dB to -28 dB), aesthetically appealing image, and backscattered DN values are hard to predict through interpolation.
4. Based on the processed Sea Beam data, some intrinsic bathymetric properties are generated: slope gradient, seafloor roughness, slope direction, and drainage network. These properties are used to infer implicit geological structures and combined with ground truth data to offer plug-in parameters for GLORIA II sonar energy attenuation model.
5. The slope values of  $10^{\circ}$ - $15^{\circ}$  typify the canyon rim and gullies that dissect the canyon escarpment. Slopes in excess of  $20^{\circ}$  are mainly located in the northeast and the central southwest portions of the canyon. The steep sloped re-entrant in the northeast of the canyon is a surficial expression of underlying coalescing salt. These high slope gradient areas also have the roughest bathymetry ( $> 5$  m) and may indicate active salt movement.
6. The drainage paths indicate sediment sources to the north and west of the canyon. A few channels in the southern and eastern walls of the main path are products of underlying salt uplifting. The salt uplifting was intermittent and caused the mixed U-shape and V-shape profiles along the channels. The U-shaped main drainage path exhibiting fluctuating incisions suggests a matured conduit but not formed by one time event.

7. Sediment accumulation rate corrects for compaction induced sediment length reduction. The correlation between AC01 and AC02 indicates episodic sediment inputs in the Holocene. The fast deposition rate ( $> 50 \text{ g/cm}^2 \text{ } 10^3 \text{ yr.}$ ) and the lack of channel levees suggest debris flows and slumps might contribute to the Holocene sedimentation. Based on Deep Tow records, debris flows can distribute locally along channel paths or evenly over a wide area, and slump deposits are located on a moderate slope.

8. Faults in the southeast of the canyon are observed in both the relief map and the seismic profile. The trends and extent of the faults are better depicted by the slope direction map. In the slope direction map, the faults seem to continue into the canyon but are dissected by the canyon wall. Although seismic profiles can display the relative movements of the faults, the multibeam bathymetry offers more than 50 times of spatial resolution than the 2-D seismics in the study area. It is evident that a detailed and reliable bathymetry can adjust other geophysical and geological observations.

9. Fault planes in the northern wall of the main drainage path served as channel conduits and are the extension of the NNE-SSW direction compression regime of the lower slope. There is no direct evidence, but the channels in the western wall of the main drainage path might lie on the conjugate fault planes in the NNW-SSE direction.

10. According to the ground truth samples, regardless of the incident angle, the acoustic transmission coefficient into the sediment is close to 1. This is because of the homogeneity of the sediment. Calculated energy attenuation rates are 0.76 dB/m to 1 dB/m at depths above 540 cm. Depending on the location, below 540 cm, the attenuation rate can reach 5.6 dB/m.

11. The reprocessed GLORIA II imagery shows a relatively homogeneous environment. Besides sediment characteristics, to have a high backscattered value in the reprocessed image, slope gradient and seafloor roughness both must be high (slope  $> 10^\circ$  and roughness  $> 5$  m). Some high backscattered patches are located adjacent to the active salt front with moderate slope gradient are interpreted as slump deposits. These slump deposits are believed to be within a few meters depth below the seafloor, as ground truth samples indicate the transmitted GLORIA II sonar energy can be 5 dB down in less than 700 cm of sediment.

12. This study uses GIS as a main tool for the integration of different data sets which allows a better spatial control and easy comparison of the data. The built-in functions of GIS and the data sharing ability of the Internet may be used for data base querying or automatic mapping, and they offer a virtual environment for deep water investigations.



## REFERENCES CITED

- Arc/Info, 1997, GIS package: Redlands, California, Environmental Systems Research Institute, Inc., version 7.1.1.
- Bouma, A. H., W. R. Bryant, and J. W. Antoine, 1968, Origin and configuration of Alaminos Canyon, northwest Gulf of Mexico: *Gulf Coast Association of Geological Societies Transactions*, v. 18, p. 290-296.
- Bouma, A. H., O. Chancey, and O. Merkel, 1972, Alaminos Canyon area, *in* R. Rezak, ed., *Contributions on the geological oceanography of the Gulf of Mexico*: Gulf Publishing Co., Houston, Texas A&M University Oceanographic Studies, p. 153-179.
- Bowditch, N., 1975, *American practical navigator: an epitome of navigation*, v. 2: Washington, D.C., U.S. Department of Defense, Defense Mapping Agency Hydrographic Center, 716 p.
- Boyce, R. E., 1976, Definitions and laboratory techniques of compressional sound velocity parameters and wet-water content, wet-bulk density, and porosity parameters by gravimetric and gamma ray attenuation techniques: *Initial Report of the Deep Sea Drilling Project*, v. 33, p. 931-958.
- Briggs, I. C., 1974, Machine contouring using minimum curvature: *Geophysics*, v. 39, p. 39-48.
- Brown, D., 1996, Industry watches deep gulf test: *AAPG Explorer*, v. 17, p. 8-9, 29.
- Bryant, W. R., J. R. Bryant, M. H. Feeley, and G. R. Simmons, 1990, Physiographic and bathymetric characteristics of the continental slope, northwest Gulf of Mexico: *Geo-Marine Letters*, v. 10, p. 182-199.
- Bryant, W. R., 1991, Physiography and bathymetry, *in* A. Salvador, ed., *The geology of North America*. v. J, *The Gulf of Mexico Basin*: Boulder, Colorado, Geological Society of America, p. 13-30.
- Burrough, P. A., 1992, *Principles of Geographical Information Systems for land resources assessment*: New York, Oxford University Press, 194 p.
- Carter, D. J. T., 1980, *Echo-sounding correction tables: formerly Matthews' tables*, 3rd ed.: Taunton, Somerset, England, Hydrographic Department, Ministry of Defense, 150 p.
- Cerveny, V., and R. Ravindra, 1971, *Theory of seismic head waves*: Toronto, University of Toronto Press, 312 p.
- Charnock, H., and J. Crease, 1966, *Revision of Matthews' tables: pilot study of the Mediterranean Sea*: Internal Report, National Institute of Oceanography UK, no. A26, 36 p.

- Chavez, P. S., Jr., and L. A. Soderblom, 1974, Simple high-speed digital image processing to remove quasi-coherent noise patterns: Proceedings of the American Society of Photogrammetry, 41st Annual Meeting, p. 595-600.
- Chavez, P. S., Jr., 1980, Automatic shading correction and speckle noise mapping/removal techniques for radar image data: National Aeronautics and Space Administration, JPL Publication 80-61, p.251-262.
- Chavez, P. S., Jr., 1986, Processing techniques for digital sonar images from GLORIA: Photogrammetric Engineering and Remote Sensing, v. 52, p. 1133-1145.
- Crease, J., and P. Edwards, 1972, Revision of Matthews' tables: pilot study of the Gulf stream region: Internal Report, National Institute of Oceanography UK, no. A56, 20 p.
- de Moustier, C., and M. C. Kleinrock, 1986, Bathymetric artifacts in Sea Beam data: how to recognize them and what causes them: Journal of Geophysical Research, v. 91, p. 3407-3424.
- ER Mapper, 1995, GIS package: San Diego, California, Earth Resource Mapping Pty Ltd, version 5.2.
- EEZ-Scan 85 Scientific Staff, 1987, Atlas of the U.S. exclusive economic zone, Gulf of Mexico: U.S. Geological Survey Miscellaneous Investigations Series, I-1864-A, Scale 1:500,000, 104 p.
- Farr, H. K., 1980, Multibeam bathymetric sonar: Sea Beam and Hydrochart: Marine Geodesy, v. 4, p. 77-93.
- Fiduk, J. C., B. D. Trudgill, M. G. Rowan, P. Weimer, P. E. Gale, B. E. Korn, R. L. Phair, W. T. Gafford, G. R. Roberts, S. W. Dobbs, and C. K. Guu, 1996, Allochthonous salt surrounding Alaminos Canyon, northwestern deep Gulf of Mexico: Gulf Coast Association of Geological Societies Transactions, v. 46, p. 27-38.
- Fofonoff, N. P., and R. C. Millard Jr., 1983, Algorithms for computation of fundamental properties of seawater: Paris, The Organization, Unesco Technical Paper in Marine Science, no. 44, p. 1-53.
- Gardner, J. V., M. E. Field, H. J. Lee, B. E. Edwards, D. G. Masson, N. H. Kenyon, and R. B. Kidd, 1991, Ground-truthing 6.5-kHz side scan sonographs: What are we really imaging?: Journal of Geophysical Research, v. 96, p. 5955-5974.
- Garrison, L. E., and H. L. Berryhill, 1970, Possible seaward extension of the San Marcos arch (abs.): GS Abstracts with Programs, v. 2, p. 285-286.
- Gealy, B. L., 1955, Topography of the continental slope, northwest Gulf of Mexico: GSA Bulletin, v. 66, p. 203-227.
- GRASS, 1993, Geographic resources analysis support system: Champaign, Illinois, U.S. Army Construction Engineering Research Laboratories (USACERL), version 4.1.

- Greenberg, D. A., and H. E. Sweers, 1972, Possible improvements to Matthews' Tables in areas of Canadian data holdings: *International Hydrographic Review*, v. 49, p. 127-151.
- Hamilton, E. L., 1972, Compressional-wave attenuation in marine sediment: *Geophysics*, v. 37, p. 620-646.
- Hamilton, E. L., 1976, Shear-wave velocity versus depth in marine sediments: a review: *Geophysics*, v. 41, p. 985-996.
- Hardin, N. S., 1989, Allochthonous salt sheets in the Alaminos Canyon region, northwest Gulf of Mexico: present configuration and processes of emplacement: Ph. D. thesis, Texas A&M University, College Station, Texas, 202 p.
- Herlihy, D. R., T. N. Stepka, and T. D. Rulon, 1992, Filtering erroneous soundings from multibeam survey data: *International Hydrographic Review*, v. 69, no. 2, p. 67-76.
- Isaaks, E. H., and R. M. Srivastava, 1989, *An introduction to applied geostatistics*: New York, Oxford University Press, 561 p.
- Jain, A. K., 1989, *Fundamentals of digital image processing*: Englewood Cliffs, New Jersey, Prentice-Hall, 569 p.
- Johnson, H.P., and M. Helferty, 1990, The geological interpretation of side-scan sonar: *Reviews of Geophysics*, v. 28, no. 4, p. 357-380.
- Kleinrock, M. C., 1991, Capabilities of some systems used to survey the deep-sea floor, in R. A. Geyer, ed., *CRC Handbook of Geophysical Exploration at Sea*: Boca Raton, Florida, CRC Press, p. 35-86.
- Koczy, F. F., 1951, Factors determining the element concentration in sediments: *Geochim. Cosmochim. Acta*, v. 1, p. 73-85.
- Lancaster, P., and K. Salkauskas, 1975, *An introduction to curve and surface fitting*, Unpublished manuscript: Division of Applied Mathematics, University of Calgary, Canada, 114 p.
- Li, R., 1992, Shape from shading-a method of integration of sonar images and bathymetric data for ocean mapping: *Marine Geodesy*, v. 15, p. 115-127.
- Matheron, G., 1971, *The theory of regionalized variables and its applications*: Paris, École nationale supérieure des mines, 211 p.
- Matthews, D. J., 1927, *Tables of the velocity of sound in pure water and sea water for use in echo-sounding and sound-ranging*, 1st ed.: London, Hydrographic Department, Admiralty, 30 p.
- Matthews, D. J., 1939, *Tables of the velocity of sound in pure water and sea water for use in echo-sounding and sound-ranging*, 2nd ed.: London, Hydrographic Department, Admiralty, 52 p.

- Mechler, S. M., 1994, Seismic stratigraphy and salt tectonics of the Alaminos Canyon area, Gulf of Mexico: Master's thesis, Texas A&M University, College Station, Texas, 71 p.
- NOAA, 1992, Atlas of NOAA's multibeam sounding data in the Gulf of Mexico, exclusive economic zone: NOAA/NOS/Coast & Geodetic Survey, Rockville, Maryland, v.1, 59 p.
- PV-WAVE, 1994, PV-WAVE Advantage: Houston, Texas, Visual Numerics, Inc., version 5.00.
- Sager, W. W., 1997, Personal communication.
- Simmons, G. R., 1992, The regional distribution of salt in the northwestern Gulf of Mexico: styles of emplacement and implications for early tectonic history: Ph. D. thesis, Texas A&M University, College Station, Texas, 183 p.
- Simmons, G. R., W. R. Bryant, R. Buffler, G. Lee, and C. Fiduk, 1996, Regional distribution of salt and basin architecture in the northwestern Gulf of Mexico: Gulf Coast Association of Geological Societies Transactions, v. 46, p. 93-94.
- Smith, W. H. F., and P. Wessel, 1990, Gridding with continuous curvature splines in tension: Geophysics, v. 55, p. 293-305.
- Sutton, J. L., 1979, Underwater acoustic imaging: Proceedings of IEEE, v. 67, p. 554-566.
- Swain, C., 1976, A Fortran IV program for interpolating irregularly spaced data using difference equations for minimum curvature: Computers and Geosciences, v. 1, p. 231-240.
- Toutin, T., 1997, Qualitative aspects of chromo-stereoscopy for depth perception: Photogrammetric Engineering & Remote Sensing, v. 63, p. 193-203.
- Treadwell, T. K., Jr., 1949, Submarine topography of the continental slope of the northwest Gulf of Mexico: Submarine Geology Report, Scripps Institution of Oceanography, University of California at San Diego, no. 7, 7 p.
- Trudgill, B. D., M. G. Rowan, J. C. Fiduk, P. Weimer, P. E. Gale, B. E. Korn, R. L. Phair, W. T. Gafford, G. R. Roberts, S. W. Dobbs, and C. K. Guu, 1997, The Perdido Fold Belt, northwestern deep Gulf of Mexico: Part 1. Structural geometry and evolution: AAPG Bulletin, in press.
- Tyce, R. C., 1986, Deep seafloor mapping systems - a review: Marine Technology Society Journal, v. 20, p. 4-15.
- Tyce, R. C., J. Miller, and R. Edwards, 1987, Deep ocean pathfinding with the Sea Beam sonar: Sea Technology, v. 28, p. 37-40.
- Uchupi, E., 1968, Map showing relation of land and submarine topography, Mississippi Delta to Bahia de Campeche: U.S. Geological Survey Miscellaneous Geologic Investigations Map I-521, Scale 1:1,000,000.

- Urick, R. J., 1983, Principles of underwater sound: New York, McGraw-Hill, 423 p.
- Wahba, G., 1990, Spline models for observational data: CBMS-NSF Regional Conference Series in Applied Mathematics: Philadelphia, Society for Industrial and Applied Mathematics, 169 p.
- Wessel, P., and W. H. F. Smith, 1995, GMT, The generic mapping tools: Manoa, Hawaii, School of Ocean and Earth Science and Technology, University of Hawaii at Manoa, version 3.0.
- Wetzel, A., and B. Kohl, 1986, Accumulation rates of Mississippi Fan sediments cored during Deep Sea Drilling Project leg 96: Initial Report of the Deep Sea Drilling Project, v. 96, p. 595-600.
- Winker, C. D., 1982, Cenozoic shelf margins, northwestern Gulf of Mexico: Gulf Coast Association of Geological Societies Transactions, v. 22, p. 427-448.
- Young, G. B., and L. W. Braile, 1976, A computer program for the application of Zoeppritz's amplitude equations and Knott's energy equations: Bulletin of the Seismological Society of America, v. 66, p. 1881-1885.
- Zoeppritz, K., B. Erdbebenwellen VIII, 1919, Über reflexion und durchgang seismischer wellen durch unstetigkeitsflächen: Gottinger Nachr., v. 1, p. 66-84.

## APPENDIX A

## DATA BASE

Table A-1. Sea Beam data

File Name	Depths (m)		Max.	Min.	Min.	Max.	Rec. Date
	Min	Max	Latitude	Latitude	Longitude	Longitude	
cb90apr11.d01	1382	2552	26.6797	26.3257	-94.5532	-93.8965	90 04 11
cb90apr11.d02	1822	2649	26.3568	26.3231	-94.6893	-94.4827	90 04 11
cb90apr12.d01	1677	2639	26.4907	26.3420	-94.6729	-94.3597	90 04 12
cb90apr12.d02	1676	2335	26.4075	26.3425	-94.5061	-94.3595	90 04 12
cb90apr12.d03	2154	2307	26.3468	26.3235	-94.4799	-94.4198	90 04 12
cb90apr12.d04	209	2672	26.4730	26.3058	-94.6842	-94.3573	90 04 12
cb90apr13.d01	37	2618	26.5732	26.2922	-94.6777	-94.3452	90 04 13

Table A-2. GLORIA II 6-hour images

File Name	Depths(m)		Starting	Ending	Starting	Ending	Rec. Date
	Min	Max	Latitude	Latitude	Longitude	Longitude	
G85_0704	1632	2624	26.189100	26.321325	-94.998398	-94.159714	85 08 22
G85_0802	1431	2523	26.449600	26.421452	-93.798302	-94.714455	85 08 24
G85_0803	1540	2210	26.421400	26.533749	-94.715797	-94.473579	85 08 24
G85_0804	1410	2001	26.533800	26.553900	-94.472298	-93.575752	85 08 25

Table A-3. Ground truth data

Core Number	Longitude	Latitude	Core length (cm)	Depth (m)
AC01	94°34.93'W	26°24.57'N	849	2544
AC02	94°30.524'W	26°24.482'N	789	2379
AC03	94°24.143'W	26°33.274'N	780	1829
AC05	94°27.999'W	26°39.124'N	809	1407

## APPENDIX B

### INTERPOLATION METHODS

#### IDW (inverse distance weighting) method

The most common IDW method uses weights that are inversely proportional to the distance. The choice of weight can also be inversely proportional to the power of the distance from the known points to the estimated point:

$$\hat{Z} = \frac{\sum_{i=1}^n \frac{Z_i}{d_i^x}}{\sum_{i=1}^n \frac{1}{d_i^x}} \quad (A1)$$

where  $\hat{Z}$  is the estimated value,  $Z_i$  are the sample values,  $d_i$  is the distance between the estimated value and sample values, and  $x$  is the power of the distance.

#### MinCurv (minimum curvature with tension) method

Smith and Wessel (1990) adapted the minimum curvature method by Briggs (1974) and Swain (1976) and put anisotropy and tension parameters. The anisotropy parameter is to adjust the ratio of latitude versus longitude. The tension parameter is to restrain the extraneous inflection points that commonly occurred in the minimum curvature method.

This method uses nearby grid points and one off-grid point to infer the unknown point. If the unknown point,  $Z_{0,0}$ , is located at  $(x_0, y_0)$ , the off-grid constraining point,  $Z_c$ , is located at  $(x_0 + \xi, y_0 + \alpha\eta)$ . The unknown point can be solved by:

$$Z_{0,0} = \frac{(1-T)\{Z_{2,0} + Z_{-2,0} + \alpha^4(Z_{0,2} + Z_{0,-2} + 2\alpha^2(Z_{1,1} + Z_{1,-1} + Z_{-1,1} + Z_{-1,-1} - 2(1+\alpha^2)[Z_{1,0} + Z_{-1,0} + \alpha^2(Z_{0,1} + Z_{0,-1}) + \sum_{i=1}^5 b_i Z_i - T \sum_{i=1}^5 b_i Z_i)\}}{T \sum_{i=1}^5 b_i - 2(1-T)[(1+\alpha^4) - (1+\alpha^2) \sum_{i=1}^5 b_i]} \quad (A2)$$

where  $T$  is the tension which varies from 0 to 1,  $\alpha$  is the aspect ratio,  $Z_{x,y}$  is the relative position of a grid point with respect to  $Z_{0,0}$ , and  $b_1$ - $b_5$  are:

$$b_1 = \xi b_5 + b_4 - b_2, \quad (A3)$$

$$b_2 = \alpha\eta(1 + \xi)b_5 - b_3, \quad (A4)$$

$$b_3 = \alpha\eta(1 + \xi)b_5 - 2b_4, \quad (\text{A5})$$

$$b_4 = 1 - \frac{b_5(\xi + \xi^2)}{2}, \quad (\text{A6})$$

$$\text{and } b_5 = \frac{2(1 + \alpha^2)}{(\xi + \alpha\eta)(1 + \xi + \alpha\eta)} \quad (\text{A7})$$

### TIN (triangulated irregular network) method

In a case of using a weighted linear combination to derive the unknown point, TIN method may be displayed as (Figure A-1; Isaaks and Srivastava, 1989):

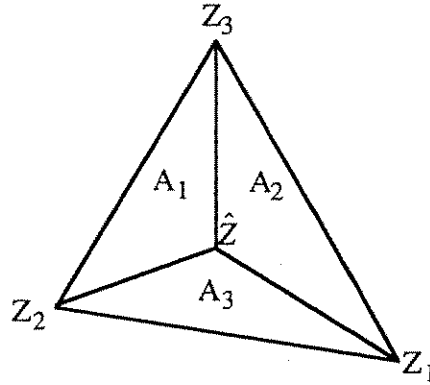


Figure A-1-Point,  $\hat{Z}$ , is estimated from weighted linear combination of  $Z_1$ ,  $Z_2$ , and  $Z_3$ .

$$\hat{Z} = \frac{A_1 Z_1 + A_2 Z_2 + A_3 Z_3}{A} \quad (\text{A8})$$

where  $\hat{Z}$  is the estimated value,  $Z_1$ ,  $Z_2$ , and  $Z_3$  are the values of the known points,  $A_1$ ,  $A_2$ , and  $A_3$  are the areas of the corresponding triangles, and  $A$  is the area of the composite triangle.

### Kriging

The steps in doing kriging are plotting a semivariogram, fitting a model, finding the weights, and interpolating. The semivariogram is a plot of semivariance versus the sample distance.

$$\hat{\gamma}(h) = \frac{1}{2n} \sum_{i=1}^n \{Z(X_i) - Z(X_i + h)\}^2 \quad (\text{A9})$$



where  $\hat{\gamma}(h)$  is semivariance,  $n$  is the number of pairs of samples separated by distance  $h$ ,  $Z(x_i)$  is sample value at location  $x_i$ , and  $Z(x_i+h)$  is sample value at  $h$  distance from  $Z(x_i)$ .

In a typical semivariogram, the semivariance first increases with distance then levels off (Figure A-2). The space between sample points is called lag. The  $h$  value when it levels off is called range. When  $h$  is less than the range, the values are spatially correlated, so it decides how big the window size is for weighted moving average interpolation. The horizontal level-off part is called sill. When  $h$  approaches 0, the interception of  $\hat{\gamma}(h)$  is called nugget, which is the spatially uncorrelated residual or noise. This noise not only can come from measurement error but is also a scale varied variable which means the spatial variation is shorter than the sample spacing.

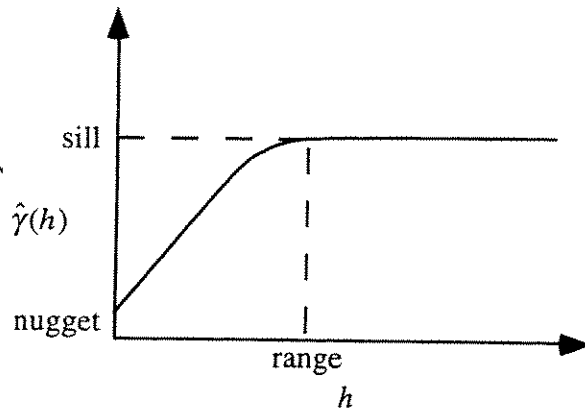


Figure A-2-An ideal semivariogram.

Common models used to describe the semivariance include: spherical, exponential, gaussian, power, and linear models. In this study, a gaussian model is used for modeling OK. This is because except for the faults, the seafloor is usually a continuous feature, and near the origin, the curve is parabolic and concave upward. A gaussian model:

$$\hat{\gamma}(h) = c_0 + c(1 - e^{-h^2/a^2}) \quad (\text{A10})$$

where  $c_0$  is nugget,  $c$  is variance contribution value, and  $a$  is range.

After fitting the model, weights are determined so the estimate is unbiased, and the estimation variance is the minimum:

$$\hat{Z}(x_0) = \sum_{i=1}^n \lambda_i Z(x_i) \quad (\text{A11})$$

The weights,  $\lambda_i$ , can be solved by:

$$\sum_{i=1}^n \lambda_i C_{ij} + \mu = C_{i0} \quad (\text{A12})$$

or in a matrix form:

$$\begin{bmatrix} \lambda_1 \\ \cdot \\ \cdot \\ \lambda_n \\ \mu \end{bmatrix} = \begin{bmatrix} C_{11} & \cdot & \cdot & C_{1n} & 1 \\ \cdot & \cdot & \cdot & \cdot & \cdot \\ \cdot & \cdot & \cdot & \cdot & \cdot \\ C_{n1} & \cdot & \cdot & C_{nn} & 1 \\ 1 & \cdot & \cdot & 1 & 0 \end{bmatrix} \begin{bmatrix} C_{10} \\ \cdot \\ \cdot \\ C_{n0} \\ 1 \end{bmatrix} \quad (\text{A13})$$

where  $C_{ij}$  is the covariance between  $i$  and  $j$ , and  $\mu$  is the Lagrange parameter.

When the study areas has a structural component, universal kriging uses a linear or quadratic function to model this drift. For the universal kriging, this study also uses the linear model to model the semivariogram:

$$\hat{\gamma}(h) = c_0 + ch \quad (\text{A14})$$

## APPENDIX C

## C-PROGRAM FOR PHYSICAL PROPERTY MEASUREMENTS

/\* This program reads in logger generated PC file then calculates velocity, Boyce density, porosity, water content, and void ratio.

Note: Need to "crush" the data file first.

Need an input AL calibrated file "aluminum.par" with calibrated slope on the first line and intercept on the second line.

Jia Y. Liu \*/

```
# include <stdio.h>
# include <math.h>

# define buffer 3000          /* store up to 3000 records */

# define R_fc 1.128           /* Boyce density parameters */
# define R_g 2.65
# define R_f 1.024
# define R_gc 2.65

# define grain_den 2.67
# define water_den 1.024

void main(int argc, char *argv[]) {
FILE *ifp1,*ifp2,*ofp1,*ofp2,*ofp3,*ofp4,*ofp5;

char vel_file[20],den_file[20],porosity_file[20],void_file[20],water_file[20]; int
samp_interval;
double temp,core_diameter;
float liner_thickness,p_wave_offset,p_wave,gamma_count_time;
float gamma_cycle,section_length,temperature;
int i,depth,DBS;
float velocity[buffer],density[buffer],boyce_den[buffer];
float porosity[buffer],voidratio[buffer],water[buffer];
float section_depth[buffer];
float deviation[buffer];
double travel_time[buffer];
long gamma[buffer];
double C2,C1;
double slope,intercept;
char ch;

/* Check if the input command is correct */
if (argc!=3) {
printf("\n");
printf("This program reads in PC logger file then output velocity, Boyce density,\n");
printf("porosity, void ratio, and water content files.\n\n");
```

```

printf("Note: 1. You need to \"crush\" the data file before running this program.\n");
printf("    e.g. crush test.dat > test_new.dat\n");
printf("    2. Need an input AL calibrated file \"aluminum.par\" with slope on the\n");
printf("    first line and intercept on the second line\n");
printf("                                           Jia Y. Liu 8/96\n\n");
printf("Usage: logger <input file> <length of previous sections>\n\n");
exit(1);
}

```

```

/* Make sure the input file name exists */
ifp1=fopen(argv[1],"r");
if (ifp1==NULL) {
    printf("Cannot open input file \"%s\"!\n",argv[1]);
    exit(1);
}

```

```

/* Make sure the slope and intercept exists */
ifp2=fopen("aluminum.par","r");
if (ifp2==NULL) {
    printf("Cannot open input parameter file \"aluminum.par\"!\n",argv[1]);
    exit(1);
}

```

```

/* Make sure the starting depth exists */
if (argv[2]==NULL) {
    printf("Need input the length of previous sections!\n");
    exit(1);
}
DBS=atoi(argv[2]);

```

```

/* Read the slope and intercept file */
fscanf(ifp2, "%lf\n",&slope);
fscanf(ifp2, "%lf\n",&intercept);

```

```

/* Read the header. Note: the delimiter is TAB */
for (i=1;i<=16;i++) {
    if (i!=2 && i!=3 && i!=4 && i!=5 && i!=8 && i!=9 && i!=12 && i!=13 && i!=16)
        while (fgetc(ifp1)!='\n') ;
    else {
        while (fgetc(ifp1)!='\t') ;
        fscanf(ifp1,"%lf\n",&temp);
        if (i==2)
            samp_interval=temp;
        if (i==3)
            core_diameter=temp;
        if (i==4)
            liner_thickness=temp;
        if (i==5)
            p_wave_offset=temp;
        if (i==8)
            gamma_count_time=temp;
    }
}

```

```

    if (i==9)
        gamma_cycle=temp;
    if (i==12)
        p_wave=temp;
    if (i==13)
        section_length=temp;
    if (i==16)
        temperature=temp;
}
}

if (p_wave!=0.) {          /* open output velocity file */
    strcpy(vel_file,argv[1]);
    strcat(vel_file,".vel");
    ofp1=fopen(vel_file,"w");
}

if (gamma_count_time!=0.) {      /* open output density file */
    strcpy(den_file,argv[1]);
    strcat(den_file,".den");
    ofp2=fopen(den_file,"w");
    strcpy(porosity_file,argv[1]);
    strcat(porosity_file,".por");
    ofp3=fopen(porosity_file,"w");
    strcpy(void_file,argv[1]);
    strcat(void_file,".voi");
    ofp4=fopen(void_file,"w");
    strcpy(water_file,argv[1]);
    strcat(water_file,".wat");
    ofp5=fopen(water_file,"w");
}

for (i=0;i<=(int)(section_length)+16;i++)
    fscanf(ifp1,"%f %f %lf %f %d %*d %*d\n",&section_depth[i],&deviation[i],&travel_time[i],&gamma[i]);

/* Calculate density, porosity, void ratio, and water content */
if (DBS == 0) {
    fprintf(ofp2,"Depth(cm)\tBulk density(g/cc)\n");
    fprintf(ofp3,"Depth(cm)\tPorosity (%) \n");
    fprintf(ofp4,"Depth(cm)\tVoid ratio\n");
    fprintf(ofp5,"Depth(cm)\tWater content (%) \n");
}
for (depth=1+14/samp_interval;depth<=(int)(section_length+14)/samp_interval;
depth++) {
    density[depth-14/samp_interval]=(log(gamma[depth]/(gamma_count_time*
gamma_cycle))-intercept)/slope/(core_diameter+deviation[depth-14/samp_interval]-
2.*liner_thickness);
    boyce_den[depth-14/samp_interval]=(density[depth-14/samp_interval]-R_fc)*
(R_g-R_f)/(R_gc-R_fc)+R_f;
    fprintf(ofp2,"%d\t%f\n",samp_interval*(depth-14/samp_interval)+DBS,boyce_den

```

```

[depth-14/samp_interval]);

    porosity[depth-14/samp_interval]=(grain_den-boyce_den[depth-
14/samp_interval])/(grain_den-water_den) * 100.;
    fprintf(ofp3,"%d\t%f\n",samp_interval*(depth-
14/samp_interval)+DBS,porosity[depth-14/samp_interval]);

    voidratio[depth-14/samp_interval]=porosity[depth-14/samp_interval]/100./(1-
porosity[depth-14/samp_interval]/100.);
    fprintf(ofp4,"%d\t%f\n",samp_interval*(depth-
14/samp_interval)+DBS,voidratio[depth-14/samp_interval]);

    water[depth-14/samp_interval]=(water_den/grain_den)*voidratio[depth-
14/samp_interval]*100.;
    fprintf(ofp5,"%d\t%f\n",samp_interval*(depth-14/samp_interval)+DBS,water[depth-
14/samp_interval]);
}

/* Calculate velocity */
if (p_wave!=0.) {          /* open output velocity file */
    if (DBS == 0)
        fprintf(ofp1,"Depth(cm)\tVelocity(m/sec)\n");
    for (depth=1;depth<=(int)(section_length/samp_interval);depth++) {
        velocity[depth]=(core_diameter+deviation[depth]-
2.*liner_thickness)/(travel_time[depth]-p_wave_offset)*1000.+3.*(20.-temperature);
        fprintf(ofp1,"%d\t%f\n",samp_interval*depth+DBS,velocity[depth]);
    }
}

/* Print out output file names */
printf("\n");
printf("The output velocity file is: %s.vel\n",argv[1]);
printf("The output Boyce density file is: %s.den\n",argv[1]);
printf("The output porosity file is: %s.por\n",argv[1]);
printf("The output void ratio file is: %s.voi\n",argv[1]);
printf("The output water content file is: %s.wat\n\n",argv[1]);

}

```

## VITA

Jia-Yuh Liu was born on January 23, 1962, in Taipei, Taiwan, R.O.C. He received a B.S. in Oceanography from National Taiwan College of Marine Science and Technology in May of 1983. He fulfilled his mandatory military service as a Second Lieutenant in the Marine Corps of Taiwan, R.O.C. from 1983-1985. After that, he returned to his alma mater and worked as a full time teaching assistant for two years. He studied seismic stratigraphy and received a M.S. in Oceanography from Texas A&M University in May 1993.

Mr. Liu is married to Meei-Hwa Wang. Their permanent mailing address is: 605 Benchmark DR, College Station, TX 77845.